Relaxometry in the Human Brain Using High Field Magnetic Resonance Imaging

by

Kelly Catherine McPhee

A thesis submitted in partial fulfilment of the requirements for the

degree of

Doctor of Philosophy

Department of Physics

University of Alberta

Abstract

Quantitative relaxation mapping allows for direct non-invasive tissue quantification with removal of variations arising from RF fields and non-uniform coil sensitivity profiles. T2 may be quantified using multi-echo spin echo sequences; however, in practical imaging situations, imperfect refocussing due to RF interference and imperfect slice profiles results in contamination of the signal decay curve by contributions from indirect and stimulated echoes.

Modelling of the multi-echo spin echo sequence by either Bloch equations or Extended Phase Graph (EPG) allows for indirect and stimulated echo compensation (ISEC). In this work, it is demonstrated that EPG-ISEC and Bloch-ISEC yield very similar but systematically different T2 results. EPG fitting provides reasonably accurate T2, but is limited by poor accuracy in resulting flip angles, and T2 errors increase when flip angles are provided. Bloch simultaneous fitting of T2 and flip angle provides excellent results, but can be limited by multiple solutions which can be overcome by including a flip angle map.

Despite the availability of methods to compensate for indirect and stimulated echoes, exponential fitting remains persistent. It is common to discard the first or all odd echoes, to improve fitting. However, it is demonstrated in this work that this is insufficient to

remove stimulated echo contamination, and errors in T2 fitting will remain significant, and will vary with T2, flip angle, and echo train length.

In clinical practice, relaxation weighted images are routinely acquired, but quantification of relaxation times typically requires additional specialized pulse sequences and hence additional imaging time, which is not typically feasible in standard clinical practice. In this work, it is demonstrated that the Bloch-based ISEC approach permits T2 to be quantified using only a Proton Density-weighted and a T2-weighted fast spin echo image and a flip angle map. With the addition of a T1 weighted image to the protocol, simultaneous T1 and T2 quantification is demonstrated. This approach may enable the introduction of quantitative relaxation into radiology protocols without substantial time penalties.

Preface

All research chapters have been published in, or are in preparation for submission to academic journals. Chapter 2 has been published as: McPhee KC, Wilman AH, "Transverse relaxation and flip angle mapping: Evaluation of simultaneous and independent methods using multiple spin echoes", *Magnetic Resonance in Medicine* (2017), vol. 77, issue 5, 2057-2065. Chapter 4 has been published as: McPhee KC, Wilman AH, "T2 quantification from only proton density and T2-weighted MRI by modelling actual refocusing angles," *NeuroImage* (2015), vol 118, 642-650. Chapter 3 is in preparation for submission to the Journal of Magnetic Resonance Imaging. Chapter 5 is in preparation for submission to Magnetic Resonance in Medicine. A.H. Wilman was the supervisory author. Dr. Wilman provided guidance throughout the process, and was involved in manuscript composition. All the data was acquired by myself, sometimes with assistance from Peter Šereš, or Nasir Uddin (1.5T data presented in Chapter 4). Unless otherwise stated, software for the calculation of T1, T2, and B1 maps in this work using MATLAB (Mathworks Inc) was prepared by the author. All analysis of MRI data presented here was performed by the author.

The research projects, of which this thesis is a part, received research ethics approval from the University of Alberta Research Ethics Board, Project Name MRI in neurological disease, No. Pro00000906, 2012-2018.

Acknowledgements

I would like to thank Dr. Alan Wilman, my supervisor, for his support, guidance, advice and assistance throughout this process. I would like to thank my committee: Dr Jack Tuszynski and Frances Fenrich. I would like to thank MR Centre staff Peter Šereš and Karim Damji for assistance with experiments. I would like to thank the various members of my lab group and other trainees at the MRI centre who have directly and indirectly assisted me, by helping with experiments, volunteering for MRIs, and sharing their expertise. Your assistance has been greatly appreciated.

I would like to thank my family, friends, and loved ones for their patience and support throughout my undergraduate and graduate education. It has been a long road.

Table of Contents

List of Tables

List of Figures

Chapter 1

Introduction

Magnetic Resonance Imaging (MRI) is an established noninvasive medical imaging tool. MRI takes advantage of the abundance of hydrogen atoms in the human body, and the principles of nuclear magnetic resonance (NMR). The hydrogen atom, has a magnetic dipole moment which is associated with its spin 1/2 nature. At thermal equilibrium, the magnetic moments of an ensemble of spins are randomly oriented. However, in the presence of a magnetic field, some of the magnetic moments have a tendency to align with the magnetic field, and will precess around an axis parallel to the magnetic field at their resonance frequency (ω_0). On a macroscopic scale, this will produce a net magnetization along the axis of the external magnetic field. With the application of a perpendicular magnetic field oscillating at ω_0, the spins may be tipped into the transverse plane where they may be detected. Following this radiofrequency pulse, the spins will relax back to their aligned state. This relaxation depends on local properties of the tissue, and includes both *longitudinal relaxation* (characterized by time constant T1) and *transverse relaxation* (characterized by time constant T2).

The benefits of MRI over other imaging techniques derive from the ability to obtain a variety of contrasts and resolutions through manipulation of the MRI pulse sequence, its noninvasive nature, and that ionizing radiation is not used. Sources of image contrast include weighting by proton density, longitudinal or transverse relaxation, flow, or diffusion, among others. With appropriate manipulation of MR image weighting to collect sets of images with purposefully varied contrast, the parameters which determine that

contrast (such as relaxation times) may be individually measured. These measurements provide tools to probe underlying tissue properties in a noninvasive manner. The focus of this thesis is quantification of relaxation times using high field MRI.

1.1 Magnetic Resonance Imaging Background

1.1.1 Spins in a Static Magnetic Field

In the presence of a magnetic field, $\vec{B}$, the potential energy of a magnetic moment, $\vec{\mu}$, is [1, 2]

$$E = -\vec{\mu} \cdot \vec{B} = -\mu_z B_0 = -\gamma S_z B_0 \tag{1.1}$$

where S_z is quantized, and may take values $\pm\hbar/2$, leading to a to distinct energy states where the magnetic moment is either parallel or antiparallel to the magnetic field. There is a tendency for spins to occupy the lower energy state, at thermal equilibrium. From Boltzman statistics, it can be shown that the ratio of spins in the parallel (ground) state, $N_\uparrow$ relative to spins in the antiparallel (excited) state, $N_\downarrow$, is [2]

$$\frac{N_\uparrow}{N_\downarrow} = e^{\Delta E/k_B T} = e^{\hbar \omega_0/k_B T} = e^{\gamma \hbar B_0/k_B T} \tag{1.2}$$

where μ is the magnetic dipole moment, k_B is Boltzmann's constant and T is temperature. It follows that the net magnetization is[1]

$$M_0 = \mu(N_\uparrow - N_\downarrow) = \mu N \tanh(\frac{\Delta E}{k_B T}) \approx \frac{N\gamma^2 \hbar^2 B}{4 k_B T} \tag{1.3}$$

where $N = N_\uparrow + N_\downarrow$. At room temperature and at 3 Tesla, $N_\uparrow/N_\downarrow$ is only slightly greater than 1 (1.0000205). However, considering there are approximately 7 x 10^{22} hydrogen atoms per millilitre of water[2] and our bodies are primarily made up of water, it becomes

---

[1]$M_0 = \mu(N_\uparrow - N_\downarrow) = \mu N \frac{N_\uparrow - N_\downarrow}{N_\uparrow + N_\downarrow} = \mu N \frac{\frac{N_\uparrow}{N_\downarrow} - 1}{\frac{N_\uparrow}{N_\downarrow} + 1} = \mu N \tanh(\frac{\Delta E}{k_B T})$. Given small x, $\tanh x \approx x$, and $\mu = \gamma\hbar/2$, we arrive at $M_0 \approx \frac{N\gamma^2 \hbar^2 B}{4 k_B T}$

[2]This may be calculated from the density of water at standard temperature and pressure, Avagadro's number, and the molecular mass of hydrogen.

obvious that this results in a sufficient net magnetization in the human body when considering a (macroscopic) imaging volume.

In the presence of a magnetic field, spins will experience a torque, and will precess around the axis of that field at a frequency ω_0 proportional to the magnetic field B_0:

$$\omega_0 = \gamma B_0 \tag{1.4}$$

where $\gamma = 2.675 \times 10^8 rads^{-1}T^{-1}$ for hydrogen. The precessional frequency is also known as the Larmor Frequency.

1.1.2 Spins in a Time Varying Field

The orientation of an ensemble of spins may be altered by the application of a radiofrequency (RF) field, applied for a finite time. Spins may be excited (tipped into the transverse plane) by application of a perpendicular radio frequency pulse, B_1, oscillating at the Larmor frequency $B_1 = B_1(t)(\cos \omega_0 t \hat{x} - \sin \omega_0 t \hat{y})$, they will continue to precess around the axis of the magnetic field. The flip angle α (the angular displacement from the equilibrium axis) is determined by:

$$\alpha = \gamma \int_0^T B_1(t)dt \tag{1.5}$$

where B_1 is the envelope, and T is the duration of the RF pulse. Transverse magnetization is expressed in a complex manner [3] :

$$M_+ \equiv M_x(t) + iM_y(t) = M_0 exp(-i\omega_0 t + i\phi_0) \tag{1.6}$$

where the phase ϕ_0 is the initial phase determined by the choice of rotational axis for the initial excitation. We may consider magnetization in a rotating frame of reference [x', y', z'], rotating with ω_0.

Slice selective excitation may be achieved by applying a linear field gradient G such that the magnetic field varies spatially with location r $B = B_0 + Gr$, and applying an RF pulse of bandwidth $\Delta\omega$. The slice width will be determined by the bandwidth of the

RF pulse

$$\Delta x = \frac{\Delta \omega}{\gamma G} \tag{1.7}$$

and the slice location may be selected my adjusting the RF frequency.

1.1.3 Signal Detection

In a receiver coil perpendicular to the transverse axis, a signal may be detected (Faraday's law of electromagnetic induction states that a change in magnetic flux over time induces a current). The induced electromotive force, ϵ in the coil due to change in magnetic flux through the coil [2, 3]:

$$\epsilon = -\frac{d\Phi}{dt} \tag{1.8}$$

where the flux can be written as

$$\Phi(t) = \int_{sample} \vec{M}(\vec{r}, t) \cdot \vec{\mathscr{B}}_{receive}(\vec{r}) dr^3 \tag{1.9}$$

where $\vec{\mathscr{B}}_{receive}$ is the receive field produced by the detection coil per unit current at all points where magnetization is non-zero [3]. The dependence on $\vec{\mathscr{B}}_{receive}$ is due to the principle of reciprocity: the flux through the detection coil due to magnetization can be found by instead calculating the flux that would be generated by that coil per unit current [3]. The induced current is thus:

$$EMF = -\frac{d}{dt} \int_V \vec{M}(\vec{r}, t) \cdot \vec{\mathscr{B}}_{receive}(\vec{r}) \tag{1.10}$$

The detected complex signal, or free induction decay (FID), is described by

$$FID \propto M_{x,y}(t) \propto M_{x,y}(0) \exp[i\omega_0 t + i\phi] exp(-t/T_2^*) \tag{1.11}$$

where ϕ is the phase with respect to the receiver at t=0.

1.1.4   Relaxation and the Bloch Equations

Spins tend to return to equilibrium. Two types of relaxation occur: longitudinal and transverse. Longitudinal relaxation (T1), also known as spin-lattice relaxation, is an energetic process where spins tend to return to their thermal equilibrium value, M_0, following excitation. Transverse relaxation (T2), also known as spin-spin relaxation is the loss of coherence in the precession of excited spins, causing a reduction in net transverse magnetization (and therefore, reduced signal). Spin-spin interactions causes local field fluctuations to occur, resulting in a loss of coherence. Relaxation of the transverse magnetization is caused by a combination of static and dynamic processes. The apparent transverse relaxation (characterized by T2*) is the combination of these:

$$\frac{1}{T2*} = \frac{1}{T2} + \frac{1}{T2'} \tag{1.12}$$

where T2 is the decay time for dynamic processes, and T2' is the decay time for static processes. Static processes may be refocussed with an RF pulse (typically 180°), resulting in a spin echo. Static processes are external field induced, such as susceptibility sources; dynamic procceses are thermodynamic in nature (see below).

Spin dynamics are governed by the phenomenological Bloch equations. The Bloch equations in the rotating frame are [3]:

$$\frac{d\vec{M}}{dt} = \gamma \vec{M} \times \vec{B} - \frac{M_x \hat{x} + M_y \hat{y}}{T2} - \frac{(M_z - M_0)\hat{z}}{T1} \tag{1.13}$$

which, taking the convention that the main magnetic field B_0 is aligned along the $\hat{z}$ axis, and considering transverse magnetization $M_{xy} = M_x + iM_y$, has the following solutions in the rotating frame:

$$M_{xy}(t) = M_{xy}(0)exp(-t/T2) \tag{1.14}$$

$$M_z(t) = M_0 + [M_z(0) - M_0]exp(-t/T1) \tag{1.15}$$

where $M_{xy}(0)$ and $M_z(0)$ are the initial transverse and longitudinal components of magnetization.

Relaxation in Solutions

The rate at which the distribution of spins exponentially approaches equilibrium following excitation via absorption of RF energy is described by relaxation time T1 [4]. Due to the small nature of this energy change, excited spins tend to not return to equilibrium spontaneously, but tend to be stimulated by interactions with surrounding materials, or *lattice* (the environment which surrounds the molecule, including the remainder of that host molecule, other solute and solvents molecules). For example, rotating or vibrating dipoles cause perturbations to the local magnetic field. The local field experienced by any given nucleus fluctuates depending on the molecular tumbling of the host molecule and surrounding molecules. Relaxation occurs due to interactions between the excited dipole with these resulting random fluctuations in local magnetic field. This process is most efficient when local magnetic field fluctuations occur at or very near the resonance frequency ω_0.

In tissue, each H atom in a water molecule generates a magnetic field of about 0.5 mT [4]. As the water molecule rotates and moves about in liquid, the local field changes constantly in amplitude and direction. Molecular tumbling due to random thermal motion of the host molecule and surrounding molecules cause fluctuations in the magnetic field experienced by a nucleus. Locally, the strength of the field is determined by the strength of nearby dipoles in the medium and how closely they approach the proton of interest.

Spin-spin relaxation, T2, represents the time in which the ensemble becomes disorganized, and thus the net transverse component to decay [4]. This transverse relaxation of a sample depends on the frequency distribution of the randomly fluctuating background magnetic field. All mechanisms which contribute to T1 also contribute to T2, because recovery of magnetization to equilibrium also results in a loss of magnetization from the transverse plane. Additionally, local dipolar fields which oscillate at low frequency can affect the precessional frequency of local nuclei, contributing to local de-phasing of transverse magnetization. Low frequency content of local dipolar fields increase monotonically as molecular motion decreases; T1 will reach a minimum value, and T2 will

continue to decrease (Figure 1.1). The minima occurs where $\tau_c \omega_0 = 0.616$[4], where τ_c is the correlation time (the average time for a molecule to rotate 1 radian).
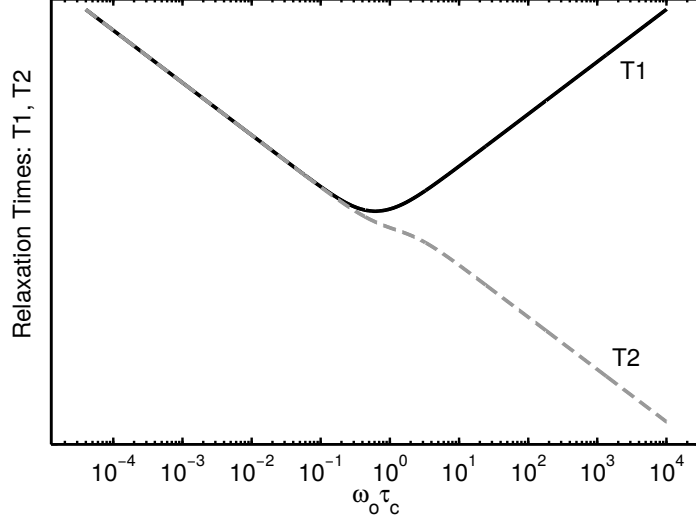
Figure 1.1: Relaxation time depends on correlation time, as predicted by Bloembergen, Purcell, and Pound. The minima occurs where $\tau_c \omega_0 = 0.616$. The x and y axis are log scale. Correlation time, τ_c increases inversely with temperature.

Relaxation theory in solutions was first described by Bloembergen, Purcell, and Pound (BPP Theory) [5]. For water, relaxation rates may be written as [5]:

$$\frac{1}{T1} = \frac{3}{2}\gamma^4 \hbar^2 I(I+1)\left[J(\omega_0) + J(2\omega_0)\right] \tag{1.16}$$

$$\frac{1}{T2} = \frac{3}{4}\gamma^4 \hbar^2 I(I+1)\left[\frac{1}{2}J(0) + 5J(\omega_0) + \frac{1}{2}J(2\omega_0)\right] \tag{1.17}$$

where ω_0 is the Larmor frequency, γ is the gyromagnetic ratio for hydrogen, I is the angular momentum quantum number, $\hbar$ is Planck's constant and $J(\omega)$ is the strength of local field fluctuating at frequency ω (spectral density).

For intramolecular relaxation in water, random walk of water undergoing self-diffusion are characterized by a single correlation time τ_c. Given the corresponding spectral densities:

$$\frac{1}{T1} = \frac{2}{5}\gamma^4 \hbar.^2 \frac{I(I+1)}{r^6}\left[\frac{\tau_c}{1+\omega_0^2 \tau_c^2} + \frac{\tau_c}{1+4\omega_0^2 \tau_c^2}\right] \tag{1.18}$$

7

$$\frac{1}{T2} = \frac{1}{5}\gamma^4\hbar^2\frac{I(I+1)}{r^6}\left[3\tau_c + \frac{5\tau_c}{1+\omega_0^2\tau_c^2} + \frac{2\tau_c}{1+4\omega_0^2\tau_c^2}\right] \tag{1.19}$$

where r is the distance between nuclei.

Relaxation in Tissues

The dipole-dipole interaction is the dominant mechanism determining relaxation rates [6]. Biological tissues are heterogeneous, and thus water may experience a variety of environments and macromolecules with which to interact. Lipids and proteins may contain freely tumbling solute ions, but may also contain membranes and other tissues which result in relatively restricted motion of water molecules [4]. These environments, and the ability of hydrogen to exchange with these pools impact relaxation times. These differences between tissues is the basis for contrast in most MR imaging. In biological tissues, macromolecular concentration, water content and water binding are all related to relaxation values [7].

In a multi-compartmental medium, relaxation is affected by the rate of exchange between compartments [4]. If compartments exchange protons much much faster than decay due to relaxation (fast exchange) the two compartments have a single relaxation rate, which is a weighted average of the two. In the case of slow exchange, relative to relaxation rates, the relaxation is then multi-exponential. For example, multi-component T2 relaxation is observed in white matter, with myelin water, intra and extracellular water, and cerebral spinal fluid being distinctly observable, and may be measured with data of sufficient time resolution and quality. Likewise, inversion recovery data with sufficient density of inversion times may be used to measure multi-component T1.

Relaxation times are shortened due to the presence of macromolecules, such as those present in tissue [4]. Generally, relaxation times are observed to be much shorter in tissues relative to pure water. Free water has a a long correlation time, and therefore a long T1 [6]. Conversely, bound water can exchange spins with the macromolecules, and thus has a much longer relaxation rate. In the case of fast exchange between bound water and free water, the observed relaxation rate will become a weighted average of the relaxation rates of the bound and free water pools.

Magnetization Transfer

Longitudinal proton magnetization can be exchanged between water and hydrogen in neighbouring nuclei [6]. The spins of bound protons cannot be measured due to very short T2. However, this bound-water fraction has a large range of resonant frequencies. This feature may be exploited, and the bound water may be saturated by choosing an excitation frequency outside of the bandwidth of the free water. Due to very short T2, this transverse magnetization will be immediately dephased. When these saturated water molecules exchange to the free water pool, the resulting free water pool has less longitudinal magnetization, and the signal is suppressed. This may be exploited purposefully to weight images. Incidental magnetization transfer also occurs in multi-slice imaging. The amount of suppression depends on the time between the off-resonance pulse and the subsequent acquisition, and the frequency offset which is used [8].

1.1.5   Spin Echo Pulse Sequences

The spin echo was first proposed by Hahn [9] for use in NMR for quantification of T2 relaxation and diffusion. The sequence consists of an excitation pulse, followed by a second pulse halfway in between the excitation and echo time. This second pulse refocusses phase accrued in the transverse plane. Spin echo may be used to quantify T2 by acquiring images at a range of echo times, and fitting for exponential decay. However, due to relatively long T2 times in liquids, diffusion will cause the signal to decay prematurely, when echo times are long [9–11], and variable echo times results in variable signal loss due to diffusion.

An example of a slice selective (2D) spin echo pulse sequence is shown in Figure 1.2. Both RF pulses and signal are shown on the first line (RF). One line of k-space is filled per TR. In a multi-slice implementation, after the echo train is acquired, before the next excitation pulse, other slices may be acquired. Crusher gradients are used on each side of the refocussing pulse. Spins which are tipped into the transverse plane by the refocussing pulse will be dephased by the second crusher. Spins which experience both crushers will be dephased then rephased.

Contrast in spin echo sequences will be determined by TE and TR. Short TE and long TR will provide a proton density-weighted image. Short TE and short TR will give a T1-weighted image. Long TE and long TR will provide a T2-weighted image. A long TE and short TR will have a mixed weighting. A typical T1-weighted image at 3T would have a TR of 600 ms, and TE of 10 ms. A T2-weighted image would have a TR of 3 seconds and TE of about 80 ms.
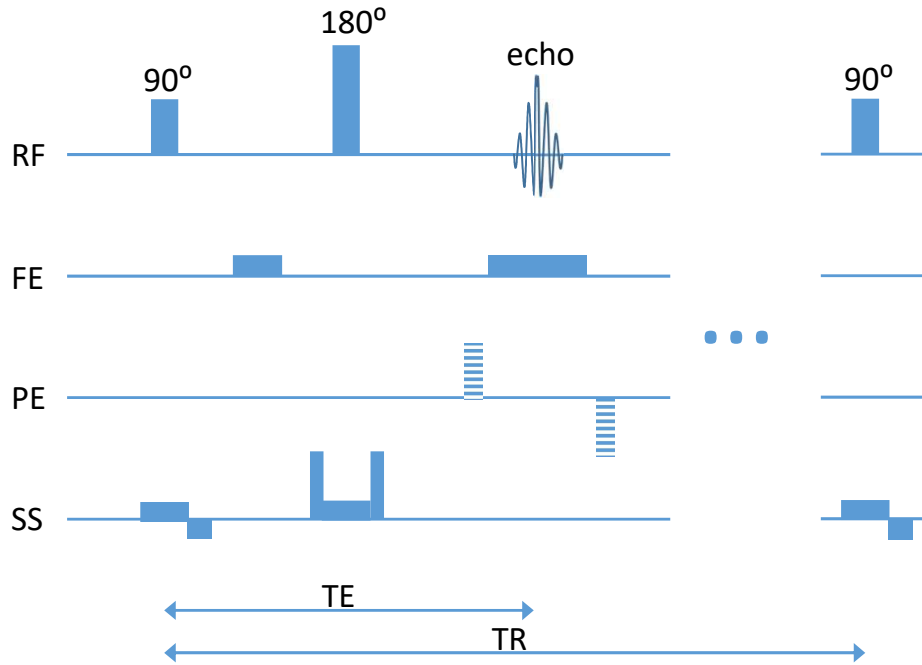
Figure 1.2: An example of a 2D spin echo pulse sequence is shown. One line of k-space is filled per TR. RF pulses and signal are shown on the RF line. Slice select (SS), phase encode (PE), and frequency encode (FE) gradients are also shown.

Carr Purcell Meiboom Gill Sequence

The Carr Purcell Meiboom Gill (CPMG) [10, 11] sequence is a multi-echo spin echo pulse sequence consisting of a 90° pulse followed by a train of 180° pulses which are 90° out of phase. The relatively short echo spacing allows for T2 to be quantified without appreciable effects of diffusion [11]. The phase shift is intended to reduce the effects of imperfect 180° refocussing pulses [10]. Multi-echo spin echo sequences used in this work are CPMG sequences.

An example of a slice selective three echo CPMG sequence is shown in Figure 1.3.

During each TR, each echo fills one line of k-space in the image for that echo. In a multi-slice implementation, after the echo is acquired, before the next excitation pulse,
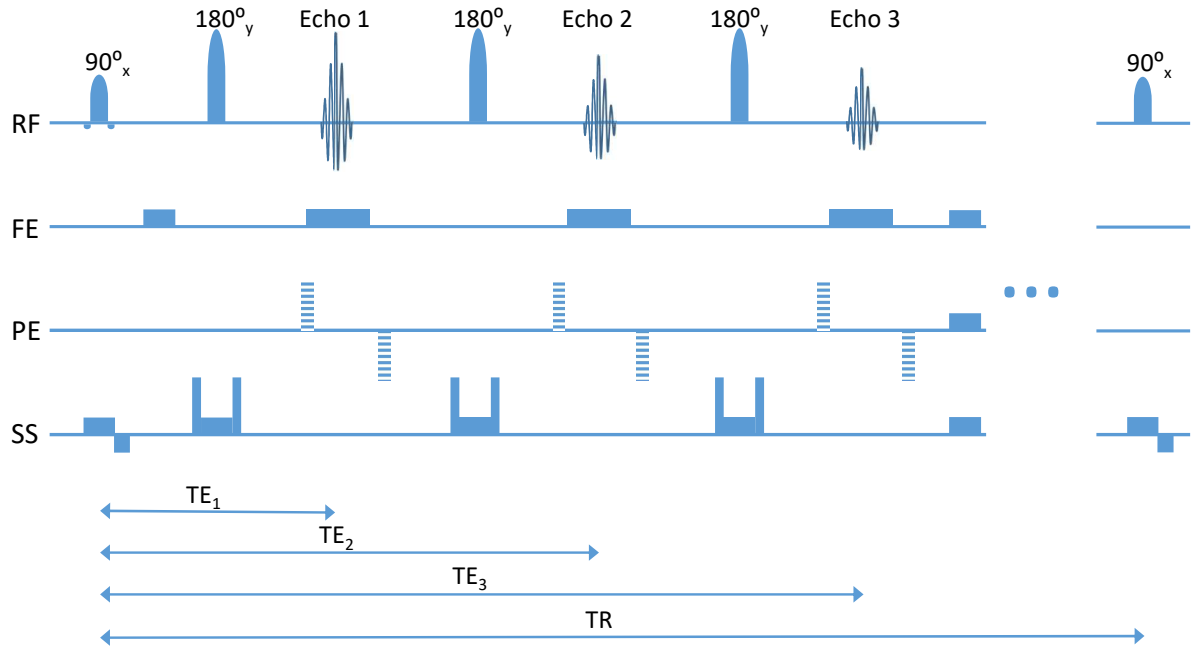
Figure 1.3: An example of a three echo CPMG sequence is shown. RF pulses and signal are shown together on the RF line. Slice select (SS), phase encode (PE), and frequency encode (FE) gradients are also shown.

Fast Spin Echo

Fast Spin Echo (FSE), also referred to as Turbo Spin Echo (TSE) or Rapid Acquisition with Relaxation Enhancement (RARE), is an accelerated spin echo sequences [12]. Image acquisition is accelerated according to the number of echoes acquired in a multi-echo sequence, and each echo fills a different line of k-space. Image contrast is determined based on the low frequency information encoded at the centre of k-space. Thus, the echo which fills the central line of k-space (corresponding to the zero frequency) will determine the contrast of the image. The image may be acquires such that any of the echoes in the sequence define the contrast, and thus is referred to as the effective echo time. Typically, phase encoding will be ordered such that the effective echo fills the central area of k-space, and other echoes are ordered to minimize discontinuities in the phase encoding direction

11

(intensity will be modulated by T2 decay) which can cause blurring and ringing.
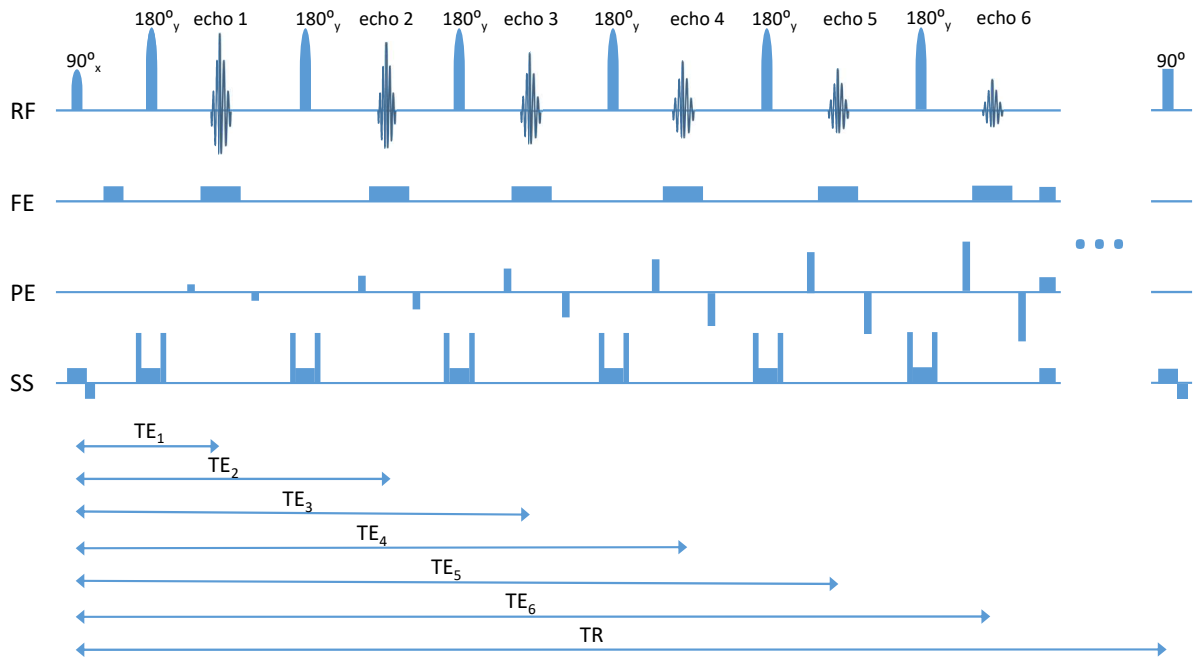
Figure 1.4: An example of a six echo fast spin echo sequence is shown. Each echo fills a different line of k-space. Image acquisition is accelerated by the number of echoes in the train, for a single contrast FSE. Image contrast is dominated by the echo which fills the centre of k-space.

An example of a slice selective six echo FSE sequence is shown in Figure 1.4. The displayed sequence uses $180°$ refocussing pulses. Frequently lower refocussing angles are employed in order to reduce the RF power deposited[3]. Six lines of k-space are acquired per TR. An example of how k-space may be ordered is shown in Figure 1.5 for this six echo sequence. The diagram shows centric k-space ordering (the first echo fills the centre of k-space, and subsequent echoes will fill further out).

---

[3]Power deposited by RF pulses results in RF heating, and power increases approximately as the square of field strength and patient size. Specific Absorption Rate (SAR = absorbed power / mass) is used to estimate increased temperature. The SAR of a sequence is estimated by the cumulative energy deposited by all RF pulses, the TR, and the patient weight. Pulse sequences with many RF pulses of high flip angles, such as FSE or MESE, result in high SAR. In order to reduce SAR, without reducing echo train lengths or reducing slice coverage, refocussing angles are often reduced. Under normal conditions, whole body SAR should be limited to 2 W/kg in the whole body, and 3.2 W/kg in the head, or a maximum rise in core temperature of $0.5°C$ [13]
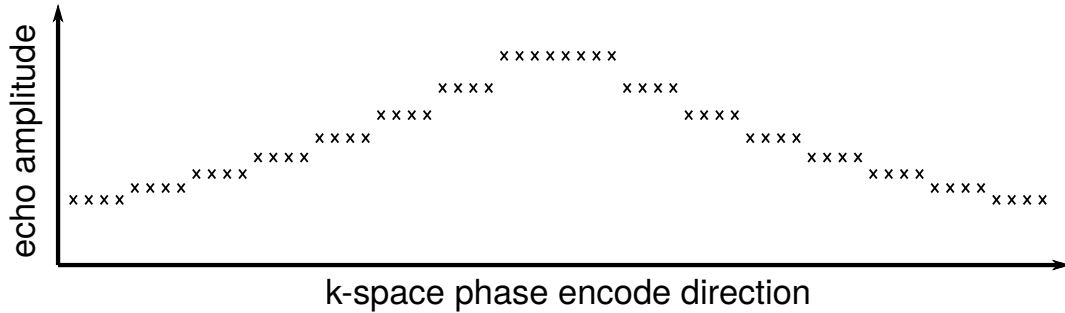
Figure 1.5: An example of how k space may be ordered is shown. The first echo fills the centre of k-space. Subsequent echoes fill out k-space around it.

Inversion Prepared FSE

The contrast of an FSE sequence may be modified by using an inversion preparation pulse. An inversion pulse is applied, then some time later the magnetizaiton is tipped into the trainsverse plane, and the FSE readout train is applied. The time between the initial inversion and $90°$ is the inversion time (TI). Different T1 values of different tissues will result in image contrast, as magnetization recovers at different rates. If this is optimized such that fluids (e.g. cerebral spinal fluid) will have approximately zero longitudinal magnetization at the inversion time, this is called a FLuid Attenuated Inversion Recovery (FLAIR). Any effective echo may be used. FLAIR images are frequently acquired as T2-weighted.

1.2 Measuring Relaxation Rates

1.2.1 Longitudinal Relaxation

Many techniques exist to measure T1 relaxation. To measure T1, we must excite the magnetization and observe recovery to equilibrium. The gold standard experiment for this measurement is inversion recovery. A series of inversion prepared sequences (an inversion prepared FSE sequences is shown in figure 1.6) with a range of inversion times are acquired. Images should be acquired with a long repetition time to allow for full recovery of magnetization, and a short echo time to minimize T2 weighting. Images with
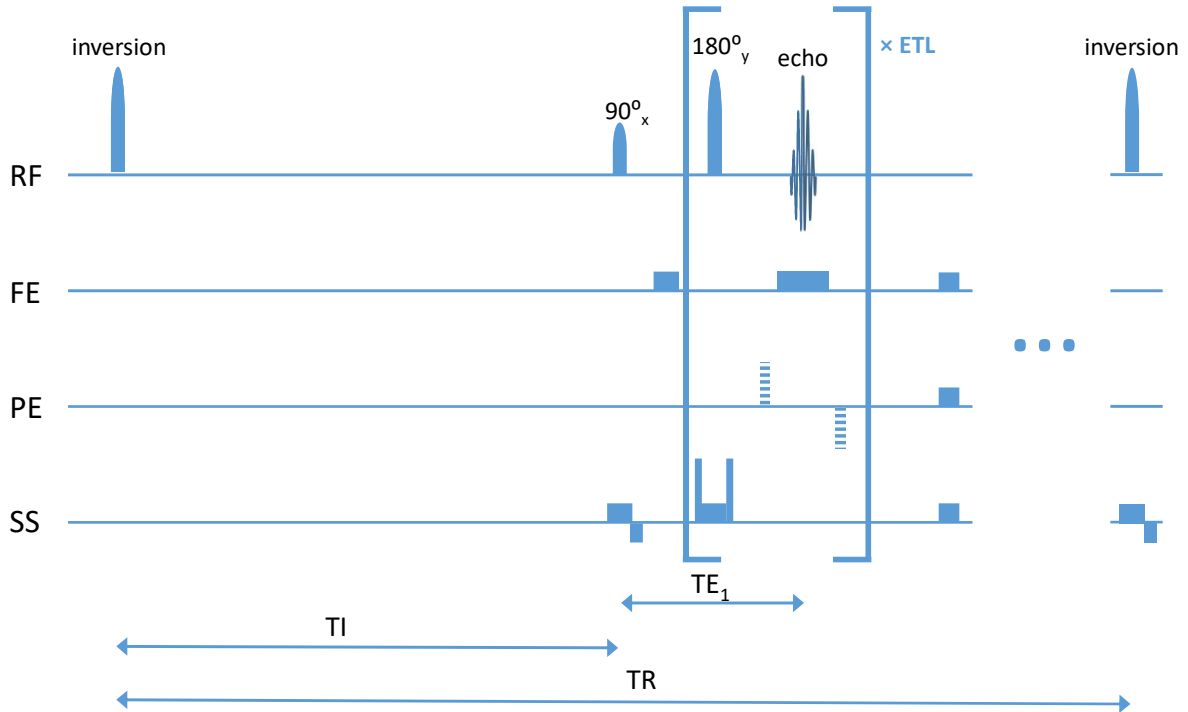
Figure 1.6: An example of an inversion prepared fast spin echo sequence is shown. A FSE sequence is precluded by an inversion pulse followed by some amount of waiting, in which spins have time to recover. Contrast will be determined by the relative amount of recovery in adjacent tissues (T1 weighting) and the effective echo time of the FSE readout (T2 weighting).

inversion times (TI) spanning the full inversion recovery curves should be used. The equation $S = S_0(1 - 2e^{-TI/T1})$ may be fit to the data either voxel by voxel, or using regions of interest. Where perfect inversion cannot be assumed (as in realistic medical imaging circumstances), inversion efficiency (f) should be included in the fitting model: $S = S_0(1 - fe^{-TI/T1})$, as shown in Figure 1.7d. Due to the requirement of a long TR, and many inversion times for accurate fitting, T1 measurement can be time consuming, particularly in tissues with long T1. As a result, inversion recovery experiments are not acquired clinically.

1.2.2 Transverse Relaxation

T2 may be measured using a standard CPMG experiment (discussed in Section 1.1.5). For a precise 180° refocussing, the amplitude of the spin echoes will exhibit exponential
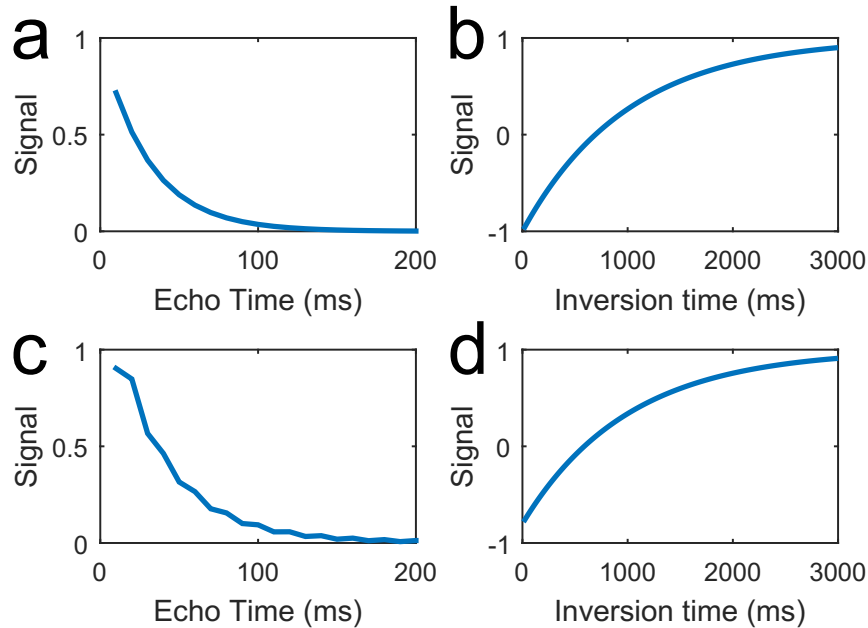
Figure 1.7: From basic MR principles, we expect T2 to be observed as (a) exponential decay, and T1 to be observed as (b) exponential recovery following perfect inversion. In practice, (c) multi-echo sequences are not observed to have pure exponential decay due to contributions from alternative echo pathways when refocussing pulses are not precisely 180°, and (d) imperfect inversion is observed in inversion recovery experiments.

decay with time constant T2. However, this requires perfect 180° refocussing pulses, otherwise stimulated echoes occur [14–16]. Stimulated echoes are a form of echo following two or more refocussing pulses (which are not perfect 180°) where magnetization has been stored in the longitudinal plane. More specifically, consider a train of three 90° pulses in rapid succession: following the first pulse, all magnetization will fall on the transverse plane. After the second pulse, the magnetization will be tipped to the -M_z axis; after the third, the magnetization will again be tipped into the transverse plane. In between the first and second pulse, transverse relaxation will decay the transverse magnetization. After the second pulse, that magnetization will be stored in the longitudinal axis, where T2 decay does not occur. Once the magnetization is returned to the transverse plane, it will have only experienced a T2 decay for part of the sequence. The echo resulting from spins which were stored in the longitudinal axis is referred to as a stimulated echo. While this example is extreme, it is obvious that following the third pulse, the resulting spin echo will contain magnetization which as not experienced T2 decay for the full time

15

between excitation and the echo time. Contributions from such alternate echo pathways increase the amplitude of later echoes, causing overestimation of T2. In MRI, perfect 180° refocussing is impossible due to through-plane (slice profile) variation, B1 calibration errors, and RF inhomogeneity [17, 18] (particularly at field strengths $\geq 3.0\text{T}$)[4].

Even in areas where the flip angles achieved are the angles requested, the slice profile results in a range of flip angles contributing to the resulting signal, resulting in stimulated echoes. Simulated slice profiles are shown in Figure 1.8. The shape of the resulting decay curve depends on the model used for simulating RF pulses, as demonstrated in Figure 1.9.

1.3 Modelling Multi-Echo Spin Echo Pulse Sequences

Modelling of multi-echo pulse sequences falls into two categories: extended phase graph, or Bloch equation modelling. Simulated echo amplitudes depend on the model used for simulating slice profiles (though EPG and Bloch simulations result in identical curves for non-selective modelling). Examples of T2 decay curves modelled using slice selective Bloch simulations with RF pulses modelled using the SLR algorithm, slice selective EPG [14] and non-selective RF pulses are shown in Figure 1.9. The pulses shapes used for these simulations are shown in Figure 1.8. The use of these methods for T2 relaxometry is described and compared in detail in Chapter 2. Explanations of each modelling technique are included below.

1.3.1 Bloch Equation Modelling

Bloch equations may be solved in order to determine the evolution of magnetization vectors with time, in the presence of magnetic field gradients, or RF fields. The evolution of the magnetization vector $\vec{M}(t) = [M_x(t), M_y(t), M_z(t)]$ may be described by the Bloch

---

[4]The wavelength of the RF pulse in tissue may be calculated by $\lambda = \frac{\lambda_0}{\sqrt{\epsilon/\epsilon_0}} = \frac{c/\omega_0}{\sqrt{\epsilon/\epsilon_0}}$. In tissue at high field (defined here as $\geq 3\text{T}$) , this becomes close to the size of the human head, resulting in interference, and non-uniform B_1 fields
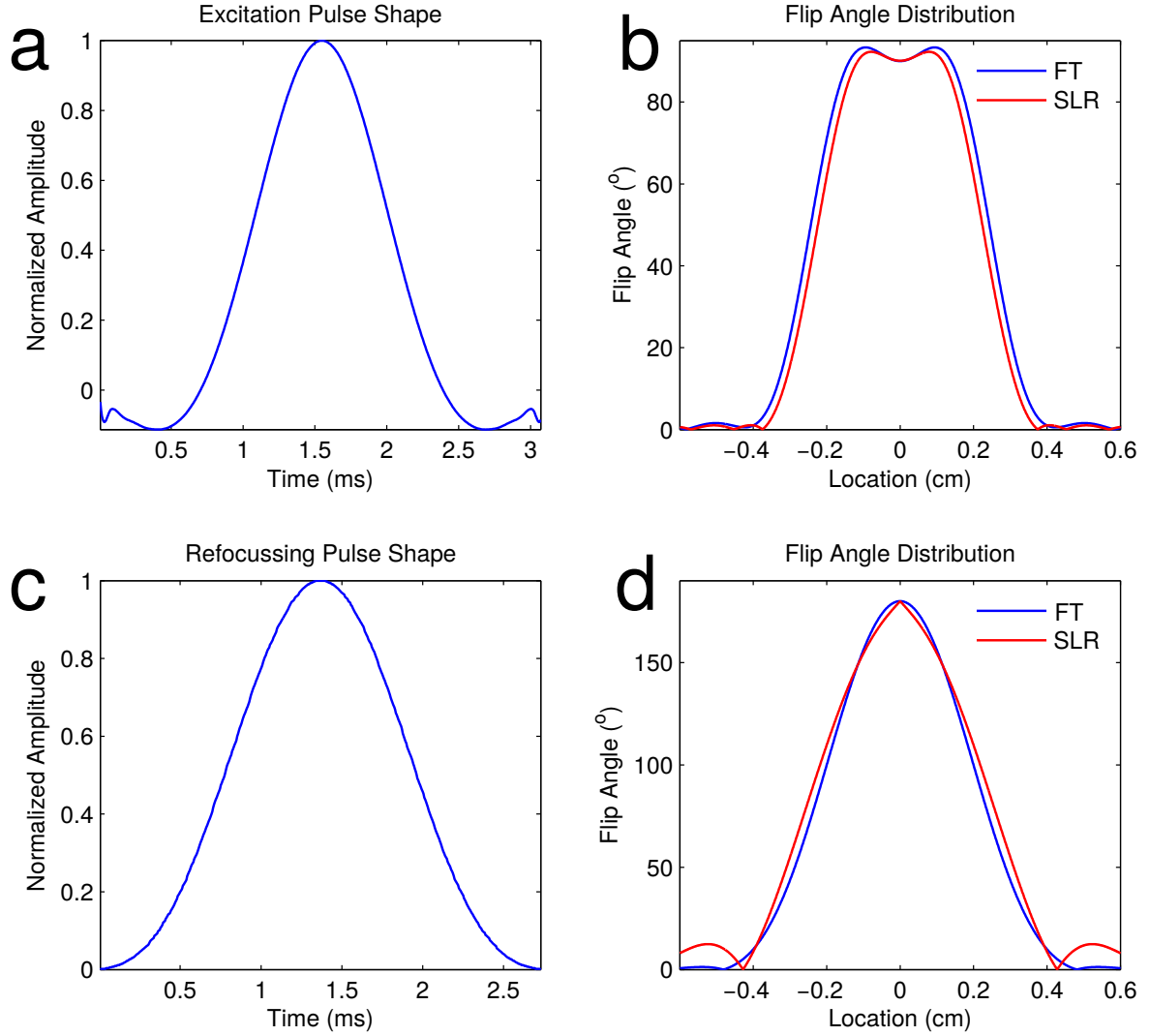
Figure 1.8: (a) A 90° excitation pulse shape and (b) the resulting flip angle distribution modelled using a Fourier Transform (FT) approximation (blue) and using the SLR algorithm (red) are shown in the top row. The bottom row shows (c) a 180° refocussing pulse, and (d) corresponding flip angle distributions. The simulation reflects parameters used for a 2D acquisition with 3 mm slice thickness.

equations. The Bloch equations in the rotating frame are [3]:

$$
\frac{d}{dt}
\begin{bmatrix} M_x \\ M_y \\ M_z \end{bmatrix}
= \gamma
\begin{bmatrix}
0 & \vec{G} \cdot \vec{r} & -B_1 \sin(\phi) \\
-\vec{G} \cdot \vec{r} & 0 & B_1 \cos(\phi) \\
B_1 \sin(\phi) & -B_1 \cos(\phi) & 0
\end{bmatrix}
\begin{bmatrix} M_x \\ M_y \\ M_z \end{bmatrix}
+
\begin{bmatrix}
(1/T_2) M_x \\
(1/T_2) M_y \\
(1/T_1)(1 - M_z)
\end{bmatrix}
\quad (1.20)
$$
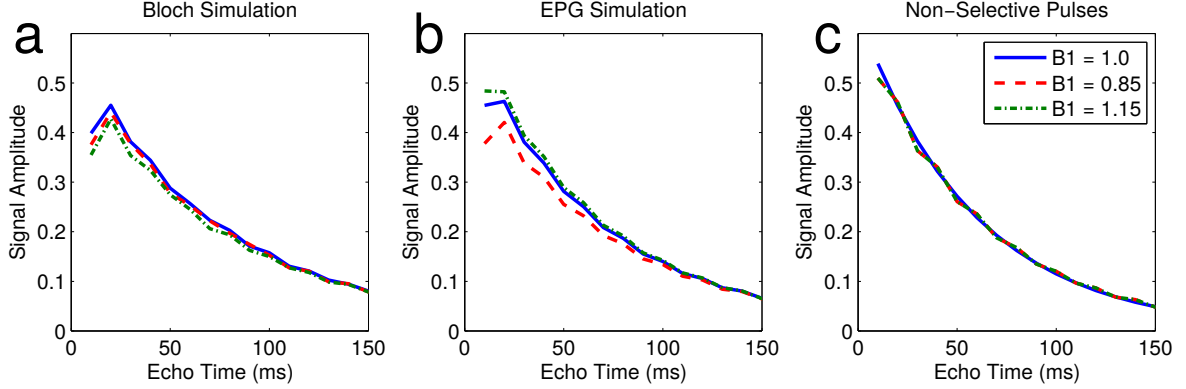
Figure 1.9: A multi-echo spin echo sequence is modelled using (a) slice selective Bloch Simulations, (b) slice selective EPG simulation, and (c) non-selective pulses. Each sequence was simulated with a range of B1 values corresponding to 180°, 153°, and 207° refocussing angles.

where B_1 and ϕ are the amplitude and phase of the RF pulse, $\vec{G}$ is the slice selection gradient, $\vec{r}$ is the location relative to the location where G=0. This may be simplified by assuming that T_1 and T_2 are long relative to the RF pulse duration:

$$\frac{d}{dt}\begin{bmatrix} M_x \\ M_y \\ M_z \end{bmatrix} = \gamma \begin{bmatrix} 0 & \vec{G} \cdot \vec{r} & -B_1 \sin(\phi) \\ -\vec{G} \cdot \vec{r} & 0 & B_1 \cos(\phi) \\ B_1 \sin(\phi) & -B_1 \cos(\phi) & 0 \end{bmatrix}\begin{bmatrix} M_x \\ M_y \\ M_z \end{bmatrix} \tag{1.21}$$

Pulse sequences may be modelled by employing solutions to these equations. Generally, employing Taylor expansions (such as implemented in [19]) or numerical ordinary differential equation solvers (e.g. in Matlab) are time consuming. RF pulses may be simulated using a hard pulse approximation, as implemented in The Shinnar-Le Roux Algorithm [20].

1.3.2   Shinnar-Le Roux Algorithm

The Shinnar-Le Roux (SLR) algorithm is based on a discrete approximation to the spin domain version of the Bloch equation. The algorithm is described in detail Pauly et al [20]. The forward SLR transform is summarized here.

The SLR algorithm relates an RF pulse shape with two complex polynomial functions

$$[B_1(t), \phi(t)] \leftarrow SLR \rightarrow [A_N(z), B_N(z)] \tag{1.22}$$

where $B_1(t)$ and $\phi(t)$ are the amplitude and phase of the RF pulse as a function of time. N refers to the number of hard pulse divisions $B_1(t)$ is approximated by. A_N and B_N are polynomials of order (N-1), and $z = e^{i\omega\Delta t}$

The Bloch equation reduces to a rotation if relaxation effects are neglected. The solution may be written as the initial magnetization multiplied by a 3×3 orthonormal matrix. The rotation may also be represented by 2×2 unitary matrices

$$Q = \begin{bmatrix} \alpha & -\beta^* \\ \beta & \alpha^* \end{bmatrix} \tag{1.23}$$

where α and β are the Cayley-Klein parameters, which relate to the axis of rotation $\hat{n}$ and rotation angle ϕ

$$\alpha = \cos(\phi/2) - i\hat{n}_z \sin(\phi/2) \tag{1.24}$$

$$\beta = -i(\hat{n}_x + i\hat{n}_y)\sin(\phi/2) \tag{1.25}$$

The magnetization following an RF pulse $\vec{M}^+$ may be related to the magnetization prior to the pulse $\vec{M}^-$ by:

$$\frac{d}{dt} \begin{bmatrix} M_{xy}^+ \\ M_{xy}^{+*} \\ M_z^+ \end{bmatrix} = \begin{bmatrix} (\alpha^*)^2 & -\beta^2 & 2\alpha^*\beta) \\ -(\beta^*)^2 & \alpha^2 & 2\alpha\beta^* \\ -\alpha^*\beta^* & -\alpha\beta & \alpha\alpha^* - \beta\beta^* \end{bmatrix} \begin{bmatrix} M_{xy}^- \\ M_{xy}^{-*} \\ M_z^- \end{bmatrix}. \tag{1.26}$$

where $M_{xy} = M_x + iM_y$ [20].

Shaped RF pulses may be considered as piecewise constant, and treated as a set of N rectangular pulses. This hard pulse approximation may be used to map an RF pulse into two complex polynomials we call the forward SLR transform. Briefly, the RF pulse is divided into N discrete steps, and each step is treated as a hard pulse (instantaneous rotation). If the angle is small, the rotation can be modelled by two sequential rotations:

free precession under the effect of the local gradient field by an angle $-\gamma Gx\Delta t$, and rotation about the applied RF vector by angle $\gamma B_1 \Delta t$. The states space recursion for the Cayley-Klein parameters is

$$\begin{bmatrix} \alpha_j \\ \beta_j \end{bmatrix} = z^{1/2} \begin{bmatrix} C_j & -S_j^* \\ S_j & C_j \end{bmatrix} \begin{bmatrix} 1 & 0 \\ 0 & z^{-1} \end{bmatrix} \begin{bmatrix} \alpha_{j-1} \\ \beta_{j-1} \end{bmatrix} \tag{1.27}$$

where $C_j = \cos(\gamma|B_{1,j}|\Delta t/2)$, $S_j = ie^{i\angle B_{1,j}}\sin(\gamma|B_{1,j}|\Delta t/2)$, and $z = e^{i\gamma Gx\Delta t}$.

These may be re-expressed using

$$A_j = z^{j/2}\alpha_j \tag{1.28}$$

$$B_j = z^{j/2}\beta_j \tag{1.29}$$

to obtain

$$\begin{bmatrix} A_j \\ B_j \end{bmatrix} = z^{1/2} \begin{bmatrix} C_j & -S_j^* z^{-1} \\ S_j & C_j z^{-1} \end{bmatrix} \begin{bmatrix} A_{j-1} \\ B_{j-1} \end{bmatrix}. \tag{1.30}$$

Given $A_0 = \alpha_0 = 1$ and $\beta = 0$, the Cayley-Klein parameters at the nth time step are (n-1) order polynomials of z^{-1}:

$$A_n(z) = \sum_{j=0}^{n-1} a_j z^{-j} \tag{1.31}$$

$$B_n(z) = \sum_{j=0}^{n-1} b_j z^{-j} \tag{1.32}$$

where $z^{-1} = e^{-i\gamma Gx\Delta t}$, reducing the representation of a selective RF pulse from n 3×3 matrices to two (n-1)-order polynomials.

1.3.3 Extended Phase Graph Algorithm

The extended phase graph (EPG) [16, 21] (also described by Weigel [22]) provides a simple tool for understanding the magnetization response of a multi-echo sequences. Effects of gradients, RF pulses, relaxation and motion phenomena may be characterized by a few

matrix operations on configuration states [22].

Given initial magnetization (M_x, M_y, M_z). an RF pulse may be treated as a simple rotation about the x axis:

$$
\begin{bmatrix} M_x^+ \\ M_y^+ \\ M_z^+ \end{bmatrix} = \begin{bmatrix} 1 & 0 & 0 \\ 0 & \cos\alpha & \sin\alpha \\ 0 & -\sin\alpha & \cos\alpha \end{bmatrix} \begin{bmatrix} M_x \\ M_y \\ M_z \end{bmatrix}
\tag{1.33}
$$

where (M_x^+, M_y^+, M_z^+) is the magnetization immediately following an RF pulse with flip angle α, rotating around the x axis is given by [16]:

$$
M_x^+ = M_x
\tag{1.34}
$$

$$
M_y^+ = M_y \cos\alpha - M_z \sin\alpha
\tag{1.35}
$$

$$
M_z^+ = M_y \sin\alpha + M_z \cos\alpha
\tag{1.36}
$$

If we consider transverse magnetization $M_T = M_x + iM_y$, we can reformulate these equations to treat any RF pulse of angle θ to be a weighted combination of 0°, 90° and 180° pulses resulting in transitions between longitudinal and transverse states:

Transition	Weight
$M_T \longrightarrow M_T$	$\cos^2(\theta/2)$
$M_T \longrightarrow M_T^*$	$\sin^2(\theta/2)$
$M_z \longrightarrow M_y$	$\sin(\theta)$
$M_z \longrightarrow M_z$	$\cos^2(\theta/2)$
$M_z \longrightarrow -M_z$	$\sin^2(\theta/2)$
$M_y \longrightarrow M_z$	$\sin(\theta)$

Each pulse results in the magnetization splitting into different pathways. An example of a phase diagram for a multi-echo spin echo sequence is displayed in Figure 1.10. Echoes occur where phase lines cross the zero phase line. Three pathways are highlighted to show a direct spin echo (green), stimulated echo (blue) and an indirect pathway (red). Only the first echo is a pure spin echo. Subsequent echoes are contaminated by alternate echo pathways, unless refocussing angles are precisely 180°. Relaxation may be accounted for when calculating echo amplitudes by including decay between RF pulses. It is assumed

that strong crusher gradients fully dephase non-refocused magnetization.
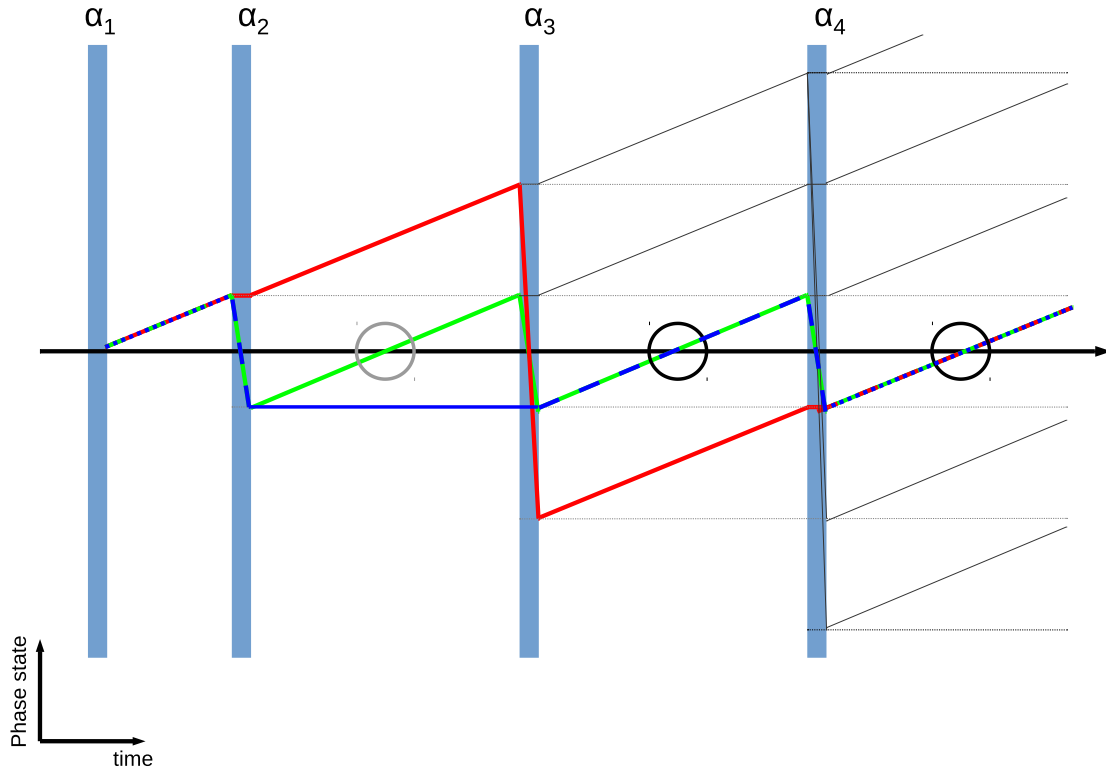
Figure 1.10: An EPG diagram showing a multi-echo spin echo sequence with four RF pulses is shown. All pathways are indicated in black. Vertical lines indicate the RF pulses (flip angles $\alpha_1, \alpha_2, \alpha_3, \alpha_4$). Horizontal and slanted lines indicate echo pathways. Diagonal lines indicate phase evolution of transverse states, while horizontal lines indicate phase storage. Three pathways are highlighted: the green line indicates a pure spin echo pathway, the blue line indicates a stimulated echo pathway, the red line indicates an indirect echo pathway. The first echo is the only true spin echoes. Subsequent echoes contain components from alternate pathways, unless refocussing pulses are precisely 180°.

The original description by Hennig does not allow for calculations including slice profile. Rather, exactly flip angles must be known. This method was extended by Lebel and Wilman [14] to include an approximation of the effect of slice profile. Briefly, a distribution of flip angles is calculated by taking the Fourier transform of the RF pulse envelope. Decay curves are computed using the EPG algorithm for each angle in the distribution (effectively, at each location across the slice profile), and then decays are summed together to estimate the total decay curve. An example is shown in Figure 1.11.
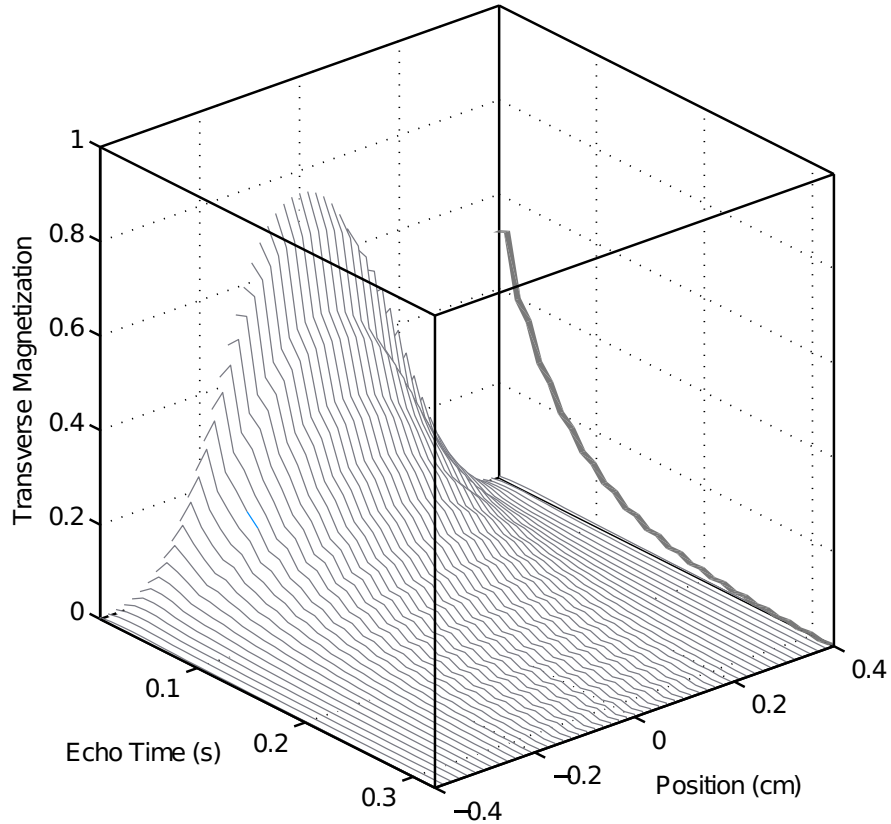
Figure 1.11: Slice selection is included in EPG by using a distribution of flip angles across the slice width. Decays are computed at each location and summed, as shown.

1.4   Flip Angle Mapping

Flip angle varies across the volume of interest due to RF interference effects. At high field (defined here as $\geq$ 3T), this effect is at pronounced due to the wavelength of the RF field being close to the size of the human head. The wavelength of the RF pulse in tissue may be calculated by $\lambda = \frac{\lambda_0}{\sqrt{\epsilon/\epsilon_0}} = \frac{c/\omega_0}{\sqrt{\epsilon/\epsilon_0}}$. A simple approach to flip angle mapping is the double angle method [23]. For a sequence with long repetition time relative to T1, the signal of a sequence using excitation angle α is proportional to $\sin(\alpha)$. If a pair of images are acquired with excitation angles α and 2α, their relative signal intensity becomes

$$\frac{S(2\alpha)}{S(\alpha)} = \frac{\sin(2\alpha)}{\sin(\alpha)} = 2\cos(\alpha) \tag{1.37}$$

and thus

$$\alpha = \frac{1}{2} \arccos \left(\frac{S(2\alpha)}{2S(\alpha)} \right) \tag{1.38}$$

neglecting non-ideal slice profile [24]. Ideally, the chosen flip angles should be equally spaced around 90°: typically nominal flip angles are chosen as $\alpha = 60°$ and 120°. If the flip angles used are too small or very large (either due to large interference effects or poor choice of prescribed angle), near the zero crossings, the sinusoidal function is approximately linear, and flip angles will not be measured accurately.

1.5   Motivation and Overview

The collection of weighted images is common in clinical practice. The contrast in weighted images is determined by the relative parameters related to their weighting (for example, proton density, T1, T2, T2* or diffusion), but also on parameters specific to the hardware and MRI sequence being used. For example, image intensity may be modified by RF inhomogeneity, sensitivity profile of the receiver coils, receiver gain, or artefacts related to motion, acceleration techniques, or other aspects of the pulse sequence. Quantitative MRI aims to overcome biases in images due to acquisition, and allow for comparison of data regardless of where it was acquired by removing dependence on these nuisance parameters [7]. Quantitative relaxation mapping provides a more specific means to monitor changes in tissue. There is a need for non-invasive biomarkers to monitor changes in tissues related to biological processes, disease, and medical intervention [25].

Quantitative MRI may improve knowledge of pathological processes, and potentially be used for defining within individuals severity of disease, prognosis, or rate of disease progression [7]. On a larger scale, quantitative MRI which is reproducible across vendors and scanners can allow for large scale multi-centre studies which may detect small effects due to disease processes or variations between populations [26]. This can be particularly important for investigation of rare diseases, as detection of small changes requires many subjects. Relaxation mapping has demonstrated variation in T1 and T2 values within specific brain regions in neurodevelopment [27, 28], multiple sclerosis (MS) [29–33], intracranial tumours [34, 35], unipolar disorder [36], Alzheimer's disease [37], epilepsy [38, 39],

and many other diseases and biological processes. Relaxation mapping has potential for clinical usage where it can demonstrate changes which are difficult or impossible to detect with conventional imaging. For example, relaxation mapping has been shown to be useful for delineation of tumours [35], detection of tumour progression [40], detecting changes in normal appearing white matter in multiple sclerosis [32, 41], and identifying abnormalities in hippocampus in intractable partial epilepsy [39]. In general, changes in T1 and T2 relaxation times are indicative of changes in tissue microenvironment.

Relaxation measurements are non-specific. Changes in microenvironment, such as demyelination, tumour growth, or injury may result in changes in relaxation rates due to changes in the water environment. However, the presence of macromolecules, or iron content also plays a role. Accumulation of iron in the brain has been demonstrated in multiple sclerosis [42], Alzheimer's disease [37] and ageing [43, 44]. T2 is sensitive to iron content in tissue [37, 42, 45]. Specifically, iron content in grey matter has been shown to have a linear relationship with 1/T2 in healthy subjects [45]. T2 has been shown to have excellent correlation with iron content in normals [46], and this effect increases with higher magnetic fields. My own laboratory has also shown significant T2 changes in MS [30, 31, 47].

In this work, only the human brain is examined. However, T2 quantification is frequently used for characterization of tissues in vivo, including examination of joints [48–51], muscle [52, 53], liver [54–56] and heart [54, 57–59].

The most common approach to T2 measurement is fitting of multi-echo spin echo data. Imperfect refocussing due to radiofrequency interference [60], slice profile (Figure 1.8) [61], or purposeful reduction in refocussing angles all result in indirect and stimulated echoes, which contaminate the signal decay [14, 16]. An obvious indicator of substantial contamination from stimulated echoes is an increased magnitude of the second echo relative to the first echo, such as shown in Figure 1.9. Fitting such data with standard exponential fitting ($S = S_0 e^{-TE/T2}$) will result in T2 mis-estimation [62].

Error in T2 from exponential fitting varies with T2 and the amount of stimulated echo contamination [14]. The amount of stimulated echo contamination in an echo depends on refocussing slice profile (determined by flip angle and RF pulse shape). RF interference

results in variable refocussing angles within the imaging field, particularly at high field. RF pulse shape is non-standard and can vary between scanners, vendors, or with sequence parameters. Echo spacing and the number of echoes available for fitting would also affect results [63]. When only exponential fitting is employed, these biases may preclude the ability to compare results across studies, compare results from multi-centre studies, which may not use identical MR systems, or in general, compare T2 values from any experiments where scan parameters are different.

The first main goal of this thesis is to examine and improve upon available methods for T2 quantification from multiple spin echoes. More specifically, to identify the accuracy and limitations of available methods, and to improve upon available methodology such that biases in T2 quantification specific to the scanner and sequence parameters and limitations of these methods are both minimized and understood. Chapters 2 and 3 of this thesis are dedicated to filling this gap in knowledge and expanding on existing methods.

Methods exist which yield accurate T2 despite imperfect refocusing by employing computational modelling of the signal response for all echo pathways [14, 64]. Direct fitting of the spin response for T2 quantification is an area of active research using methods such as stimulated echo compensation with echo phase graph [14, 63, 65–68], or full Bloch modelling [64] for modelling of echo pathways. These methods employ different models for simulation of multi-echo spin echo decay curves, but aim to achieve the same goal: to determine both the T2 and the refocusing flip angles from the fitting process. Differences in T2 values from these two methods have not previously been studied, nor has the accuracy of the inherent flip angle map produced by these methods. Further, EPG approximates the slice profile with a Fourier Transform of the RF pulse shape. Use of a more accurate slice profile model has not been previously investigated. These methods are examined in detail in Chapter 2.

Despite the availability of methods for more advanced fitting, expert use is still necessary for implementation, and these methods require knowledge of detailed sequence parameters including exact flip angle trains and RF pulse shapes. Not all vendors make knowledge of detailed sequence parameters openly available. Use of exponential fitting

26

remains persistent [49, 50, 55, 57, 69–71] due to its simplicity and ease of implementation. Some researchers use exponential fitting for T2, and simply acknowledge stimulated echoes as a limitation in their study [50, 55, 57, 69]. Other researchers have used simple remedies to attempt to limit the effects of stimulated echoes by removing echoes but still using an exponential fit, either skipping the first echo in the train [38, 48, 52, 72–79] or all odd echoes [54, 80]. Both of these approaches improve fit quality, and are assumed to reduce errors in T2 fitting caused by indirect and stimulated echo contamination. However, the accuracy of skipped echo methods has not previously been fully examined. In Chapter 3, the effectiveness of these simple remedies for T2 measurement is examined by comparing to a Bloch modelling approach.

Relaxation mapping is a powerful quantitative MRI method, but it is not widely used because of its difficulty to implement at high magnetic field (as described above) and the need for specialized pulse sequences, and hence additional imaging time, which is not feasible in standard clinical practice. However, there is demand for rapid quantification of relaxation maps. Some authors have attempted this by directly fitting weighted images [37, 44, 81–89] or through use of specialized sequences (for example, DESPOT1 and DESPOT2 [90, 91], QRAPMASTER [92, 93], or Fingerprinting [94, 95]). Further, weighted images are frequently acquired in clinical and research exams, and the question of how that data may be used quantitatively is of active interest in the research community [96].

The second main goal of this thesis is to enable wider use of accurate relaxation quantification. Based on the developed methods and knowledge of limitations of available models from Chapters 2 and 3, the focus of the second half of this thesis is to develop means which enable accurate T1 and T2 quantification using only relaxation-weighted fast spin echo pulse sequences. Weighted images are frequently acquired in clinical and research exams. Methods to enable quantitative relaxometry from standard radiology sequences could allow for wider use of relaxation mapping methods, where time for dedicated sequences is not available. Furthermore, such methods have the potential to enable retrospective quantitative analysis of existing qualitative clinical and research data. Chapters 4 and 5 are dedicated to achieving this second goal.

Previous work [14, 63–68] required multiple echoes to obtain satisfactory fitting conditions for three fitting parameters (T2, flip angle, initial signal amplitude), which requires multiple echoes (in practice, at least four [63], but typically many more). Differences between T2 values obtained from exponential fitting of MESE experiments and pairs (or sets) of FSE images have been previously noted [97, 98]. In addition, inter-site studies have noted systematic differences between sites and vendors in T2 maps calculated from exponential fitting of pairs of PD and T2-weighted fast spin echo images [81]. Novel means to acquire T2 maps from standard PD and T2-weighted images are demonstrated in Chapter 4. In Chapter 5, it is demonstrated that with the addition of a T1-weighted image, T1 may also be estimated.

References

[1] David J. Griffiths. *Introduction to Quantum Mechanics.* Pearson, Upper Saddle River, NJ, 2 edition, March 2004.

[2] Dwight G. Nishimura. *Principles of Magnetic Resonance Imaging.* Stanford Univ, 1.1 edition, February 2010.

[3] E. Mark Haacke, Robert W. Brown, Michael R. Thompson, and Ramesh Venkatesan. *Magnetic Resonance Imaging: Physical Principles and Sequence Design.* Wiley-Liss, 1st edition, June 1999.

[4] John C. Gore and Richard Kennan. Chapter 3: Physical and Physiological Basis of Magnetic Relaxation. In *Magnetic Resonance Imaging.* Mosby, 1999.

[5] N. Bloembergen, E. M. Purcell, and R. V. Pound. Relaxation Effects in Nuclear Magnetic Resonance Absorption. *Physical Review,* 73(7):679, April 1948. 05294.

[6] Marinus T. Vlaardingerbroek and Jacques A. den Boer. *Magnetic Resonance Imaging.* Springer, 2 edition, January 1999.

[7] Paul Tofts. *Quantitative MRI of the Brain: Measuring Changes Caused by Disease.* Wiley, 1 edition, October 2003.

[8] Irene M. Vavasour, Kenneth P. Whittall, David K.B. Li, and Alex L. MacKay. Different magnetization transfer effects exhibited by the short and long T2 components in human brain. *Magnetic Resonance in Medicine,* 44(6):860–866, 2000.

[9] E. L. Hahn. Spin Echoes. *Physical Review,* 80(4):580–594, November 1950.

[10] H. Y. Carr and E. M. Purcell. Effects of Diffusion on Free Precession in Nuclear Magnetic Resonance Experiments. *Physical Review,* 94(3):630–638, May 1954. 04664.

[11] S. Meiboom and D. Gill. Modified Spin-Echo Method for Measuring Nuclear Relaxation Times. *Review of Scientific Instruments*, 29:688–691, August 1958.

[12] J. Hennig, A. Nauerth, and H. Friedburg. RARE imaging: A fast imaging method for clinical MR. *Magnetic Resonance in Medicine*, 3(6):823–833, December 1986.

[13] R. J. Stafford. High Field Mri - Technology, Applications, Safety, and Limitations. *Medical Physics*, 31(6), June 2004.

[14] R. Marc Lebel and Alan H. Wilman. Transverse relaxometry with stimulated echo compensation. *Magnetic Resonance in Medicine*, 64(4):1005–1014, 2010.

[15] S. Majumdar, S. C. Orphanoudakis, A. Gmitro, M. O'Donnell, and J. C. Gore. Errors in the measurements of T2 using multiple-echo MRI techniques. I. Effects of radiofrequency pulse imperfections. *Magnetic Resonance in Medicine*, 3(3):397–417, 1986.

[16] Jürgen Hennig. Echoes - how to generate, recognize, use or avoid them in MR-imaging sequences. Part I: Fundamental and not so fundamental properties of spin echoes. *Concepts in Magnetic Resonance*, 3(3):125–143, 1991.

[17] P. Roschmann. Radiofrequency penetration and absorption in the human body: Limitations to high-field whole-body nuclear magnetic resonance imaging. *Medical Physics*, 14(6):922–931, 1987.

[18] J. M. Jin, J. Chen, W. C. Chew, H. Gan, R. L. Magin, and P. J. Dimbylow. Computation of electromagnetic fields for high-frequency magnetic resonance imaging applications. *Physics in Medicine and Biology*, 41(12), December 1996.

[19] Haiying Liu, Edward Michel, Sean O. Casey, and Charles L. Truwit. Actual imaging slice profile of 2d MRI. In L.E. Antonuk and M.J. Yaffe, editors, *Medical Imaging 2002: Physics of Medical Imaging*, volume 4682 of *Proceedings of the SPIE*, pages 767–773, May 2002.

[20] J. Pauly, P. Le Roux, Dwight Nishimura, and A. Macovski. Parameter relations for the Shinnar-Le Roux selective excitation pulse design algorithm [NMR imaging]. *IEEE Transactions on Medical Imaging*, 10(1):53–65, 1991.

[21] J Hennig. Multiecho Imaging Sequence with Low Refocusing Flip Angles. *J. Magn. Reson.*, 78:397, 1988.

[22] Matthias Weigel. Extended phase graphs: Dephasing, RF pulses, and echoes - pure and simple. *Journal of Magnetic Resonance Imaging*, 41(2):266–295, February 2015.

[23] Rudolf Stollberger and Paul Wach. Imaging of the active B1 field in vivo. *Magnetic Resonance in Medicine*, 35(2):246–251, 1996.

[24] Mustapha Bouhrara and Jean-Marie Bonny. B1 mapping with selective pulses. *Magnetic Resonance in Medicine*, 68(5):1472–1480, November 2012.

[25] Clifford R Jack, Jr, Matt A Bernstein, Nick C Fox, Paul Thompson, Gene Alexander, Danielle Harvey, Bret Borowski, Paula J Britson, Jennifer L Whitwell, Chadwick Ward, Anders M Dale, Joel P Felmlee, Jeffrey L Gunter, Derek L G Hill, Ron Killiany, Norbert Schuff, Sabrina Fox-Bosetti, Chen Lin, Colin Studholme, Charles S DeCarli, Gunnar Krueger, Heidi A Ward, Gregory J Metzger, Katherine T Scott, Richard Mallozzi, Daniel Blezek, Joshua Levy, Josef P Debbins, Adam S Fleisher, Marilyn Albert, Robert Green, George Bartzokis, Gary Glover, John Mugler, and Michael W Weiner. The Alzheimer's Disease Neuroimaging Initiative (ADNI): MRI methods. *Journal of magnetic resonance imaging: JMRI*, 27(4):685–691, April 2008.

[26] Nikolaus Weiskopf, John Suckling, Guy Williams, Marta M. Correia, Becky Inkster, Roger Tait, Cinly Ooi, Edward T. Bullmore, and Antoine Lutti. Quantitative multi-parameter mapping of R1, PD*, MT, and R2* at 3t: a multi-center validation. *Frontiers in Neuroscience*, 7, June 2013.

[27] Rajesh Kumar, Sean Delshad, Paul M. Macey, Mary A. Woo, and Ronald M. Harper. Development of T2-relaxation Values in Regional Brain Sites during Adolescence. *Magnetic resonance imaging*, 29(2):185–193, February 2011. 00013.

[28] Sean C. L. Deoni, Evelyne Mercure, Anna Blasi, David Gasston, Alex Thomson, Mark Johnson, Steven C. R. Williams, and Declan G. M. Murphy. Mapping Infant Brain Myelination with Magnetic Resonance Imaging. *Journal of Neuroscience*, 31(2):784–791, January 2011.

[29] H. B. W. Larsson, J. Frederiksen, J. Petersen, A. Nordenbo, I. Zeeberg, O. Henriksen, and J. Olesen. Assessment of demyelination, edema, and gliosis by in vivo determination of T1 and T2 in the brain of patients with acute attack of multiple sclerosis. *Magnetic Resonance in Medicine*, 11(3):337–348, September 1989.

[30] R. Marc Lebel, Amir Eissa, Peter Seres, Gregg Blevins, and Alan H. Wilman. Quantitative high-field imaging of sub-cortical gray matter in multiple sclerosis. *Multiple Sclerosis Journal*, 18(4):433–441, April 2012.

[31] Md. Nasir Uddin, Kelly C. McPhee, Gregg Blevins, and Alan H. Wilman. Recovery of accurate T2 from historical 1.5 tesla proton density and T2-weighted images: Application to 7-year T2 changes in multiple sclerosis brain. *Magnetic Resonance Imaging*, 37:21–26, April 2017.

[32] Francesco Manfredonia, Olga Ciccarelli, Zhaleh Khaleeli, Daniel J. Tozer, Jaume Sastre-Garriga, David H. Miller, and Alan J. Thompson. Normal-appearing brain t1 relaxation time predicts disability in early primary progressive multiple sclerosis. *Archives of Neurology*, 64(3):411–415, March 2007.

[33] A.L. MacKay, I.M. Vavasour, A. Rauscher, S.H. Kolind, B. M adler, G.R.W. Moore, A.L. Traboulsee, D.K.B. Li, and C. Laule. MR Relaxation in Multiple Sclerosis. *Neuroimaging Clinics of North America*, 19(1):1–26, February 2009.

[34] Timo Kurki and Markku Komu. Spin-lattice relaxation and magnetization transfer in intracranial tumors in vivo: Effects of Gd-DTPA on relaxation parameters. *Magnetic Resonance Imaging*, 13(3):379–385, January 1995.

[35] Kelsey Herrmann, Bernadette O. Erokwu, Mette L. Johansen, James P. Basilion, Vikas Gulani, Mark A. Griswold, Chris A. Flask, and Susann M. Brady-Kalnay.

Dynamic Quantitative T1 Mapping in Orthotopic Brain Tumor Xenografts. *Translational Oncology*, 9(2):147–154, April 2016.

[36] R. J. Dolan, A. M. Poynton, P. K. Bridges, and M. R. Trimble. Altered magnetic resonance white-matter T1 values in patients with affective disorder. *The British Journal of Psychiatry*, 157(1):107–110, July 1990.

[37] G. Bartzokis, D. Sultzer, J. Cummings, L. E. Holt, D. B. Hance, V. W. Henderson, and J. Mintz. In vivo evaluation of brain iron in Alzheimer disease using magnetic resonance imaging. *Archives of General Psychiatry*, 57(1):47–53, January 2000.

[38] D. Wagnerová, V. Herynek, M. Dezortová, P. Marusič, P. Krek, J. Zámečník, F. Jírøu, A. Škoch, and M. Hájek. The relationships between quantitative MR parameters in hippocampus in healthy subjects and patients with temporal lobe epilepsy. *Physiological Research*, 64(3):407–417, 2015.

[39] G. D. Jackson, A. Connelly, J. S. Duncan, R. A. Gr unewald, and D. G. Gadian. Detection of hippocampal pathology in intractable partial epilepsy: increased sensitivity with quantitative magnetic resonance T2 relaxometry. *Neurology*, 43(9):1793–1799, September 1993.

[40] Stephanie Lescher, Alina Jurcoane, Andreas Veit, Oliver B ahr, Ralf Deichmann, and Elke Hattingen. Quantitative T1 and T2 mapping in recurrent glioblastomas under bevacizumab: earlier detection of tumor progression compared to conventional MRI. *Neuroradiology*, 57(1):11–20, January 2015.

[41] A. MacKay, C. Laule, I. Vavasour, B. M adler, A. Traboulsee, D. Paty, W. Moore, and D. Li. The Short T2 Component in Normal-Appearing White Matter in Multiple Sclerosis. In *Normal-appearing White and Grey Matter Damage in Multiple Sclerosis*, Topics in Neuroscience, pages 47–61. Springer, Milano, 2004. DOI: 10.1007/978-88-470-2127-3_5.

[42] Andrew J. Walsh, R. Marc Lebel, Amir Eissa, Gregg Blevins, Ingrid Catz, Jian-Qiang Lu, Lothar Resch, Edward S. Johnson, Derek J. Emery, Kenneth G. Warren,

and Alan H. Wilman. Multiple Sclerosis: Validation of MR Imaging for Quantification and Detection of Iron. *Radiology*, 267(2):531–542, May 2013.

[43] B. Hallgren and P. Sourander. The effect of age on non–haemin iron in the human brain. *Journal of Neurochemistry*, 3(1):41–51, 1958.

[44] George Bartzokis, Mace Beckson, Darwood B. Hance, Peter Marx, Jennifer A. Foster, and Stephen R. Marder. MR evaluation of age-related increase of brain iron in young adult and older normal males. *Magnetic Resonance Imaging*, 15(1):29–35, January 1997.

[45] Josef Vymazal, Rodney A. Brooks, Charles Baumgarner, Vu Tran, David Katz, Jeff W. M. Bulte, E. Rivka Bauminger, and Giovanni Di Chiro. The relation between brain iron and NMR relaxation times: An in vitro study. *Magnetic Resonance in Medicine*, 35(1):56–61, 1996.

[46] Neil Gelman, Jay M. Gorell, Peter B. Barker, Ralph M. Savage, Eric M. Spickler, Joseph P. Windham, and Robert A. Knight. MR Imaging of Human Brain at 3.0 T: Preliminary Report on Transverse Relaxation Rates and Relation to Estimated Iron Content. *Radiology*, 210(3):759–767, March 1999.

[47] Md Nasir Uddin, R. Marc Lebel, Peter Seres, Gregg Blevins, and Alan H. Wilman. Spin echo transverse relaxation and atrophy in multiple sclerosis deep gray matter: A two-year longitudinal study. *Multiple Sclerosis (Houndmills, Basingstoke, England)*, 22(9):1133–1143, August 2016.

[48] Timothy J. Mosher, Yi Liu, and Collin M. Torok. Functional Cartilage MRI T2 Mapping: Evaluating the Effect of Age and Training on Knee Cartilage Response to Running. *Osteoarthritis and cartilage / OARS, Osteoarthritis Research Society*, 18(3):358–364, March 2010. 00060.

[49] Shoichiro Takao, Tan B. Nguyen, Hon J. Yu, Shigeo Hagiwara, Yasuhito Kaneko, Taiki Nozaki, Seiji Iwamoto, Maki Otomo, Ran Schwarzkopf, and Hiroshi Yoshioka.

T1rho and T2 relaxation times of the normal adult knee meniscus at 3t: analysis of zonal differences. *BMC Musculoskeletal Disorders*, 18, May 2017.

[50] L Yao, A Gentili, and A Thomas. Incidental magnetization transfer contrast in fast spin-echo imaging of cartilage. *Journal of magnetic resonance imaging: JMRI*, 6(1):180–184, February 1996.

[51] S. T. Soellner, A. Goldmann, D. Muelheims, G. H. Welsch, and M. L. Pachowsky. Intraoperative validation of quantitative T2 mapping in patients with articular cartilage lesions of the knee. *Osteoarthritis and Cartilage*, 25(11):1841–1849, November 2017.

[52] Ishu Arpan, Sean C. Forbes, Donovan J. Lott, Claudia R. Senesac, Michael J. Daniels, William T. Triplett, Jasjit K. Deol, H. Lee Sweeney, Glenn A. Walter, and Krista Vandenborne. T2 mapping provides multiple approaches for the characterization of muscle involvement in neuromuscular diseases: a cross-sectional study of lower leg muscles in 515-year-old boys with Duchenne muscular dystrophy. *NMR in Biomedicine*, 26(3):320–328, March 2013.

[53] Hermien E. Kan, Tom W. J. Scheenen, Marielle Wohlgemuth, Dennis W. J. Klomp, Ivonne van Loosbroek-Wagenmans, George W. Padberg, and Arend Heerschap. Quantitative MR imaging of individual muscle involvement in facioscapulohumeral muscular dystrophy. *Neuromuscular Disorders*, 19(5):357–362, May 2009.

[54] Daniel Kim, Jens H. Jensen, Ed X. Wu, Sujit S. Sheth, and Gary M. Brittenham. Breathhold multiecho fast spin-echo pulse sequence for accurate R2 measurement in the heart and liver. *Magnetic Resonance in Medicine*, 62(2):300–306, August 2009.

[55] Haiying Tang, Jens H. Jensen, Christina L. Sammet, Sujit Sheth, Srirama V. Swaminathan, Kristi Hultman, Daniel Kim, Ed X. Wu, Truman R. Brown, and Gary M. Brittenham. MR characterization of hepatic storage iron in transfusional iron overload. *Journal of Magnetic Resonance Imaging*, 39(2):307–316, February 2014.

[56] Diego Hernando, Yakir S Levin, Claude B Sirlin, and Scott B Reeder. Quantification of Liver Iron with MRI: State of the Art and Remaining Challenges. *Journal of magnetic resonance imaging : JMRI*, 40(5):1003–1021, November 2014.

[57] Bettina Baeßler, Frank Schaarschmidt, Christian Stehning, Bernhard Schnackenburg, Agathe Giolda, David Maintz, and Alexander C. Bunck. Reproducibility of three different cardiac T2-mapping sequences at 1.5t. *Journal of Magnetic Resonance Imaging*, 44(5):1168–1178, November 2016.

[58] Nilesh R. Ghugre, Cathleen M. Enriquez, Ignacio Gonzalez, Marvin D. Nelson, Thomas D. Coates, and John C. Wood. MRI detects myocardial iron in the human heart. *Magnetic Resonance in Medicine*, 56(3):681–686, September 2006.

[59] Enver Tahir, Martin Sinn, Sebastian Bohnen, Maxim Avanesov, Dennis S aring, Christian Stehning, Bernhard Schnackenburg, Christine Eulenburg, Joshua Wien, Ulf K. Radunski, Stefan Blankenberg, Gerhard Adam, Charles B. Higgins, Maythem Saeed, Kai Muellerleile, and Gunnar K. Lund. Acute versus Chronic Myocardial Infarction: Diagnostic Accuracy of Quantitative Native T1 and T2 Mapping versus Assessment of Edema on Standard T2-weighted Cardiovascular MR Images for Differentiation. *Radiology*, 285(1):83–91, October 2017.

[60] J.T. Vaughan, M. Garwood, C.m. Collins, W. Liu, L. DelaBarre, G. Adriany, P. Andersen, H. Merkle, R. Goebel, M.b. Smith, and K. Ugurbil. 7t vs. 4t: RF power, homogeneity, and signal-to-noise comparison in head images. *Magnetic Resonance in Medicine*, 46(1):24–30, July 2001.

[61] A. P. Crawley and R. M. Henkelman. Errors in T2 estimation using multislice multiple-echo imaging. *Magnetic Resonance in Medicine*, 4(1):34–47, January 1987.

[62] S. Majumdar, S. C. Orphanoudakis, A. Gmitro, M. O'Donnell, and J. C. Gore. Errors in the measurements of T2 using multiple-echo MRI techniques. II. Effects of static field inhomogeneity. *Magnetic Resonance in Medicine: Official Journal of the Society of Magnetic Resonance in Medicine / Society of Magnetic Resonance in Medicine*, 3(4):562–574, August 1986.

[63] Md. Nasir Uddin, R. Marc Lebel, and Alan H. Wilman. Transverse relaxometry with reduced echo train lengths via stimulated echo compensation. *Magnetic Resonance in Medicine*, 70(5):1340–1346, 2013.

[64] Noam Ben-Eliezer, Daniel K. Sodickson, and Kai Tobias Block. Rapid and accurate T $_2$ mapping from multi-spin-echo data using Bloch-simulation-based reconstruction: Mapping Using Bloch-Simulation-Based Reconstruction. *Magnetic Resonance in Medicine*, 73(2):809–817, 2015.

[65] Thomas Prasloski, Burkhard M adler, Qing-San Xiang, Alex MacKay, and Craig Jones. Applications of stimulated echo correction to multicomponent T2 analysis. *Magnetic Resonance in Medicine*, 67(6):1803–1814, 2012.

[66] W. D. Rooney, J. R. Poolaro, S. C. Forbes, D. J. Wang, K Vanderborne, and G. A. Walter. Application of the Extended Phase Graph Technique to Improve T2 Quantitation Across Sites. In *Proceedings of International Society for Magnetic Resonance in Medicine Annual Meeting 19*, volume 19, page 138, 2011.

[67] Chuan Huang, Ali Bilgin, Tomoe Barr, and Maria I. Altbach. T2 relaxometry with indirect echo compensation from highly undersampled data. *Magnetic Resonance in Medicine*, 70(4):1026–1037, 2013.

[68] Chuan Huang, Maria I. Altbach, and Georges El Fakhri. Pattern recognition for rapid T2 mapping with stimulated echo compensation. *Magnetic Resonance Imaging*, 32(7):969–974, September 2014.

[69] Mehdi Behroozi, Caroline Chwiesko, Felix Str ockens, Magdalena Sauvage, Xavier Helluy, Jutta Peterburs, and Onur G unt urk un. In vivo measurement of T1 and T2 relaxation times in awake pigeon and rat brains at 7t. *Magnetic Resonance in Medicine*, page In Press, May 2017.

[70] Christian Langkammer, Nikolaus Krebs, Walter Goessler, Eva Scheurer, Franz Ebner, Kathrin Yen, Franz Fazekas, and Stefan Ropele. Quantitative MR Imag-

ing of Brain Iron: A Postmortem Validation Study. *Radiology*, 257(2):455–462, November 2010. 00088.

[71] Serguei Liachenko and Jaivijay Ramu. Quantification and reproducibility assessment of the regional brain T2 relaxation in nave rats at 7t. *Journal of Magnetic Resonance Imaging*, 45(3):700–709, March 2017.

[72] Luca Biasiolli, Alistair C Lindsay, Joshua T Chai, Robin P Choudhury, and Matthew D Robson. In-vivo quantitative T2 mapping of carotid arteries in atherosclerotic patients: segmentation and T2 measurement of plaque components. *Journal of Cardiovascular Magnetic Resonance*, 15(1):69, August 2013.

[73] Marion de Roquefeuil, Pierre-André Vuissoz, Jean-Marie Escanyé, and Jacques Felblinger. Effect of physiological Heart Rate variability on quantitative T2 measurement with ECG-gated Fast Spin Echo (FSE) sequence and its retrospective correction. *Magnetic Resonance Imaging*, 31(9):1559–1566, November 2013.

[74] Vít Herynek, Dita Wagnerová, Irena Hejlová, Monika Dezortov, and Milan Hájek. Changes in the brain during long-term follow-up after liver transplantation. *Journal of Magnetic Resonance Imaging*, 35(6):1332–1337, June 2012.

[75] Michael J. Knight, Bryony McCann, Demitra Tsivos, Elizabeth Couthard, and Risto A. Kauppinen. Quantitative T1 and T2 MRI signal characteristics in the human brain: different patterns of MR contrasts in normal ageing. *Magnetic Resonance Materials in Physics, Biology and Medicine*, 29(6):833–842, December 2016.

[76] Tarja L onnfors-Weitzel, Thilo Weitzel, Johannes Slotboom, Claus Kiefer, Claudio Pollo, Michael Sch upbach, Markus Oertel, Alain Kaelin, and Roland Wiest. T2-relaxometry predicts outcome of DBS in idiopathic Parkinson's disease. *NeuroImage : Clinical*, 12:832–837, September 2016. 00000.

[77] Takashi Nishii, Toshiyuki Shiomi, Hisashi Tanaka, Youichi Yamazaki, Kenya Murase, and Nobuhiko Sugano. Loaded Cartilage T2 Mapping in Patients with Hip Dysplasia. *Radiology*, 256(3):955–965, September 2010.

[78] J. Sedlacik, K. Boelmans, U. L obel, B. Holst, S. Siemonsen, and J. Fiehler. Reversible, irreversible and effective transverse relaxation rates in normal aging brain at 3 T. *NeuroImage*, 84:1032–1041, January 2014.

[79] Tilman J. Sumpf, Martin Uecker, Susann Boretius, and Jens Frahm. Model-based nonlinear inverse reconstruction for T2 mapping using highly undersampled spin-echo MRI. *Journal of Magnetic Resonance Imaging*, 34(2):420–428, August 2011. 00057.

[80] N. K. Focke, G. Helms, P. M. Pantel, S. Scheewe, M. Knauth, C. G. Bachmann, J. Ebentheuer, P. Dechent, W. Paulus, and C. Trenkwalder. Differentiation of Typical and Atypical Parkinson Syndromes by Quantitative MR Imaging. *American Journal of Neuroradiology*, 32(11):2087–2092, December 2011.

[81] Corinna M Bauer, Hernan Jara, and Ron Killiany. Whole brain quantitative T2 MRI across multiple scanners with dual echo FSE: Applications to AD, MCI, and normal aging. *NeuroImage*, 52(2):508–514, August 2010.

[82] Amanda F. Mejia, Elizabeth M. Sweeney, Blake Dewey, Govind Nair, Pascal Sati, Colin Shea, Daniel S. Reich, and Russell T. Shinohara. Statistical estimation of T1 relaxation times using conventional magnetic resonance imaging. *NeuroImage*, 133:176–188, June 2016.

[83] Peter Gibbs, Daniel J. Tozer, Gary P. Liney, and Lindsay W. Turnbull. Comparison of quantitative T2 mapping and diffusion-weighted imaging in the normal and pathologic prostate. *Magnetic Resonance in Medicine*, 46(6):1054–1058, 2001.

[84] Gary P. Liney, Adrian J. Knowles, David J. Manton, Lindsay W. Turnbull, Stephen J. Blackband, and Anthony Horsman. Comparison of conventional single echo and multi-echo sequences with a fast spin-echo sequence for quantitative T2 mapping: Application to the prostate. *Journal of Magnetic Resonance Imaging*, 6(4):603–607, 1996.

[85] Khader M. Hasan, Christopher Halphen, Arash Kamali, Flavia M. Nelson, Jerry S. Wolinsky, and Ponnada A. Narayana. Caudate Nuclei Volume, Diffusion Tensor Metrics, and T2 Relaxation in Healthy Adults and Relapsing-Remitting Multiple Sclerosis Patients: Implications to Understanding Gray Matter Degeneration. *Journal of magnetic resonance imaging : JMRI*, 29(1):70–77, January 2009.

[86] Khader M. Hasan, Indika S. Walimuni, Larry A. Kramer, and Richard E. Frye. Human brain atlas-based volumetry and relaxometry: Application to healthy development and natural aging. *Magnetic Resonance in Medicine*, 64(5):1382–1389, 2010.

[87] Sonja Bauer, Marlies Wagner, Alexander Seiler, Elke Hattingen, Ralf Deichmann, Ulrike Nöth, and Oliver C. Singer. Quantitative T2-Mapping in Acute Ischemic. *Stroke*, 45(11):3280–3286, November 2014.

[88] Jody L. Tanabe, Martina Vermathen, Robert Miller, Deborah Gelinas, Michael W. Weiner, and William D. Rooney. Reduced MTR in the corticospinal tract and normal T2 IN amyotrophic lateral sclerosis. *Magnetic resonance imaging*, 16(10):1163–1169, December 1998.

[89] Lili He and Nehal A. Parikh. Automated detection of white matter signal abnormality using T2 relaxometry: application to brain segmentation on term MRI in very preterm infants. *NeuroImage*, 64:328–340, January 2013.

[90] Sean C.L. Deoni, Brian K. Rutt, and Terry M. Peters. Rapid combined T1 and T2 mapping using gradient recalled acquisition in the steady state. *Magnetic Resonance in Medicine*, 49(3):515–526, March 2003. 00316.

[91] Sean C. L. Deoni, Terry M. Peters, and Brian K. Rutt. High-resolution T1 and T2 mapping of the brain in a clinically acceptable time with DESPOT1 and DESPOT2. *Magnetic Resonance in Medicine*, 53(1):237–241, January 2005. 00148.

[92] J.b.m. Warntjes, O. Dahlqvist, and P. Lundberg. Novel method for rapid, simulta-

neous T1, T*2, and proton density quantification. *Magnetic Resonance in Medicine*, 57(3):528–537, March 2007.

[93] J.B.M. Warntjes, O. Dahlqvist Leinhard, J. West, and P. Lundberg. Rapid magnetic resonance quantification on the brain: Optimization for clinical usage. *Magnetic Resonance in Medicine*, 60(2):320–329, August 2008.

[94] Dan Ma, Vikas Gulani, Nicole Seiberlich, Kecheng Liu, Jeffrey L. Sunshine, Jeffrey L. Duerk, and Mark A. Griswold. Magnetic resonance fingerprinting. *Nature*, 495(7440):187–192, March 2013.

[95] European Society of Radiology. Magnetic Resonance Fingerprinting - a promising new approach to obtain standardized imaging biomarkers from MRI. *Insights into Imaging*, 6(2):163–165, April 2015.

[96] White Matter Study Group. White Matter Study Group Meeting. In *Proceedings of ISMRM*, volume 25, April 2017.

[97] Ilana R. Leppert, C. Robert Almli, Robert C. McKinstry, Robert V. Mulkern, Carlo Pierpaoli, Michael J. Rivkin, and G.Bruce Pike. T2 Relaxometry of Normal Pediatric Brain Development. *Journal of magnetic resonance imaging : JMRI*, 29(2):258–267, February 2009.

[98] Joseph R. Roebuck, Steven J. Haker, Dimitris Mitsouras, Frank J. Rybicki, Clare M. Tempany, and Robert V. Mulkern. Carr-Purcell-Meiboom-Gill imaging of prostate cancer: quantitative T2 values for cancer discrimination. *Magnetic Resonance Imaging*, 27(4):497–502, May 2009.

Chapter 2

Transverse Relaxation and Flip Angle Mapping: Evaluation of Simultaneous and Independent Methods using Multiple Spin Echoes[1]

Purpose: To evaluate transverse relaxation (T2) and flip angle maps derived from signal pathway modelling of multiple spin echoes using simultaneous or independent T2 and flip angle fitting.

Methods: We examined different approaches to indirect and stimulated echo compensated T2 relaxometry from multiple spin echoes to evaluate both T2 and flip angle accuracy in simulation, phantom, and human brain. Signal pathways were modelled with or without independent flip angle maps using either Bloch simulations, or Extended Phase Graph (EPG) with Fourier or Shinnar-Le Roux approximation of slice profiles.

Results: Slice-selective decay curves differ substantially between models. Inaccurate flip angles are obtained with EPG methods, although T2 values are relatively accurate. Providing measured flip angles to EPG methods yields erroneous T2. Bloch methods improve both T2 and flip angle results. Simultaneous fitting can suffer from flip angle redundancy yielding multiple T2 solutions, particularly in low SNR cases.

Conclusion: EPG fitting provides reasonably accurate T2, but is limited by poor accuracy in resulting flip angles, and T2 errors increase when flip angles are provided. Bloch simultaneous fitting of T2 and flip angle provides excellent results, but can be limited by multiple solutions which can be overcome by including a flip angle map.

2.1 Introduction

Quantification of the transverse relaxation time (T2), rather than just T2-weighting, has many applications including investigation of liver [1, 2], heart [3, 4], brain [5–11], muscle [12, 13] and cartilage[14–16]. However, T2 quantification from multiple spin echoes is rarely straightforward due to imperfect refocusing pulses which produce stimulated and indirect echoes that lead to non-exponential decay [17, 18]. Imperfect refocusing can arise from B1 inhomogeneity [19], non-ideal slice profiles or purposeful use of reduced flip angles.

Recent works have determined T2 by modelling the actual spin response from multi-echo spin echo experiments [18, 20]. Two different models were used: either the Extended Phase Graph (EPG) with Fourier slice approximations [18], or Bloch simulations [20]. These methods simulate the spin echo pathways with different models, but aim to achieve the same goal of determining both the T2 and the refocusing flip angles from the fitting process. However, the accuracy of the inherent flip angle map produced by these methods has not been studied in any detail. Furthermore, differences in T2 results between the two fitting models have not been studied. Neither has the value of a hybrid model using EPG with Shinnar-Le Roux (SLR) slice profiles been previously considered. In addition, the

benefits and limitations of fitting for both T2 and flip angle simultaneously have not been compared to a similar method where the flip angle is provided a priori [21]. To fill this knowledge gap, the purpose of this paper is threefold: evaluation of the accuracy of the flip angle map when performing simultaneous T2 and flip angle fitting, comparison of T2 fitting with Bloch or EPG approaches, and comparison to T2 fitting with independent flip angle mapping. These comparisons are made in simulation, phantom and human brain, with the results clarifying differences between methods and providing guidelines for the use of these various multiple spin echo methods for single component T2 fitting.

2.2 Methods

2.2.1 Overview

Multi-echo spin echo (MESE) signal decay was modelled with either Bloch [20, 21] or EPG simulations [18] to determine T2, signal amplitude and, where necessary, flip angle. These methods all provide both indirect and stimulated echo compensation (ISEC); however, each method treats the RF pulses in a different manner. Signal pathways were modelled with or without independent flip angle maps using either Bloch simulations, or EPG with Fourier or SLR approximation of slice profiles. These six ISEC methods, as well as a simple exponential fit, are compared in simulation, phantom and the human brain. Simulations are used to determine accuracy of a range of T2 and flip angle fits at SNR of 50, and for a range of SNR values. Errors in fitting due to the assumption of a constant T1 of 2 s was assessed for a range of T1, T2, and flip angle values.

2.2.2 Bloch-ISEC Fitting

Bloch equation based simulations have been previously described for simultaneous T2 and flip angle fitting [20] and for independent T2 fitting with a provided flip angle map [21]. Here, we build on our previously described Bloch simulation based ISEC method which used only two data points from a proton density and a T2-weighted image [21], and extend it to an entire MESE decay train to perform either a two parameter fit (T2 and

amplitude, where a flip angle map is provided to the algorithm) or a three parameter fit (T2, amplitude, and flip angle). MESE data were fitted via minimization of the sum squared difference between experimental decay curves and simulated data, using a pattern recognition algorithm [20, 22].

A dictionary of decay curves with many T2 and flip angle values was first created. Simulations of slice-selective MESE T2 decay curves were performed using fully simulated RF pulses [23], and solutions to the Bloch equations to simulate relaxation. All simulations were performed using in-house MATLAB (R2014a, 64 bit) code. RF pulses were modelled with the SLR algorithm [23]. In order to model slice selection, typically 1001 points equally spaced over twice the excitation width in the slice-select direction were modelled independently, and summed together. The SLR Algorithm is based on a discrete approximation to the spin domain version of the Bloch equation [23]. It takes advantage of the fact that Bloch equations reduce to a rotation if relaxation effects are neglected during the RF pulse. This rotation can be represented by a 2 2 unitary matrix, which may be further simplified to a pair of polynomials. Shaped pulses are broken into a sequence of n hard pulse segments (here, n = 1024). The total magnetization response may be calculated by the concatenation of n rotation matrices, which can be described as two n-1 order polynomials. The SLR algorithm is described in sufficient detail for implementation in reference (23). Alternatively, various implementations of Bloch simulations, have been published online (for example, [24]). In order to model slice selection, magnetization response to RF pulses, gradients, and relaxation must be calculated at many points across the slice-select direction (here, typically 1001 points equally spaced over twice the excitation width). Relaxation decay between RF pulses was calculated according to solutions to Bloch equations. Echo amplitudes are calculated by summing these points together at each echo time.

To create the dictionary of 510711 curves for T2 fitting, simulations were repeated for a range of T2 (10 - 1000 ms at 0.1 ms resolution up to 150 ms, 1 ms resolution from 150 - 200 ms, 2 ms resolution from 200 - 300 ms, 5 ms resolution from 300 - 500 ms, and 10 ms resolution from 500 - 1000 ms) and normalized flip angles, nB1, (0.20 - 1.80 at 0.005 resolution), and an assumed T1 of 2 s (this assumption is examined here).

2.2.3 EPG-ISEC Fitting

T2 fitting utilizing slice resolved EPG-ISEC has been previously described [18], and MAT-LAB code for that algorithm is freely available [25]. The extended phase graph model [17] provides a system of equations which describe spin amplitudes following radiofrequency pulses of a given angle. The EPG model does not include slice selection, so Lebel and Wilman [18] approximated the effect of slice selection by providing pre-computed flip angle distributions, estimated by the Fourier transform of RF pulse shapes. EPG was then used to calculate the resulting echo train amplitude at many locations across the slice, given the excitation and refocusing flip angles for each location in the slice. Note that in this algorithm, flip angle distributions are calculated once, using the prescribed angles. Within the fitting algorithm, the flip angle distribution is scaled according to the flip angle map fit. Relaxation decay between RF pulses was calculated according to solutions to Bloch equations. Echo amplitudes were calculated by summing magnetization across the profile.

Additionally, modifications to the original EPG-ISEC method [18] were tested. In addition to using the Fourier Transform (FT) approximation, as originally used in [18], we tested use of slice profile flip angle distributions calculated using the SLR algorithm. We refer to these methods as EPG_{SLR} and EPG_{FT}, to clarify the slice profile approximation used. The EPG-ISEC method was also modified to accept the option of an independently-measured flip angle, reducing it to a two parameter fit: T2 and amplitude. In each implementation, the signal was summed over 201 points equally distributed across 2 $\times$ slice width, and T1 was assumed to be 2 s within the fitting model. Note that in this algorithm, flip angle distributions are calculated once, using the prescribed angles. Within the fitting algorithm, the flip angle distribution is scaled according to the flip angle map fit.

The inferiority of the exponential approach has been previously demonstrated for EPG [18] and Bloch approaches [20, 21]. More specifically, the EPG-ISEC method has previously been shown to be superior to the exponential approach under a wide range of conditions that consider T1/T2 ratio, flip angle dependence, and SNR [18]. Thus we

do not extensively consider exponential fitting, although mono-exponential fitting results are included in all tables.

2.2.4   Flip Angle Mapping

Pairs of Fast Spin Echo (FSE) images with variable excitation angle were collected to enable flip angle computation using a double angle method [26] with slice profile correction, as previously described [21]. Correction for the slice profile is necessary to avoid systematic errors [27]. Here, flip angle maps are expressed as a normalized value (nB1), which is a correction factor relating the prescribed flip angle, to the actual flip angle achieved at the center of the slice.

2.2.5   Numerical Assessment of T2 Fitting Methods

We compared each fitting model in terms of model accuracy, robustness to noise, and impact of providing prior flip angle maps to reduce fitting parameters. Simulated T2 decay curves with a range of T2 (20 - 200 ms) and nB1 (0.5 - 1.5), and with T1 1 s were fitted with each fitting method (pulse shapes, gradients, and timing were matched to experimental parameters, as described below). The ISEC T2 fitting algorithms tested were EPG_{FT}, EPG_{SLR} and Bloch with all methods tested both with and without a provided flip angle map. Errors in T2 fit were computed in order to assess performance of each fitting routine. We also examine the assumption in EPG-ISEC of symmetry around 180° refocusing angles by comparing sample curves from each model for selective and non-selective RF pulses.

Simulations were used to examine the robustness of each T2 fitting model to noise. Bloch simulated noisy data was generated by adding random Gaussian complex noise to a set of decay curves with a range of T2 and nB1 (T2 = 20 - 100 ms, nB1 = 0.5 - 1.5, corresponding to refocusing angles 90° - 270°). SNR was defined as the ratio of the amplitude of the first echo to the standard deviation of the noise. An SNR of 50 was first applied. Each curve was then fit with each of the six ISEC fitting algorithms, and to an exponential model, for comparison. The process was repeated 500 times, and mean and

standard deviation of the resulting T2 and nB1 fits was examined. To further examine the robustness of fitting over a range of SNR (from 10 - 300), simulated T2 curves (T2 = 50 ms, nB1 = 1.0) were fitted with each method. The mean and standard deviation in resulting T2 fits from 500 repetitions at each SNR were examined

To examine the repercussions of assuming a uniform T1, decay curves were simulated with a range of T1s (200 - 3000 ms) and were fitted using each ISEC method, assuming T1 = 2 s, as was assumed for in vivo experiments. Errors were examined for a range of T2 (25 - 300 ms) and nB1 (0.33 - 1.5, corresponding to 60 - 270° refocusing angles).

2.2.6   Phantom Experiments

T2 fitting results from MESE experiments in phantoms were performed with comparison to exponential fitting of a single spin echo experiment, which uses only a single refocusing pulse, and thus exhibits no indirect or stimulated echoes. Four $MnCl_2$ solutions with concentrations ranging from 68-402 mM were placed in 28 mm diameter cylindrical plastic laboratory tubes. A series of single spin echo experiments were performed (TE = 13.1, 14, 20, 30, 50, 70, 100, 200, 400, 700 ms, TR 14 s, nominal excitation 90°; nominal refocusing 180°; sinc pulse shapes). T2 maps were computed by non-linear least squares fit of an exponential function to all echo times in each single echo spin echo data set. T1 values were estimated with an inversion recovery experiment (inversion times = 14, 20, 50, 100, 200, 300, 500, 1000, 2000, 3000 ms; FSE readout; 10 mm slice thickness; TR 12 s; TE 8.5 ms). MESE data, and a flip angle map were also acquired during the same scanning session, with parameters matched to in vivo experiments (described below), with the exception of 10 mm slice thickness for all experiments, and TR 14 s for flip angle mapping. T2 maps using the various ISEC fits and a simple mono-exponential model were computed from the MESE data and compared to single spin echo T2 fits. ISEC fits were performed using the measured T1 in each case. MESE fit results were compared to single echo spin echo T2 fit values and to double angle flip angle measurements using a two sample t-test, and threshold of p < 0.01 while accounting for multiple comparisons using a Bonferroni correction.

2.2.7 In Vivo Experiments

Axial single-slice two dimensional MESE images of the human brain were acquired in nine healthy volunteers (6 male, aged 29.1±5.1 years) through iron-rich deep grey matter. MESE sequence parameters included: TR 3 s, echo spacing 10 ms, echo train length 32, nominal excitation 90°; nominal refocusing 180°, excitation and refocusing pulse durations 4 ms and 1.6 ms, excitation width 4 mm, refocusing width 1.75 × excitation width, Gaussian pulse shapes (time-bandwidth product 2.69; 5 sigma width), matrix 256 × 145 × 1, voxel size $1 \times 1.25 \times 4$ mm^3. FSE images for flip angle mapping were acquired with resolution and pulse shapes matched to the MESE acquisition. All experiments were performed on a Varian Unity Inova 4.7 T whole-body imaging system.

Regions-of-interest (ROIs) were drawn selecting four grey matter regions (putamen, globus pallidus, head of the caudate nucleus, thalamus) and two white matter regions (frontal and posterior white matter). Mean ROI T2 values were reported, with bilateral ROIs combined.

2.3 Results

2.3.1 Simulations

Slice selective simulations of MESE sequences differ, depending on the model used. Figure 2.1 shows decay curves for three choices of refocusing angles (180° ±17°), using both non-selective (a) and slice selective simulations with Bloch (b) or EPG methods (c,d). While the EPG and Bloch simulations reduce to the same results in a non-selective application, they are not equivalent when slice selective pulses are simulated. Furthermore, symmetry around refocusing angles of 180° is only achieved in the non-selective case.

Accuracy of T2 and nB1 fitting was examined at an SNR of 50. Mean error in T2 fit (Fig. 2.2) and corresponding mean nB1 maps (Fig. 2.3) are shown. In regard to T2, EPG_{SLR} (Fig. 2.2c) provides improved accuracy in T2 over the original EPG_{FT} method (Fig. 2.2b), however the Bloch-based methods provide best accuracy (Fig. 2.2a,d). When provided with accurate flip angles, both EPG methods perform poorly (Fig. 2.2e,f),
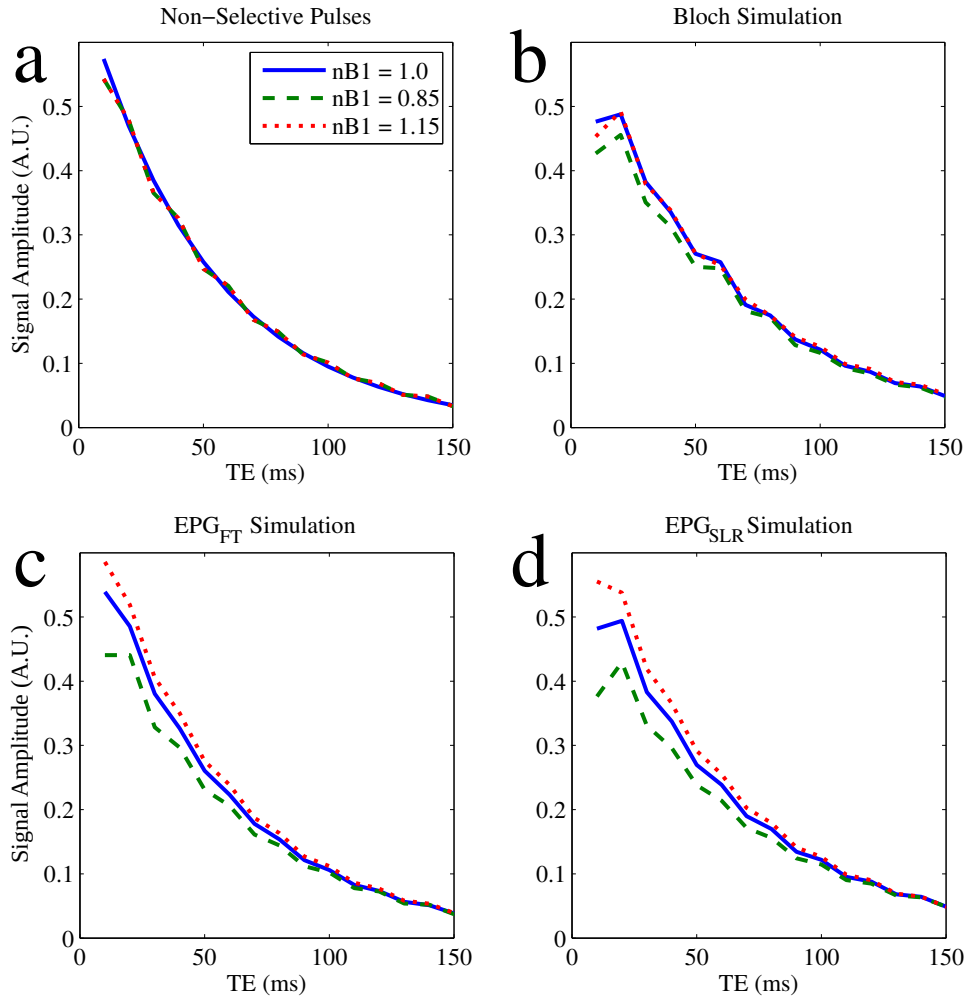
Figure 2.1: T2 decay curves with T2 = 50 ms and nB1 = 0.85, 1 and 1.15 were computed using the following simulations: (a) non-selective (b) slice selective Bloch, (c) EPG$_{FT}$, and (d) EPG$_{SLR}$. Except for the non-selective case, symmetry around 180° refocusing angles is not observed, and models do not provide equivalent results.

and significantly over or underestimate T2. In regard to flip angle accuracy, neither of the EPG fitting models provides an accurate nB1 map across the range of values, while simulations show the Bloch approach to be more effective (Fig. 2.3). Exponential fitting resulted in overestimation of T2 of 20-159% in the range of values tested (see Supplementary Figure A.1).

The coefficient of variation (COV) of T2 for the SNR of 50 case considered in Fig. 2.2 is shown in Fig. 2.4. Three parameter Bloch and EPG have similar levels of variation in fit results. Providing the flip angle to the Bloch fitting model, reduces the number of fitting parameters thus decreasing variation in re-sults. For lower SNR values, such
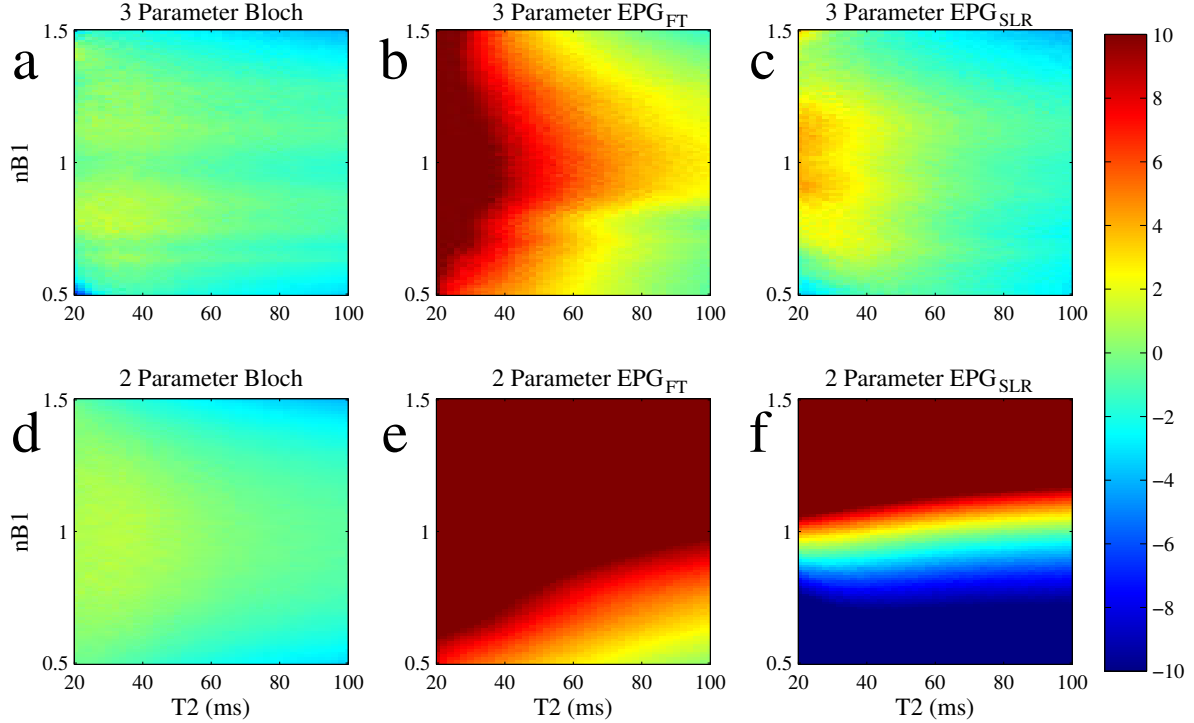
Figure 2.2: Mean error in T2 fit result (%) from simulated T2 decay curves with T1 =1 s, 500 repetitions at SNR = 50 for simultaneous T2 and nB1 fitting using (a) Bloch,(b) EPG$_{FT}$, (c) EPG$_{SLR}$. Bottom row (d-f) nB1 is provided to the fitting algorithm: (d) Bloch (e) EPG$_{FT}$, (f) EPG$_{SLR}$.

as SNR < 20, all methods performed poorly. Standard deviations rose sharply as SNR decreased below 30 (see Supplementary Figure A.2), and thus ROIs in in vivo data with SNR < 30 were not included in the reported values

T2 mapping using the Bloch model for ISEC was found to be robust to errors in the assumed T1, where T1 is estimated within 1 second (see Supplementary Figure A.3. The EPG$_{SLR}$ fitting model was similarly robust, however, the EPG$_{FT}$ model, overestimated T2. Fit accuracy in all models is relatively insensitive to T1, when fitting uses a T1 estimate (here, 2 s) within 1 s of the actual T1 (1 - 3 s).

Potential redundant solutions when fitting nB1 and T2 simultaneously are illustrated in Fig. 2.5 using the Bloch method. We compare a simulated data curve (T2 = 70 ms, nB1 = 0.80) with no added noise to similar curves in the fitting space (Fig. 2.5a). All sample curves shown would provide a fit with an R^2 of 0.99. A map of the sum of square of residuals for a range of possible fit parameters for a simulated zero noise curve
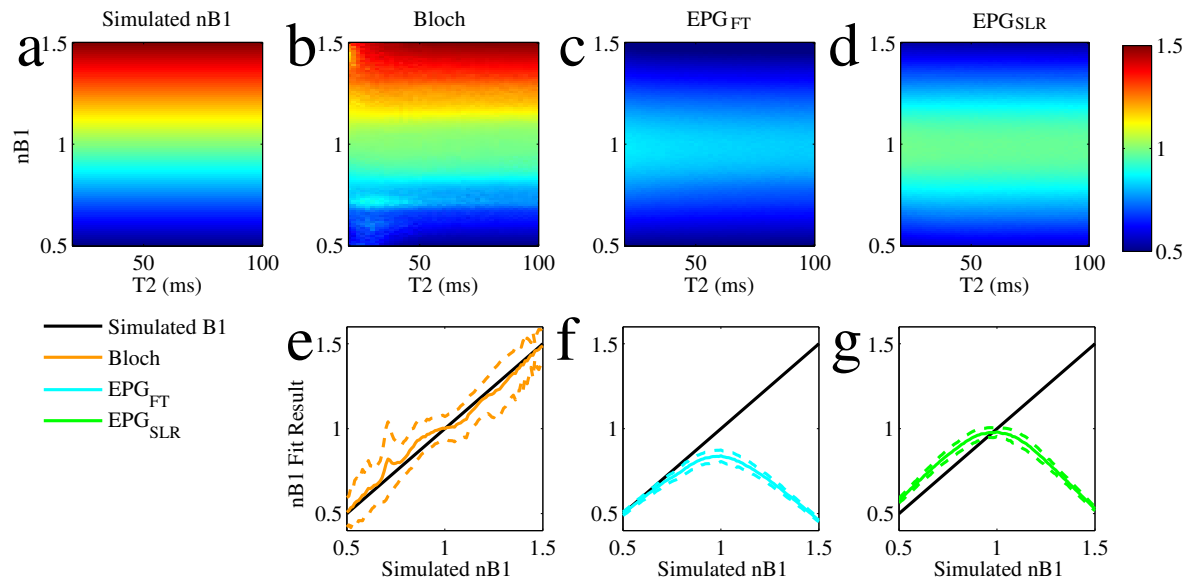
Figure 2.3: Mean nB1 results are shown in color from each fitting algorithm with actual nB1 on the y-axis. (a) Actual nB1 is compared to nB1 fit from three parameter (b) Bloch, (c) EPG$_{FT}$, and (d) EPG$_{SLR}$. Cross sections from b-d are examined in (e-g) for T2 = 50 ms, showing mean (solid line) $\pm$ 1 standard deviation (dashed line) in nB1 fit results, relative to the simulated nB1 value (black).
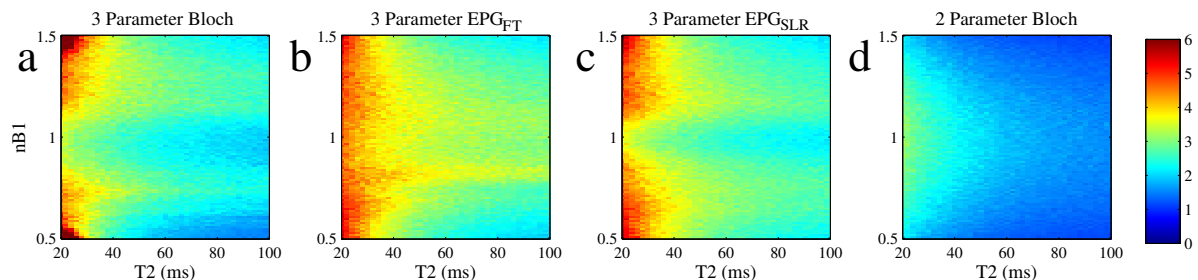
Figure 2.4: Coefficient of variation in T2 fit result (%) from 500 repetitions at SNR = 50 for simultaneous T2 and nB1 fitting using three parameter (a) Bloch-ISEC,(b) EPG$_{FT}$ model, (c) EPG$_{SLR}$ fit , or (d) two parameter Bloch-ISEC.

is shown in 5b. If nB1 was known, the range of potential T2 fits is reduced to a vertical intersection in 5b. The minimum point is evident in this zero noise simulation, however, a local minimum may also be found with nB1 > 1. Further, the sum squared residuals at the shown alternative solutions are comparable to values that would be expected for an accurate fit of a data curve with SNR between 80 and 100. As SNR decreases, the ability of the fitting algorithm to reliably converge on the correct T2 and nB1 fit is hindered, as alternate local minima may be found. Histograms with SNR 50 (Fig. 2.5c-e) illustrate

widening in the distribution of T2 results and emergence of two nB1 fit results, when simultaneously fitting for T2 and flip angle.
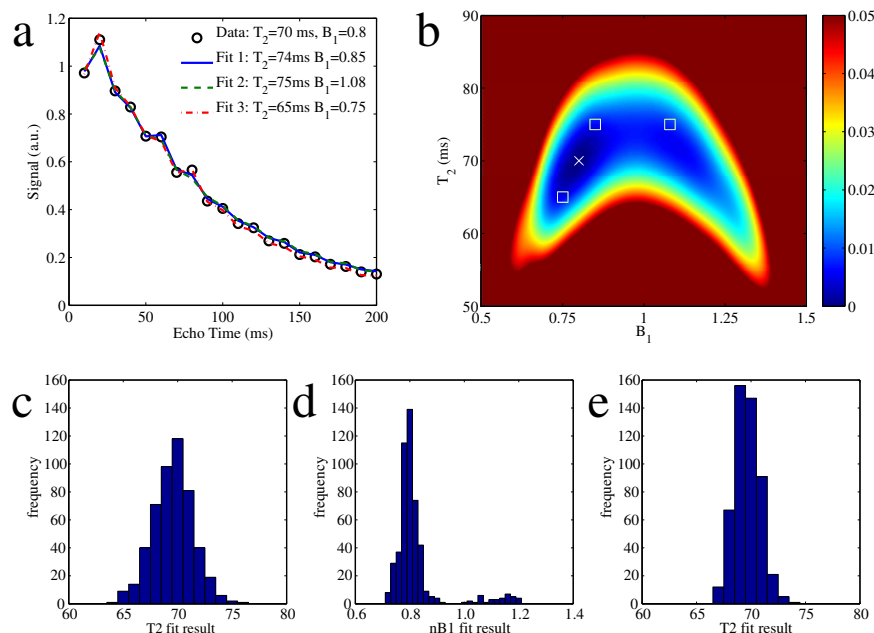
Figure 2.5: (a) Data points from a Bloch simulated curve with T2 = 70 ms and nB1 = 0.8 are shown with three incorrect fit curves, each with R2 0.99. (b) The sum squared residual compared to a range of dictionary curves is shown for the simulated (zero noise) curve. The correct fit is marked by ×, and □ indicates other curves from (a). Histograms of (c) T2 and (d) nB1 fit results from 500 repetitions of Bloch fitting with SNR = 50 demonstrate how noise impacts the nB1 measurement, and increases the uncertainty in T2 fit results relative to (e) two parameter T2 Bloch fitting.

2.3.2   Experimental Results

T2 and flip angle results from phantom experiments are shown in Table 2.1. Results from ISEC fitting methods using two and three parameter (abbreviated 2p and 3p in the table) are compared to T2 values from the single echo spin echo experiment, and measured flip angles from the double angle experiment, with most values found to be statistically significantly different (p < 0.01, with a Bonferroni correction for multiple corrections), as expected from simulation. Two parameter EPG fitting resulted in T2 estimates which were inconsistent with spin echo T2 results as predicted from simulation. Two parameter and three parameter Bloch fits yielded similar T2 to single spin echo.

For T2s below 50 ms, EPG_{FT} overestimates T2, which is improved by use of EPG_{SLR}. For longer T2, relative discrepancies between models in T2 fit results are smaller, with EPG_{FT} tending to provide longer T2 relative to Bloch fitting, and smaller differences are observed between Bloch and EPG_{SLR}. In terms of flip angles, the EPG methods perform poorly and the Bloch modelling generally yielded improved flip angle fit results, except in the 155° case which was mistaken for 202° due to approximate flip angle redundancy around 180°.

Mean T2 from nine volunteers in various grey and white matter regions are shown in Table 2.2, with example parameter maps from each fitting model shown in Fig. 2.6. T2 results of the two Bloch based methods were very similar. As expected, T2 values from EPG_{FT} are generally increased relative to the Bloch-ISEC methods. EPG_{SLR} methods typically resulted in T2 s being much closer to the Bloch results, agreeing within the standard deviations. EPG methods where nB1 was provided to the fitting algorithm generally resulted in significant mis-estimation of T2. In terms of flip angles, the Bloch method was generally most accurate, although in some cases low refocusing angles ($<$ 180°) were misinterpreted as being $>$ 180°.

Table 2.1: Comparing T2 fit values in Phantom data[a]

Sample	1	2	3	4
$[MnCl_2]$ (mM)	67.9	124.6	270	401.5
T1 (ms)	1166 $\pm$ 22	793 $\pm$ 16	454 $\pm$ 7	324 $\pm$ 4
T2 Measurement (ms)				
Spin Echo	99.4 $\pm$ 1.3	52.2 $\pm$ 0.7	24.9 $\pm$ 0.5	16.7 $\pm$ 0.4
Bloch-ISEC (2p)[b]	98.6 $\pm$ 0.9*	49.7 $\pm$ 0.5*	23.9 $\pm$ 0.6*	16.4 $\pm$ 0.3*
EPG_{FT}-ISEC (2p)	106.0 $\pm$ 1.0*	62.1 $\pm$ 0.7*	29.7 $\pm$ 0.7*	21.2 $\pm$ 0.4*
EPG_{SLR}-ISEC (2p)	93.6 $\pm$ 1.3*	57.0 $\pm$ 0.9*	25.6 $\pm$ 0.7*	17.8 $\pm$ 0.4*
Bloch-ISEC (3p)	97.2 $\pm$ 0.8*	50.3 $\pm$ 0.5*	23.8 $\pm$ 0.5*	16.5 $\pm$ 0.3*
EPG_{FT}-ISEC (3p)	100.6 $\pm$ 1.2*	53.5 $\pm$ 0.6*	26.8 $\pm$ 0.6*	18.9 $\pm$ 0.4*
EPG_{SLR}-ISEC (3p)	98.0 $\pm$ 1.2*	51.2 $\pm$ 0.6*	24.8 $\pm$ 0.6	17.1 $\pm$ 0.3*
Exponential fit	118.8 $\pm$ 2.4*	65.1 $\pm$ 0.8*	32.0 $\pm$ 0.7*	23.2 $\pm$ 0.4*
Refocusing Flip Angle Measurement (°)				
Double Angle	155.1 $\pm$ 7.8	210.2 $\pm$ 4.0	188.6 $\pm$ 4.3	190.1 $\pm$ 2.2
Bloch-ISEC	202.8 $\pm$ 8.5*	206.7 $\pm$ 2.9	192.7 $\pm$ 3.5*	189.5 $\pm$ 2.1
EPG_{FT}	139.9 $\pm$ 6.0*	138.1 $\pm$ 2.6	152.8 $\pm$ 2.3*	154.9 $\pm$ 2.2*
EPG_{SLR}	169.1 $\pm$ 8.1*	164.3 $\pm$ 3.6	179.6 $\pm$ 1.0*	179.8 $\pm$ 1.0*

[a] Data are reported as mean $\pm$ standard deviation within the ROI. Asterisks indicate T2 or flip angle values that are significantly different (P<0.01) from the spin echo or the double angle measurement.
[b] Two parameter and three parameter fits are indicated by 2p and 3p.
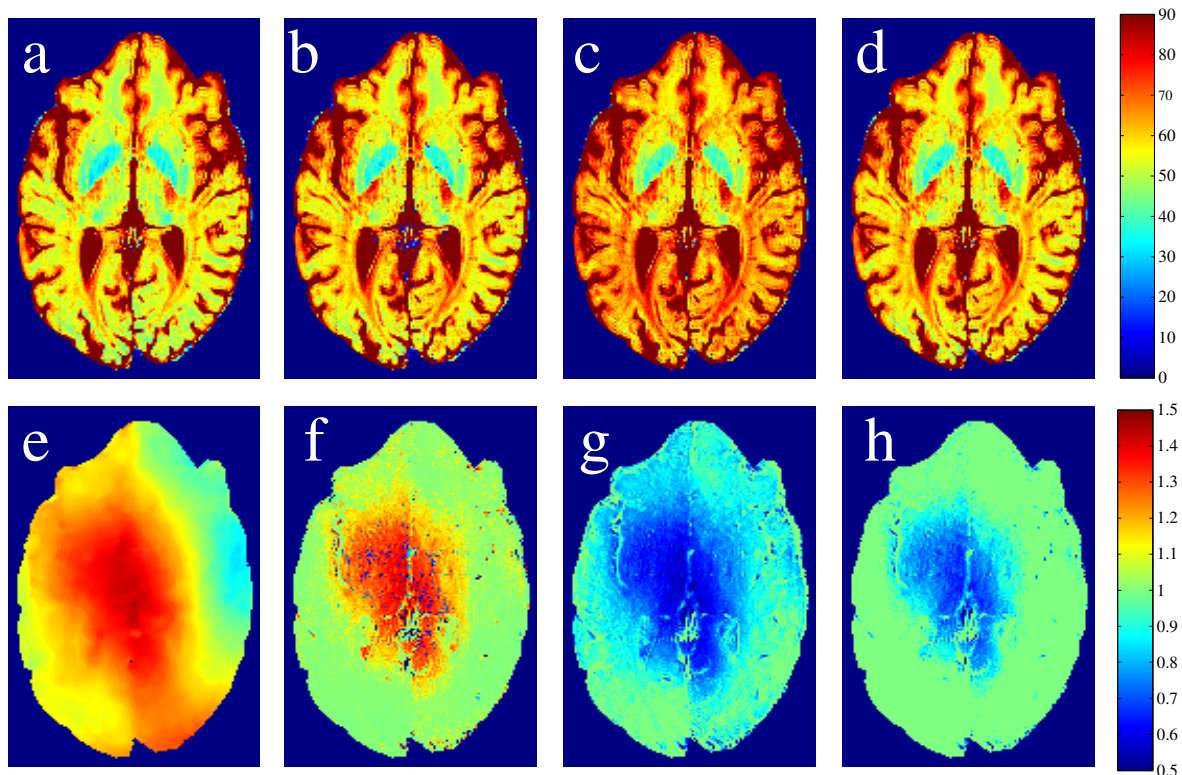
Figure 2.6: Maps from each of the methods are shown: (a) two and (b) 3 parameter Bloch-modelling, and 3 parameter (c) EPG_{FT} and (d) EPG_{SLR}. The measured nB1 (e) and the calculated nB1s are shown in (f,g,h) below their corresponding T2 maps for three parameter fits.

Table 2.2: T2 (ms) and Refocusing Flip Angles (°) from nine volunteers[a]

	Globus Pallidus	Caudate	Putamen	Thalamus	Posterior WM	Frontal WM
T2 Measurement (ms)						
Bloch-ISEC (2p)	34.9 1.9	58.2 ± 1.7	50.6 ± 3.1	52.5 ± 2.6	60.6 ± 4.8	52.3 ± 2.7
EPG_{FT}-ISEC (2p)	43.1 ± 2.2	67.6 ± 2.0	59.1 ± 3.1	64.5 ± 3.3	68.3 ± 5.1	58.8 ± 3.0
EPG_{SLR}-ISEC (2p)	37.8 ± 2.3	59.8 ± 2.1	51.8 ± 2.9	58.4 ± 3.7	59.3 ± 4.8	50.4 ± 2.9
Bloch-ISEC (3p)	35.1 ± 2.0	58.3 ± 1.6	50.7 ± 3.0	53.7 ± 2.5	61.2 ± 5.4	52.2 ± 2.5
EPG_{FT}-ISEC (3p)	40.4 ± 2.1	63.8 ± 1.7	56.0 ± 3.0	58.9 ± 3.0	68.0 ± 5.9	56.9 ± 2.9
EPG_{SLR}-ISEC (3p)	36.4 ± 1.9	59.3 ± 1.6	51.8 ± 2.9	54.9 ± 2.6	62.2 ± 5.4	53.3 ± 2.4
Exponential fit	46.4 ± 2.4	72.5 ± 1.9	63.9 ± 3.3	68.4 ± 3.5	75.9 ± 5.9	67.2 ± 2.7
Refocusing Flip Angle Measurement (°)						
Double Angle	192.1 ± 9.9	183.4 ± 8.1	181.2 ± 9.0	203.0 ± 11.2	166.4 ± 10.9	159.2 ± 10.0
Bloch	188.2 ± 5.9	186.4 ± 3.0	186.9 ± 3.2	192.7 ± 10.0	185.8 ± 5.6	196.6 ± 7.3
EPG_{FT}	160.4 ± 6.7	157.0 ± 3.6	157.5 ± 3.8	153.4 ± 11.1	163.3 ± 8.7	149.1 ± 6.7
EPG_{SLR}	178.1 ± 2.9	179.3 ± 1.0	179.1 ± 1.1	175.4 ± 7.9	178.8 ± 2.3	173.0 ± 4.9

[a] Values are reported as mean $\pm$ SD within the group averaged results.
[b] Two parameter and three parameter fits are indicated by 2p and 3p.

Computation time on a typical volunteer data set for EPG_{SLR} was 49 minutes for 2 parameter fitting, and 92 minutes for 3 parameter fitting. EPG_{FT} is 43 and 86 min-

utes for 2 and 3 parameter fitting. Bloch is 22 and 39 minutes for 2 and 3 parameter fitting. However, the Bloch approach also requires prior generation of a dictionary of curves, which is very time consuming, taking approximately 50 hours using 8 processors in parallel to generate the 510711 curves used in the volunteer study. Exponential fitting required 8.4 minutes, although results were erroneous. These timings are when running MATLAB 2014a on a 16 × 2.4 GHz core system with 48 GB of RAM, running 64 bit Ubuntu 14.04. Computation time could be decreased with parallel processing for fitting, and more optimized implementations.

2.4 Discussion

Bloch, EPG_{FT} and EPG_{SLR} simulations of slice selective MESE each produce different decay curves due to different treatment of the RF pulse response. Nevertheless, three parameter EPG and Bloch, and two parameter Bloch models can produce high quality T2 fits, yielding systematically different, but similar, T2 values in most cases. T2 values in specific brain structures were found to be in agreement with published results at the same field strength [18, 28, 29], and differences in resulting parameter maps between each model appear consistent with simulated differences. The three parameter EPG methods overestimate T2 relative to the Bloch approaches, with EPG_{FT} producing the largest differences. The two parameter EPG methods, with provided flip angles, provide erroneous T2 values.

Each method produces starkly different flip angle maps, which follows from the different treatment of RF pulses. In general, the flip angle maps produced are not precise, and exact knowledge of flip angle response requires a separate flip angle map measurement, as was used in the two parameter Bloch approach. The consequences of these RF effects are relatively minor on resulting T2 maps, except when a known flip angle map is applied to EPG fits, which results in substantial T2 fit errors. Unlike the Bloch approach, where RF pulses are properly treated, the EPG methods use an inaccurate slice profile model, which results in systematic mis-estimation of flip angle maps. When the flip angle is forced to be exact, slice selective EPG solutions result in large T2 errors. The slice pro-

file approximation, used in EPG_{FT}, overestimates the flip angle profile yielding a reduced flip angle result which is improved with the use of EPG_{SLR}. However, both EPG methods use a pre-calculated flip angle distribution, which is identical for every refocusing pulse. By moving to a full Bloch simulation, the RF pulse response is fully accounted for, which enables provision of a flip angle map to minimize fitting parameters. If exact flip angles are known for each voxel, this information is best applied with the full Bloch simulation, and is not recommended with the EPG approach.

Differences between T2 fitting models are further exacerbated when only a few data points have high SNR. When the T2 is short relative to the inter-echo spacing and echo train duration, only a few points provide information about the decay, and the remaining points are mostly noise. This may impact fit accuracy, and the algorithm may benefit from weighting fits with signal amplitude, or truncating echo trains once the signal magnitude drops to near noise levels. For example, when T2 is below 50 ms, EPG_{FT} results in overestimates which can exceed 10%. The different models yield more similar results at longer decay times. In this case, the use of 10 ms inter-echo spacing limits the number of high SNR data points for shorter T2 values. Decreasing the first echo time, and reducing echo spacing should improve quantification of shorter T2. In all cases, results in our study may be scaled for different inter-echo spacings by maintaining the same inter-echo spacing to T2 ratio. Here, we do not examine T2 less than 20 ms (2 × the echo spacing).

EPG-ISEC limits the range of refocusing angles to ≤180° to avoid redundant solutions, assuming that symmetry around this refocusing angle occurs. However, symmetry was not observed around refocusing angles of 180° in any of the models of slice-selective MESE, and thus the Bloch-ISEC method does not assume such redundancy. In real (noisy) data, the three parameter Bloch-ISEC method can have difficulty distinguishing between local minima at high and low flip angles. To help prevent this, we applied a pattern recognition fitting method, as described by [20, 22], to avoid convergence on local minima, or difficulties in fitting to the lookup table when starting guesses were poor. However, this does not entirely eliminate the alternative solution being chosen, and results showed in some cases low (<180°) refocusing angles were misinterpreted as

57

high flip angles. Fitting may benefit from regularization, or constraints on flip angle solutions. Alternatively, use of a lower refocusing angle that is always <180° would remove the issue of multiple solutions where nB1 and T2 are simultaneously fit; however this would increase T1 effects.

Limitations of this work include a lack of a true gold standard for T2 measurement. The single echo spin echo T2 measurement was used for phantom T2 comparisons, but suffers from a long acquisition time, which limits in vivo use. Although the single spin echo produces no stimulated echoes, it uses variable inter-echo spacing, which increases with longer TEs and exposes the sequence to diffusion effects that can lead to substantial signal loss in regions of microscopic magnetic inhomogeneity [30]. A further limitation is the consideration of only T2 values < 100 ms. In particular cerebrospinal fluid was not considered due to the relatively short echo train duration. In addition only single component solutions were examined, even though WM voxels and partial volume effects would be expected to have multiple T2 components. Finally, Gaussian RF pulses were used with refocusing widths of 1.75 times excitation. The pulse shape was chosen to limit RF heating effects at high field, with the wider refocusing width compensating for the poorer RF profile. Other profiles may give different results. Sharper profiles may have less variation across the profile, but contiguous slices would require a significant reduction in relative refocusing width. Effects of relative refocusing width have been previously considered for EPG [18].

2.5 Conclusion

Slice selective decay curves differ substantially between methods and are not symmetric about 180° refocusing angles. Differences in the simulated decay curves arise mainly from the modelling of RF profile response. Highly inaccurate flip angles are obtained with the EPG_{FT} method with only marginal improvement using EPG_{SLR}. Nevertheless, T2 values are similar with all EPG and Bloch models in most cases, although the T2 values are systematically slightly different. Providing measured flip angles to EPG methods yields erroneous T2, thus EPG-based methods should not be implemented as a two-parameter

fitting with input flip angles, rather EPG should include the flip angle in the fitting process (three-parameter). In contrast, provision of accurate flip angles to the Bloch approach yields accurate T2 and can remove effects of flip angle redundancy, which can yield multiple solutions especially in cases of reduced SNR. When available, the more complex Bloch fitting is preferred over EPG, but the much simpler EPG approach can still provide excellent T2 results in most cases when SNR is adequate and sufficient data points are available.

Acknowledgements

References

[1] José M. Alústiza, José Artetxe, Agustín Castiella, Cristina Agirre, José I. Emparanza, Pedro Otazua, Manuel García-Bengoechea, Jess Barrio, Fernando Mjica, and José A. Recondo. MR Quantification of Hepatic Iron Concentration1. *Radiology*, 230(2):479–484, February 2004.

[2] Nilesh R. Ghugre, Thomas D. Coates, Marvin D. Nelson, and John C. Wood. Mechanisms of Tissue-Iron Relaxivity: Nuclear Magnetic Resonance Studies of Human Liver Biopsy Specimens. *Magnetic resonance in medicine : official journal of the Society of Magnetic Resonance in Medicine / Society of Magnetic Resonance in Medicine*, 54(5):1185–1193, November 2005.

[3] Shivraman Giri, Yiu-Cho Chung, Ali Merchant, Georgeta Mihai, Sanjay Rajagopalan, Subha V. Raman, and Orlando P. Simonetti. T2 quantification for improved detection of myocardial edema. *Journal of Cardiovascular Magnetic Resonance*, 11(1), December 2009.

[4] David Verhaert, Paaladinesh Thavendiranathan, Shivraman Giri, Georgeta Mihai, Sanjay Rajagopalan, Orlando P. Simonetti, and Subha V. Raman. Direct T2 Quantification of Myocardial Edema in Acute Ischemic Injury. *JACC: Cardiovascular Imaging*, 4(3):269–278, March 2011.

[5] A.L. MacKay, I.M. Vavasour, A. Rauscher, S.H. Kolind, B. M adler, G.R.W. Moore, A.L. Traboulsee, D.K.B. Li, and C. Laule. MR Relaxation in Multiple Sclerosis. *Neuroimaging Clinics of North America*, 19(1):1–26, February 2009.

[6] Kenneth P Whittall, Alex L. Mackay, Douglas A. Graeb, Robert A. Nugent, David K. B. Li, and Donald W. Paty. In vivo measurement of T2 distributions and water contents in normal human brain. *Magnetic Resonance in Medicine*, 37(1):34–43, 1997.

[7] John F. Schenck and Earl A. Zimmerman. High-field magnetic resonance imaging of brain iron: birth of a biomarker? *NMR in Biomedicine*, 17(7):433–445, 2004.

[8] Andrew J. Walsh, R. Marc Lebel, Amir Eissa, Gregg Blevins, Ingrid Catz, Jian-Qiang Lu, Lothar Resch, Edward S. Johnson, Derek J. Emery, Kenneth G. Warren, and Alan H. Wilman. Multiple Sclerosis: Validation of MR Imaging for Quantification and Detection of Iron. *Radiology*, 267(2):531–542, May 2013.

[9] Khader M. Hasan, Christopher Halphen, Arash Kamali, Flavia M. Nelson, Jerry S. Wolinsky, and Ponnada A. Narayana. Caudate Nuclei Volume, Diffusion Tensor Metrics, and T2 Relaxation in Healthy Adults and Relapsing-Remitting Multiple Sclerosis Patients: Implications to Understanding Gray Matter Degeneration. *Journal of magnetic resonance imaging : JMRI*, 29(1):70–77, January 2009.

[10] Josef Vymazal, Rodney A. Brooks, Charles Baumgarner, Vu Tran, David Katz, Jeff W. M. Bulte, E. Rivka Bauminger, and Giovanni Di Chiro. The relation between brain iron and NMR relaxation times: An in vitro study. *Magnetic Resonance in Medicine*, 35(1):56–61, 1996.

[11] Sean C.L. Deoni. Transverse relaxation time (T2) mapping in the brain with off-resonance correction using phase-cycled steady-state free precession imaging. *Journal of Magnetic Resonance Imaging*, 30(2):411–417, August 2009.

[12] Ke Li, Richard D. Dortch, E. Brian Welch, Nathan D. Bryant, Amanda K.W. Buck, Theodore F. Towse, Daniel F. Gochberg, Mark D. Does, Bruce M. Damon, and Jane H. Park. Multi-parametric MRI characterization of healthy human thigh muscles at 3.0T - relaxation, magnetization transfer, fatwater, and diffusion tensor imaging. *NMR in biomedicine*, 27(9):1070–1084, September 2014.

[13] Rebecca J. Willcocks, William D. Rooney, William T. Triplett, Sean C. Forbes, Donovan J. Lott, Claudia R. Senesac, Michael J. Daniels, Dah-Jyuu Wang, Ann T. Harrington, Gihan I. Tennekoon, Barry S. Russman, Erika L. Finanger, Barry J. Byrne, Richard S. Finkel, Glenn A. Walter, H. Lee Sweeney, and Krista Vandenborne. Multicenter prospective longitudinal study of magnetic resonance biomarkers

in a large duchenne muscular dystrophy cohort. *Annals of Neurology*, 79(4):535–547, April 2016.

[14] Timothy C. Dunn, Ying Lu, Hua Jin, Michael D. Ries, and Sharmila Majumdar. T2 Relaxation Time of Cartilage at MR Imaging: Comparison with Severity of Knee Osteoarthritis. *Radiology*, 232(2):592–598, August 2004.

[15] Stephen J Matzat, Jasper van Tiel, Garry E Gold, and Edwin H G Oei. Quantitative MRI techniques of cartilage composition. *Quantitative imaging in medicine and surgery*, 3(3):162–174, June 2013.

[16] A. Amirabadi, L. Vidarsson, E. Miller, M. S. Sussman, K. Patil, H. Gahunia, S. A. F. Peel, A. Zhong, R. Weiss, G. Detzler, H. L. M. Cheng, R. Moineddin, and A. S. Doria. USPIO-related T1 and T2 mapping MRI of cartilage in a rabbit model of blood-induced arthritis: a pilot study. *Haemophilia*, 21(1):e59–e69, January 2015.

[17] Jürgen Hennig. Echoes - how to generate, recognize, use or avoid them in MR-imaging sequences. Part I: Fundamental and not so fundamental properties of spin echoes. *Concepts in Magnetic Resonance*, 3(3):125–143, 1991.

[18] R. Marc Lebel and Alan H. Wilman. Transverse relaxometry with stimulated echo compensation. *Magnetic Resonance in Medicine*, 64(4):1005–1014, 2010.

[19] J.T. Vaughan, M. Garwood, C.m. Collins, W. Liu, L. DelaBarre, G. Adriany, P. Andersen, H. Merkle, R. Goebel, M.b. Smith, and K. Ugurbil. 7t vs. 4t: RF power, homogeneity, and signal-to-noise comparison in head images. *Magnetic Resonance in Medicine*, 46(1):24–30, July 2001.

[20] Noam Ben-Eliezer, Daniel K. Sodickson, and Kai Tobias Block. Rapid and accurate T_2 mapping from multi-spin-echo data using Bloch-simulation-based reconstruction: Mapping Using Bloch-Simulation-Based Reconstruction. *Magnetic Resonance in Medicine*, 73(2):809–817, 2015.

[21] Kelly C. McPhee and Alan H. Wilman. T2 quantification from only proton density

and T2-weighted MRI by modelling actual refocusing angles. *NeuroImage*, 118:642–650, September 2015.

[22] Chuan Huang, Maria I. Altbach, and Georges El Fakhri. Pattern recognition for rapid T2 mapping with stimulated echo compensation. *Magnetic Resonance Imaging*, 32(7):969–974, September 2014.

[23] J. Pauly, P. Le Roux, Dwight Nishimura, and A. Macovski. Parameter relations for the Shinnar-Le Roux selective excitation pulse design algorithm [NMR imaging]. *IEEE Transactions on Medical Imaging*, 10(1):53–65, 1991.

[24] Brian Hargreaves. Bloch Equation Simulator. http://www-mrsrl.stanford.edu/ brian/blochsim/, 2003. Date Accessed: 2016-04-08.

[25] R Marc Lebel. StimFit: A toolbox for robust T2 mapping with stimulated echo compensation. In *Proceedings of the Meeting of the International Society for Magnetic Resonance in Medicine*, page 2558, Melbourne, Australia, 2012.

[26] Rudolf Stollberger and Paul Wach. Imaging of the active B1 field in vivo. *Magnetic Resonance in Medicine*, 35(2):246–251, 1996.

[27] Mustapha Bouhrara and Jean-Marie Bonny. B1 mapping with selective pulses. *Magnetic Resonance in Medicine*, 68(5):1472–1480, November 2012.

[28] Fumiyuki Mitsumori, Hidehiro Watanabe, and Nobuhiro Takaya. Estimation of brain iron concentration in vivo using a linear relationship between regional iron and apparent transverse relaxation rate of the tissue water at 4.7t. *Magnetic Resonance in Medicine*, 62(5):1326–1330, 2009.

[29] Md. Nasir Uddin, R. Marc Lebel, and Alan H. Wilman. Transverse relaxometry with reduced echo train lengths via stimulated echo compensation. *Magnetic Resonance in Medicine*, 70(5):1340–1346, 2013.

[30] Alexander G. Gardener, Susan T. Francis, Malcolm Prior, Andrew Peters, and Penny A. Gowland. Dependence of blood R2 relaxivity on CPMG echo-spacing at 2.35 and 7 T. *Magnetic Resonance in Medicine*, 64(4):967–974, October 2010.

Chapter 3

Limitations of Skipping Echoes for Exponential T2 Fitting

BACKGROUND: Exponential fitting of multi-echo spin echo sequences with skipped-echoes is still commonly used for quantification of transverse relaxation (T2).

PURPOSE: To examine the efficacy of skipped-echo methods for T2 quantification against computational modelling of the exact signal decay.

STUDY TYPE: Prospective comparison of methods.

SUBJECTS/PHANTOM: Eight volunteers were imaged at 4.7T, six volunteers at 1.5T and T2 phantoms.

FIELD STRENGTH/SEQUENCE: 1.5T and 4.7T, T2 fitting of multiple-echo spin echoes.

ASSESSMENT: Fitting of exponential T2 using all echoes, skipping the first echo or skipping all odd echoes, compared with Bloch simulations. Error in resulting T2 values is examined over a range of T2 (10-150ms), refocussing flip angles (90-270°) and echo train lengths (6-32).

STATISTICAL TEST: Shapiro-Wilk tests and Q-Q plots were used to check for normality of data. Paired sample t-tests and Wilcoxon rank tests were

used compare fitting models using α=0.05. Multiple comparisons were accounted for with Bonferroni correction.

RESULTS: Skipping echoes was insufficient to avoid stimulated echo contamination, and improvement over full exponential fitting was highly dependent on the refocusing flip angle, actual T2 value, and the number of echoes available. Simulations showed skipping the first echo was the most effective form of exponential fitting offering particular advantages for short T2 and short echo trains. In vivo skipped echo T2 values were significantly different than all echo exponential fitting (P<0.004), but also were significantly different from reference values (P<0.002, except in frontal white matter). In general, both skipped-echo approaches still produce large errors, particularly for deviations from 180° refocusing. Typical mis-estimation of T2 in vivo ranged from 23-39% in examined ROIs for exponential fitting of all echoes, or 15-32% for skipped-echo methods.

DATA CONCLUSION: Skipped-echo fitting methods are insufficient for avoiding stimulated echo contamination with T2 errors depending on a complicated interplay of T2, refocusing angle, and echo train length. Modelling of the multi-echo sequence is recommended.

3.1 Introduction

Quantitative Transverse Relaxation (T2) is frequently used for characterization of tissue in vivo, including examination of muscle [1], joints [2–4], liver [5, 6], heart [5, 7], and brain [8–10]. The most common approach to T2 measurement is fitting of multi-echo spin echo (MESE) data. Imperfect refocussing due to slice profile [11], radiofrequency interference [12], or purposeful reduction of refocussing angles all result in indirect and stimulated echoes, which contaminate the signal decay [13, 14]. An obvious indicator of substantial contamination from stimulated echoes is an increased intensity of the second echo in comparison to the first echo. Fitting such data with standard exponential fitting results in T2 mis-estimation [15]. Methods now exist which yield accurate T2 despite imperfect

refocusing by computationally modelling the signal response for all echo pathways [14, 16–18]. However, even with availability of software for more advanced fitting, expert use is still necessary for code implementation and requires knowledge of detailed sequence parameters including exact flip angle trains and RF pulse shapes. Hence, exponential fitting remains persistent [3, 4, 6, 7, 19–21] due to its extreme simplicity and ease of implementation. Some researchers have acknowledged stimulated echoes as a limitation in their study, when using exponential fitting [4, 6, 7, 19]. Other researchers have sought simple remedies to limit the effects of stimulated echoes by removing echoes but still using an exponential fit, either skipping the first echo in the train [1, 2, 22–30] or all odd echoes [5, 31]. Both of these approaches are thought to improve exponential T2 fitting by reducing errors caused by spurious echoes. However, the accuracy of skipped echo methods has not been fully detailed across a range of T2, refocusing angles and echo train lengths. Here, we examine the effectiveness of these simple remedies for T2 measurement by comparing to a proven computational echo modelling approach.

3.2 Methods

Two-dimensional, slice selective, multi-echo spin echo (MESE) experiments were carried out in simulations, phantom, and in vivo human brain at 1.5 and 4.7 T to examine accuracy of exponential T2 fitting using all points, rejecting the first echo, or rejecting all odd echoes. For comparison in vivo, a full computational model for T2 fitting was used, employing a measured flip angle map and Bloch simulations for Indirect and Stimulated Echo Compensation (ISEC) [17] (sometimes referred to as the Echo Modulation Curve (EMC) algorithm [16]). In phantom, single spin echo experiments were used for comparison.

3.2.1 Simulations

Simulations were used to examine efficacy of the exponential fitting schemes for sequences with a range of refocusing widths (non-selective, 1.75 $\times$ and 3 $\times$ excitation width), refocusing angles (90°-270°) and T2 values (10-150 ms), and longitudinal relaxation time

(T1, 1 s). Simulations of MESE signal amplitudes employed Shinnar-Le Roux (SLR) [32] simulations for RF pulses, and Bloch solutions for relaxation decay between pulses similar to previously described methods [17]. Simulations were also performed using RF pulse shapes and timings matching all in vivo experiments at both field strengths. Simulated data were fit with exponential curves using either all echoes, only even echoes, or discarding only the first echo. Fitting of retrospectively truncated echo trains was also performed to examine the impact of the number of echoes. All simulations and image processing were performed using custom in-house MATLAB (R2014a, 64 bit) programs.

3.2.2 In Vivo Experiments

Human brain experiments were performed on a 4.7T (Varian Inova), or a 1.5T (Siemens Sonata) MRI system. All subjects provided written, informed consent, and this investigation was approved by the local institutional ethics board.

Multi-echo spin echo (CPMG) images were acquired with oblique transverse orientation through iron-rich deep grey matter. Eight volunteers (5 male, mean age 30, range 25 - 38 yrs) were studied at 4.7T and six volunteers were studied at 1.5T (4 male, mean age 28, range 25-38 yrs). 4.7T parameters were repetition time (TR) 3 s or 4 s, echo train length (ETL) 32, echo time (TE) 10 to 320 ms, echo spacing 10 ms, prescribed excitation 90°, prescribed refocusing 180°, relative refocusing width 1.75, matrix 256 $\times$ 145, voxel size $1 \times 1.25 \times 4$ mm^3. Acquisition parameters for the 1.5T experiments were TR 4000 ms, ETL 12 (some subjects had longer trains which were retrospectively reduced to 12 for fitting), TE 12.4 ms to 148.9, echo spacing 12.4 ms, prescribed excitation 90°, prescribed refocusing 180°, relative refocusing width 1.0, matrix 256 $\times$192, voxel size $0.94 \times 0.94 \times 5$ mm^3. The RF pulse shapes at 4.7T were Gaussian with time-bandwidth product 2.69, 5 sigma width, and the 1.5T used proprietary customized single lobe RF pulse shapes similar to sinc-Gauss with the RF pulse shape waveform.

3.2.3 Phantom Experiments

MESE experiments were repeated in phantoms at 4.7T, with comparison to a single spin echo, which uses only a single refocusing pulse, and thus exhibits only direct spin echoes. $MnCl_2$ solutions (68 - 270 mM) were placed in 28 mm diameter cylindrical plastic laboratory tubes. A series of single spin echo experiments were performed (TE 14, 20, 30, 50, 70 ms, TR 14 s, nominal excitation angle 90°, nominal refocusing angle 180°, sinc pulse shapes). MESE data and a flip angle map were acquired during the same imaging session, with parameters matched to in vivo experiments, with the exception of 10 mm slice thickness for all experiments, and TR 14 s for flip angle mapping.

3.2.4 Flip Angle Mapping

Exact flip angles were determined using a double angle method [33] with a correction for slice profile [34]. For 4.7T acquisitions, a pair of fast spin echo images were acquired (TR 7000 ms; excitation angle 60°, 120°; effective TE 43 ms; pulse shapes and resolution were matched to MESE data). For 1.5T acquisitions, a pair of echo planar images were acquired (excitation angle = 60°, 120°, TR 7050 ms, TE 40 ms, imaging matrix 128 × 128; FOV 240× 240 mm^2, slice thickness 2 mm, and acquisition time 7 sec each). In order to avoid errors due to slice profile, the pair of sequences were simulated, as described above, to determine the relative signal intensities for each possible flip angle. A 5×5 median filter was applied to B1 maps prior to use for T2 fitting. Flip angle maps were expressed as a normalized factor (B1) relating the refocussing angle achieved to the prescribed refocussing angle.

3.2.5 T2 Measurement

The phantom and in vivo MESE signal magnitudes were fit to an exponential function $S = A_0 \exp(-TE/T2)$, using a non-linear least squares algorithm. Fitting was applied to all echoes, with and without the first echo, and to even echoes only. For comparison in vivo, MESE data sets were also fit using the ISEC T2 fitting model, which used the experimentally measured flip angle map and fits for decay simulations as previously

described [17]. A constant T1 of 2 s was used for all Bloch simulations for fitting. T2 averages in vivo were calculated in regions of interest (ROI), drawn manually, selecting grey matter (caudate, putamen, globus pallidus, thalamus) and white matter territories (frontal white matter and posterior white matter).

For phantom experiments, the single spin echo data was used for reference values, and was fit with a pure exponential function as described above for in vivo MESE data. Average T2 within circular ROIs ($\sim$ 21 mm diameter) at the centre of each tube were used.

Truncated echo trains for skipped echo fitting was also examined. In vivo results from one subject in three ROIs were examined. Phantom results from fitting truncated echo trains were compared to fitting simulated curves created using the average measured B1 within a small ROI ($\sim$4 $\times$ 4 mm^2), T2 values from single spin echo experiments, and T1 of 1 s. Small ROIs were used to avoid averaging various amounts of stimulated echoes due to substantial variation in B1 across the field of view.

3.2.6 Statistics

Shapiro-Wilk tests and Q-Q plots were used to check for normality of data. Paired sample t-tests and Wilcoxon tests were performed to test if each T2 fitting method was significantly different from the gold standard. T2 values from each skipped echo method were compared to exponential fitting of all echoes, and skipping the first echo was compared to skipping all odd echoes. Multiple comparisons of T2 fitting methods were accounted for with Bonferroni correction, and analysis was carried out using $\alpha = 0.05$.

3.3 Results

Simulated decay curves (Figure 3.1) illustrate that in slice selective experiments, all echoes after the first are contaminated with stimulated and/or indirect echo components, with the largest increase in stimulated echo component between the first and second echo, and spurious echo fraction continues to increase with each subsequent echo, even though

the net signal is decreasing. Exponential fitting of simulated slice selective 32 echo T2 decay curves (Figures 3.1 and 3.2) show that T2 is mis-estimated by various degrees depending on the exponential fitting scheme, as well as the refocusing angle, relative width, and actual T2 value. Slice selective experiments (Figure 3.2 top and middle row) perform poorest, though non-selective experiments also mis-estimate T2, unless the refocusing angle is exactly 180° (simulations using parameters based on the 12 echo 1.5T experiments are shown in Supplementary Figure A.5). At 32 echoes, skipping echoes has greatest benefit for short T2 times with skipping only the first echo being most effective, though T2 is still overestimated by at least 13% in the brain. Decreasing from 32 to 12, 8 or 6 echoes, increases the value of skipping echoes over all echo exponential fitting (Figure 3.3). In these cases, substantial benefit is achieved by skipping echoes to avoid the extreme errors of full exponential fitting. In general, skipping the first echo is more effective than skipping all odd echoes for these shorter echo trains (Figure 3.4), though overall, the skipped echo methods were not found to be significantly different in most of the examined ROIs. In all cases, as refocusing angles deviate from 180°, errors in T2 increase. The echo number dependence on T2 fitting is further examined in Figure 3.4, where phantom and in vivo data are compared to simulation. Decreasing the echo train length tends to lead to more accuracy in skipped echo methods, but less accuracy in full exponential fitting. Effects of echo train length on full exponential fitting agree with previously reported findings [35].

In vivo T2 values (mean ± standard deviation across the group) using all 32 echoes, and for 8 echoes for each of the T2 fitting schemes are shown in Table 3.1 for 4.7T and in Table 3.2 for 12 echo 1.5T experiments. All exponential fitting schemes over-estimate T2, relative to the ISEC method. T2 maps from one subject from 4.7T are shown in Figure 3.5. Each method provides different results, with the exponential fit of all echoes showing the longest T2 values (Fig 3.5b), and ISEC showing the shortest T2 values (Fig 3.5a). T2 values were typically overestimated by 23-39% in examined ROIs for exponential fitting of all echoes, and 15-32% for skipped echo methods. SNR in vivo typically exceeded 80 within the examined ROIs. Use of a truncated 8 echo train (Fig 3.5 f-h) shows improvement in skipped echo exponential fitting. However, overestimation
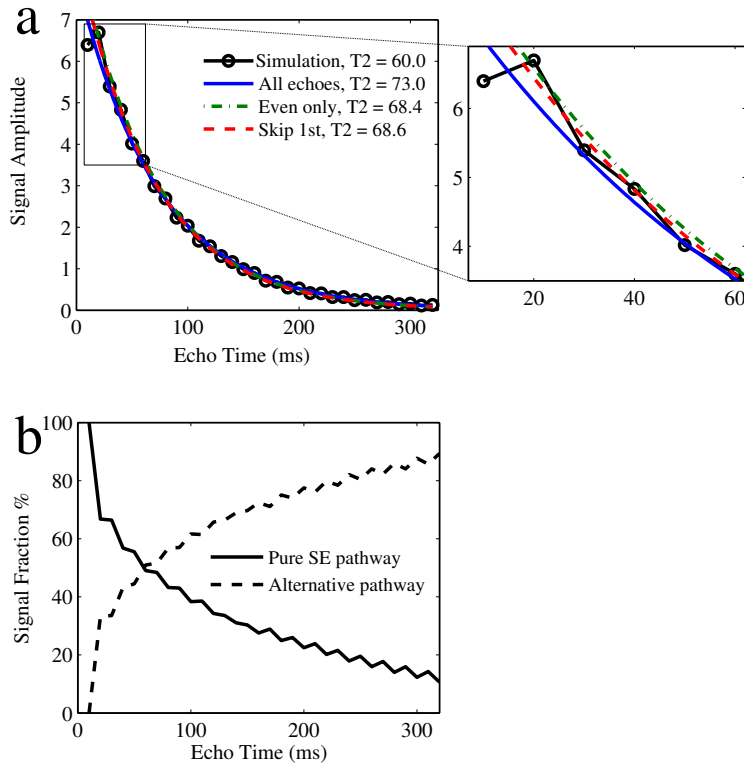
Figure 3.1: (a) A simulated slice selective MESE decay curve for 180° and T2 = 60 ms (black line with circles) is shown with three exponential fit curves (all echoes, blue line; even echoes only, green; all echoes except the first, red). T2 fit values varied depending on echoes used for fitting. (b) The fraction of the total signal and signal intensity due to the direct Spin Echo (SE) pathway (solid line), is compared to signal arising from all other pathways (dashed line). Simulations were based on sequence parameters from 4.7T experiments.

relative to the ISEC model is still evident.

When examining 4.7T data, exponential methods (with all echoes, or skipping echoes) were found to be significantly different from gold standard values (P ≤ 0.0006 for all values except skipped echo methods in frontal white matter in 8 echo data sets, P = 0.01). Skipped echo methods were found to be significantly different from exponential fitting of all echoes (P ≤ 0.003, except for 32 echo skipped echo methods in frontal white matter (P = 0.03 for skipping the first echo, and P= 0.007 for skipping odd echoes)). Skipping the first echo and skipping even echoes was found to be significantly different in only about half of ROIs. Data from volunteers imaged at 1.5 T also indicated that that
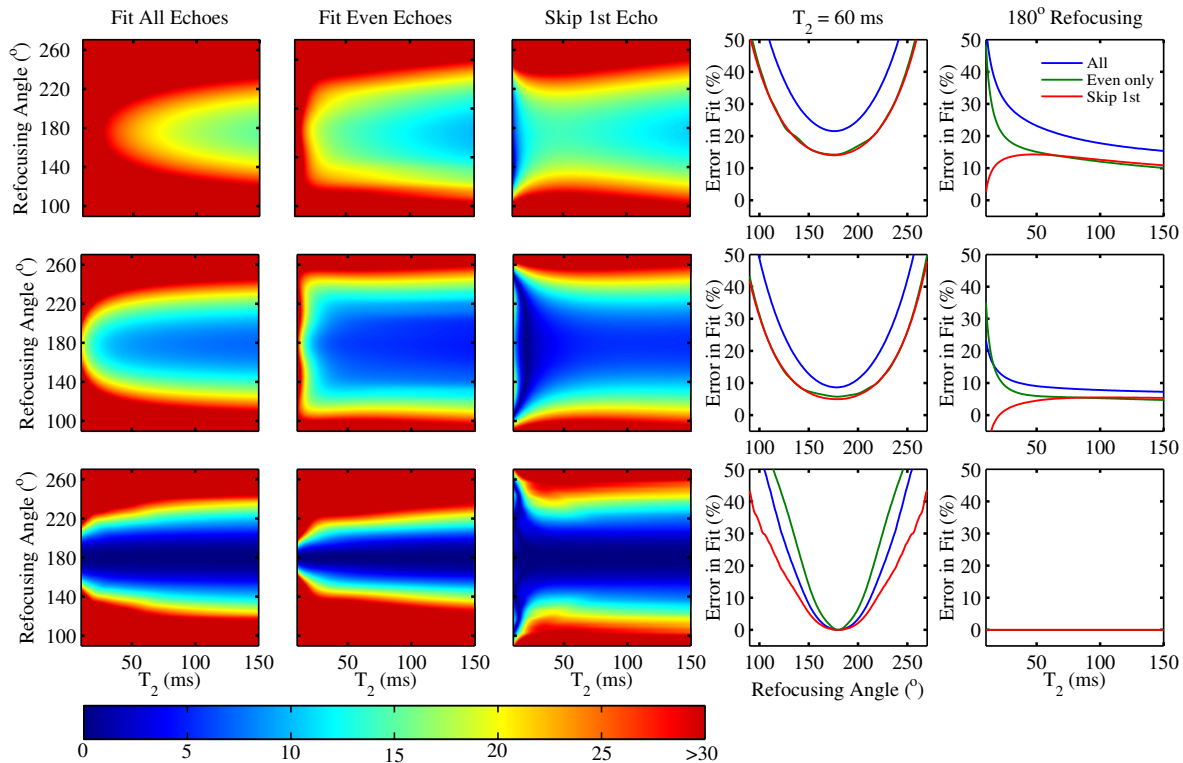
Figure 3.2: The effect of relative refocussing width on absolute percent error in exponential T2 fit of simulated data (based on 4.7T pulse sequence and imaging parameters) is examined. Error maps of exponential T2 fit using 32 echoes with 10 ms spacing for a range of T2 (10-150 ms) and refocusing angles (90°-270°): left column all echoes fit, 2nd column even echoes fit, 3rd column skipping first echo only. Refocusing width is altered vertically, with top row 1.75 × excitation, centre row 3×, and non-selective refocusing at bottom. Line plots showing error in T2 fit as a function of refocusing angle, at a T2 of 60 ms (4th column), and as a function of T2 with 180° refocusing (far right) are shown on the right

all exponential methods were significantly different from ISEC fitting ($P \leq 0.002$), and skipped echo methods were found to be significantly different from exponential fitting of all echoes ($P \leq 0.004$). Skipping the first echo was not found to provide significantly different results than skipping all odd echoes (P ranged from 0.6 - 1.0).

3.4 Discussion

Two common T2 correction schemes were considered: skipping the first echo or skipping all odd echoes. These skipped methods were generally preferable to full exponential
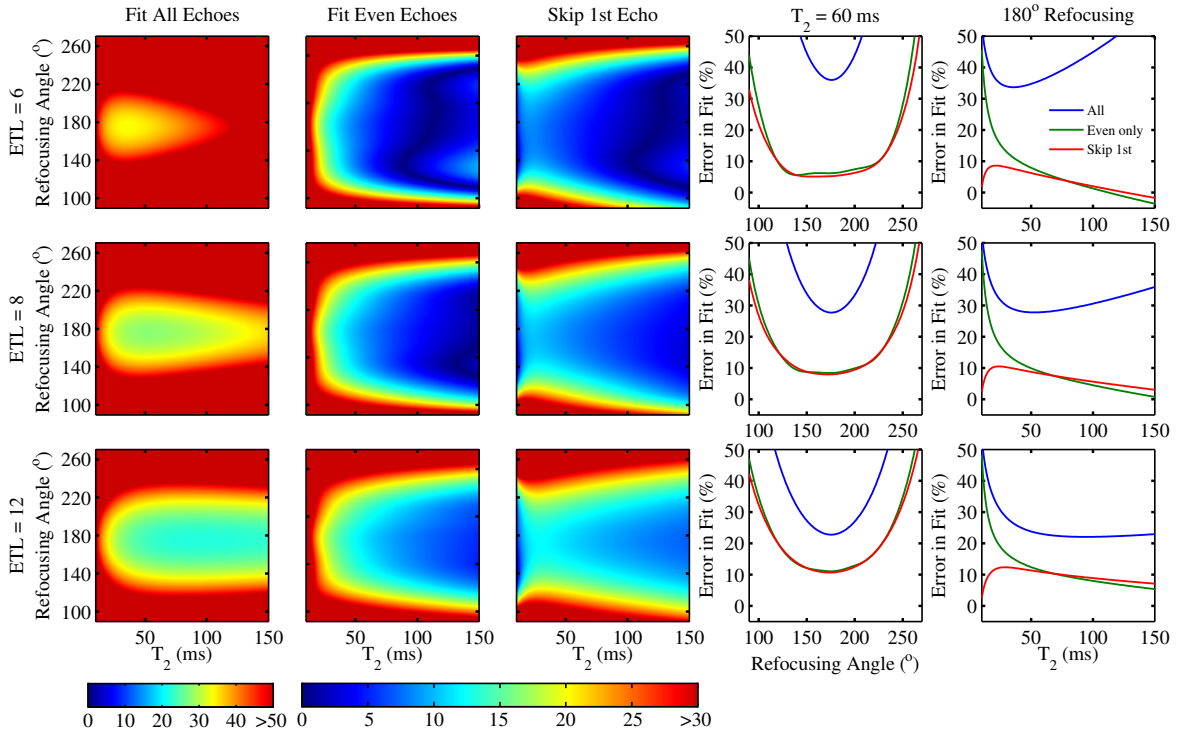
Figure 3.3: Effect of reduced echo train length (ETL = 6, 8, 12) on absolute percent error in exponential T2 fit of simulated data (based on 4.7T pulse sequence and imaging parameters) is examined for a range of T2 (10-150 ms) and refocusing angles (90°-270°): left column all echoes, 2nd column even echoes, 3rd column skipping first echo only. ETL is altered between rows: 6 top, 8 middle, and 12 bottom. Echo spacing is 10 ms throughout with 1.75 relative refocusing width. At right, line plots showing error in T2 fit as a function of refocusing angle, at a T2 of 60 ms, and as a function of T2 with 180° refocusing are also shown.

fitting, though neither was capable of eliminating all errors due to stimulated echoes. The starkest improvements over full exponential fitting were found when using reduced echo train numbers in slice selective experiments. Simulations showed the two skipped echo methods diverged in performance for short T2 (< 50 ms), where skipping only the first echo was preferred since this enabled sufficient echoes to be available rather than skipping all odd echoes. Thus as a general rule, if exponential fitting must be applied, we recommend skipping the first echo, rather than using full exponential or even echo only fits based improved results at short T2 values. However, using an exponential fit with a skipped first echo still comes with substantial errors that have an intricate dependence on T2, flip angle and echo train length, and the two methods showed similar results in
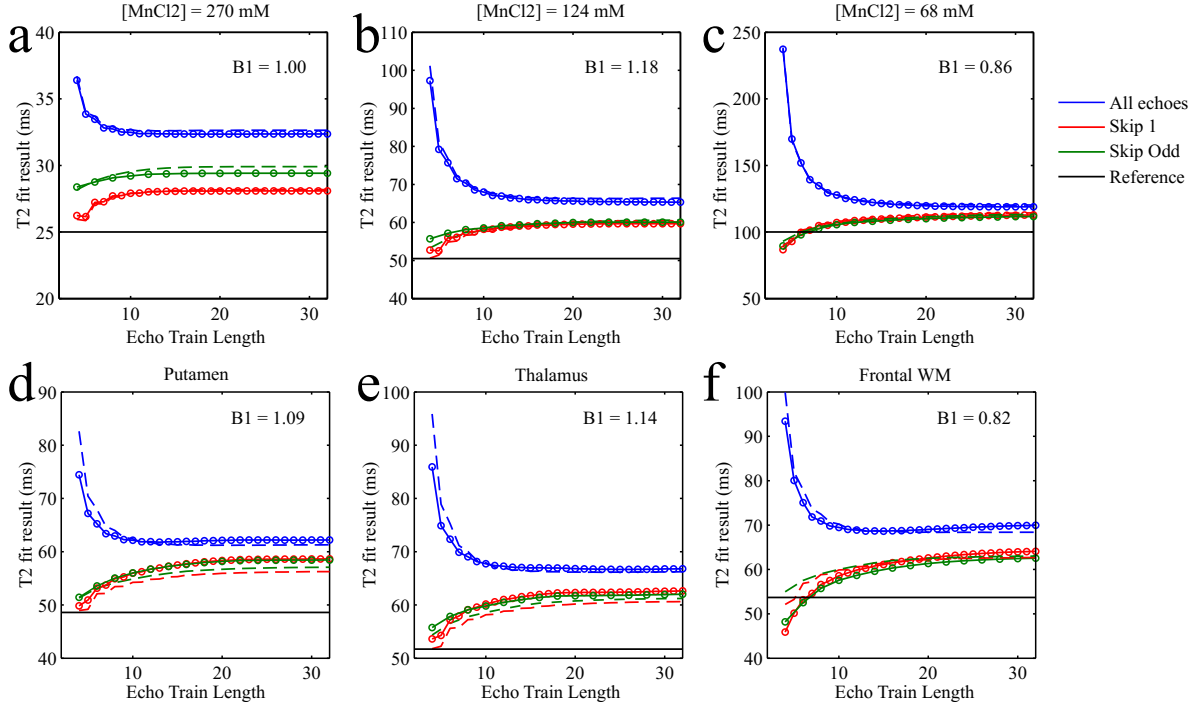
Figure 3.4: Effect of number of echoes on T2 values from experimental phantom (top row) and in vivo brain at 4.7T (bottom row). Exponential fits using all echoes (blue), skipping the first echo (red) or skipping all odd echoes (green) are compared between experiment (circles and solid lines) and simulated data (dashed lines). The reference value is shown in black (computed using ISEC fitting of all echoes for in vivo, and from spin echo in phantom).

vivo, in the ROIs examined for this study.

The main difficulty with skipped echo methods is that discarding the first echo, or all odd echoes, does not eliminate contamination from indirect and stimulated echoes in slice selective 2D experiments. Simulations show that the signal fraction originating from pure spin echo pathways typically diminishes with each echo, and is overtaken by the fraction of signal from alternative echo pathways after only a few echoes. Thus later echoes often carry a greater unwanted echo component. Skipping the first echo eliminates the only point without stimulated echo content, but changes to the unwanted echo content across the echo train still limit exponential fitting. Similarly, even echoes only retains high stimulated echo content. Even though non-selective Carr-Purcell and Carr-Purcell-Meiboom-Gill spin echo sequences refocus effects of imperfect refocusing pulses on alternate (even) echoes [5, 36], with slice selection this is no longer the case.
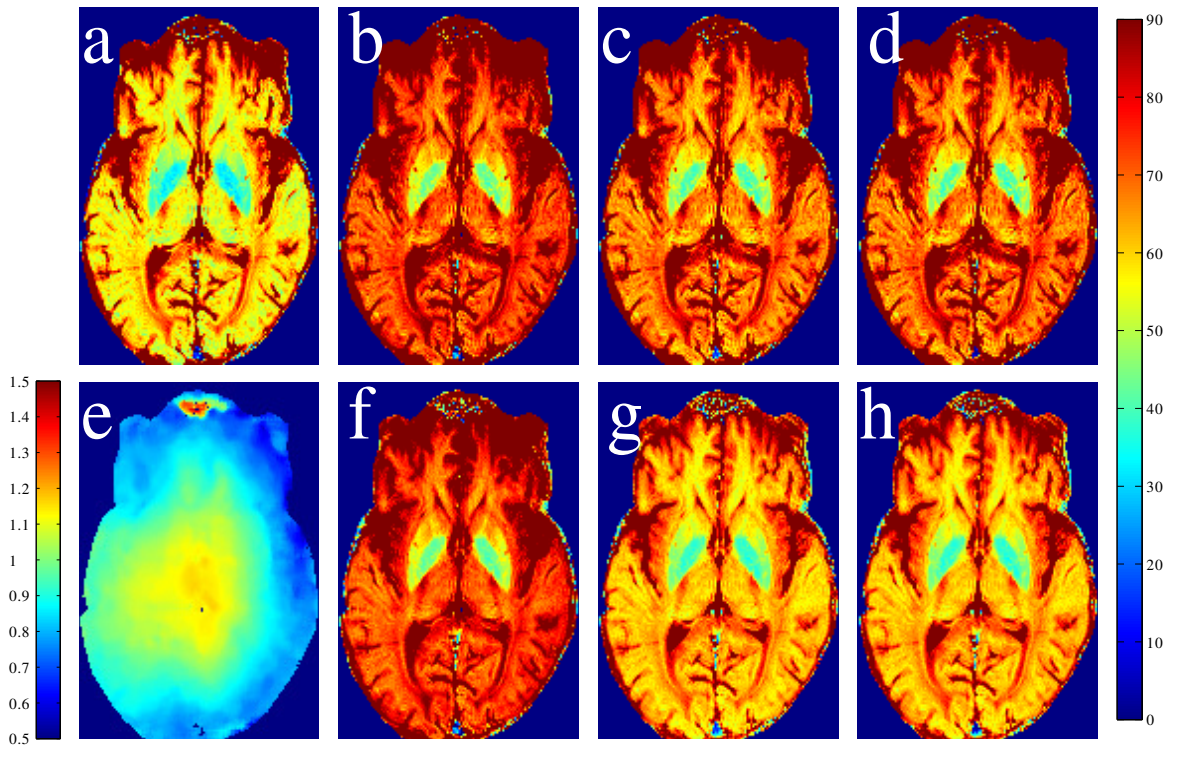
Figure 3.5: T2 maps from 4.7T 32 echo data calculated using (a) ISEC, (b-d) exponential fitting with all echoes (b), even echoes only (c) and skipping first echo only (d). The corresponding B1 map is shown in (e). T2 maps are elongated relative to ISEC results, with all exponential fitting schemes. Exponential fitting is repeated for retrospectively truncated echo trains (ETL 8) in the second row (f) all 8 echoes, (g) skip odd, and (h) skip first only. Results with the reduced ETL are improved for echo skipping methods, but still overestimate T2 relative to ISEC fitting (a).

Our results show that both skipped echo methods result in substantial error in T2. In comparison, it has been previously shown that ISEC fitting methods result in T2 fitting errors of only a few percent over a wide range of T2 and refocussing flip angle values [17].

In terms of T2 studies that compare groups of subjects, if the errors in exponential fitting remain constant, then differences between groups may not be affected. However, our work indicates that the error in skipped echo methods is highly dependent on actual refocussing angle, relative pulse width, as well as T2 and echo train. First, in regard to refocusing flip angle, we recommend use of a rapid flip angle map, to enable an awareness of the flip angles being applied which often vary across and within slices as well as between subjects. Knowledge of the refocusing flip angles enables interpretation of errors from

Table 3.1: Mean T2 (ms) from 32 echo and 8 echo 4.7T experiments for 8 volunteers

Measurement	ETL	Globus Pallidus	Caudate	Putamen	Thalamus	Posterior WM	Frontal WM
Refocusing angle (°)		192.8 ± 10.3	183.6 ± 8.6	181.2 ± 9.6	203.4 ± 11.8	168.4 ± 9.9	160.5 ± 10.0
ISEC	32	34.5 ± 1.7	57.7 ± 1.1	50.0 ± 2.8	51.9 ± 1.9	59.7 ± 4.2	52.3 ± 2.9
Exponential all	32	$46.1 \pm 2.3^{*}$	$72.0 \pm 1.3^{*}$	$63.3 \pm 3.0^{*}$	$67.7 \pm 3.1^{*}$	$74.4 \pm 4.6^{*\dagger}$	$67.2 \pm 2.9^{*}$
Exponential skip 1st	32	$43.4 \pm 2.4^{*\dagger}$	$68.5 \pm 1.4^{*\dagger}$	$59.8 \pm 2.9^{*\dagger\ddagger}$	$63.8 \pm 2.8^{*\dagger\ddagger}$	$72.2 \pm 5.3^{*\dagger\ddagger}$	$62.8 \pm 2.9^{*}$
Exponential even	32	$43.1 \pm 2.1^{*\dagger}$	$67.7 \pm 1.3^{*\dagger}$	$59.2 \pm 3.0^{*\dagger\ddagger}$	$63 \pm 2.6^{*\dagger\ddagger}$	$70.6 \pm 5.3^{*\dagger\ddagger}$	$61.9 \pm 2.7^{*}$
Exponential all	8	$44.4 \pm 2.4^{*\dagger}$	$72.4 \pm 1.3^{*\dagger}$	$63.5 \pm 3.5^{*\dagger}$	$68.4 \pm 4.2^{*\dagger}$	$72.0 \pm 4.1^{*\dagger}$	$67.9 \pm 3.3^{*\dagger}$
Exponential skip 1st	8	$39.1 \pm 1.9^{*\dagger\ddagger}$	$62.6 \pm 1.4^{*\dagger}$	$55.3 \pm 3.1^{*\dagger}$	$58.4 \pm 1.8^{*\dagger}$	$64.1 \pm 4.4^{*\dagger\ddagger}$	$57.3 \pm 2.7d$
Exponential even	8	$39.7 \pm 1.8^{*\dagger\ddagger}$	$62.6 \pm 1.3^{*\dagger}$	$55.3 \pm 3.0^{*\dagger}$	$58.4 \pm 1.7^{*\dagger}$	$63.4 \pm 4.2^{*\dagger\ddagger}$	$57.1 \pm 2.8^{\dagger}$

* indicates significantly different from ISEC
† indicates significantly different from exponential fit of all echoes
‡ indicates skipped echo methods are different from each other

Table 3.2: Mean T2 (ms) from 12 echo 1.5T experiments for six volunteers

Measurement	Globus Pallidus	Caudate	Putamen	Thalamus	Posterior WM	Frontal WM
Refocussing angle	195.4 ± 6.1	186.9 ± 2.9	194.2 ± 4.5	193.4 ± 4.6	184 ± 4.6	183.8 ± 5.3
ISEC	59.4 ± 2.0	81.9 ± 2.1	71.9 ± 2.3	74.6 ± 1.9	81.3 ± 2.0	69.7 ± 1.4
Exponential all	$75.5 \pm 1.7^{*}$	$101.3 \pm 2.5^{*}$	$90.2 \pm 2.4^{*}$	$93.4 \pm 1.9^{*}$	$100.3 \pm 2.5^{*}$	$86.5 \pm 1.8^{*}$
Exponential skip first	$7.00 \pm 1.6^{*\dagger}$	$92.9 \pm 2.3^{*\dagger}$	$83.1 \pm 2.2^{*\dagger}$	$86.5 \pm 1.8^{*\dagger}$	$93.8 \pm 2.2^{*\dagger}$	$80.2 \pm 1.6^{*\dagger}$
Exponential even	$70.1 \pm 2.0^{*\dagger}$	$92.8 \pm 2.4^{*\dagger}$	$83.0 \pm 2.4^{*\dagger}$	$86.4 \pm 1.9^{*\dagger}$	$93.4 \pm 2.1^{*\dagger}$	$80.2 \pm 1.5^{*\dagger}$

* indicates significantly different from ISEC
† indicates significantly different from exponential fit of all echoes

our results provided. Further, as exponential fitting errors are also dependent on the pulse sequence parameters, we recommend against comparison or combination of data from multiple scanners, or where sequence parameters are inconsistent.

Second in regard to the relative pulse width, if the refocusing pulses can be made wide, or, in the extreme, non-selective, excellent results can be obtained with skipped echo exponential methods when flip angles are near 180°. Past work has demonstrated the value of refocusing width greater than three times the excitation width in reducing T2 errors in exponential fitting [37]. However, these errors will also depend on pulse shape, for example the relatively poor Gaussian pulse shape used here at 4.7T to limit RF heating, still produced substantial T2 errors at $3 \times$ width. Of course, wide refocusing width would also pose limitations in cases of contiguous multi-slice 2D acquisition. Third, our results indicate a moderate dependence of the T2 error on the actual T2 value, although this dependence is not as strong as the flip angle and pulse width dependence in the case of the skipped first echo method. Finally, our results also indicate a moderate dependence on echo train number, with reduced echo trains being preferable in some

cases when skipping the first echo, depending on refocussing flip angle. In contrast, we found that full exponential fitting performs increasingly poorly with reduced echoes, which agrees with previous findings [35].

In short, we find that the skipped echo T2 errors have a complicated interplay on all of the parameters considered. Awareness of all of these effects and assignment of optimal parameters is best obtained by examining the graphical results herein. While skipped methods represent a step forward over standard exponential fitting, we recommend fitting for the actual decay curve using modelling that accounts for all echo pathways. Here we used ISEC fitting with full Bloch equation modelling and measured flip angle maps [16, 17, 38], but a more simplified extended phase graph approach is also quite effective [14, 17]. However, not all vendors openly provide detailed pulse sequence information required for modelling of slice selective MESE sequences, such as RF and gradient pulse shapes, amplitudes and timing. In the future, clinical MRI manufacturers could design T2 fitting based on the exact RF pulses used, enabling precise fitting of the actual decay curves using modelling approaches, or could make RF pulse shapes and gradient information for MESE sequences available to the user, so that available algorithms may be implemented [39, 40].

Limitations of this work include the use of only one inter-echo spacing at each field strength. However, the results may be scaled for any inter-echo spacing by considering the ratio of inter-echo spacing to T2. Also we did not consider variable inter-echo spacing within the echo train since this is less commonly used. Errors in exponential T2 fitting depend on the amount of spurious echoes, and therefore on the specific RF pulse shapes and flip angles, making results specific to the pulse sequence under study. We assumed a uniform T1 for both ISEC fitting, and for simulated experiments. In cases with a large T1/T2 value (>10), this assumption will result in only very small errors in ISEC fitting [14, 17]. Due to a range of T1 values in tissues, differences in T2 values between models may not be exactly as simulation results presented, particularly in echo amplitudes with large contributions from stimulated echoes, though these differences are expected to be small in comparison to differences in T2 values due to fitting model. Lastly this work used mono-exponential fitting which is not ideal for multi-component territories, such as

77

white matter, which also contains a rapidly decaying short T2 component of myelin water [18]. However, multiple component fitting requires much more rigorous experimental conditions than single component fitting, particularly in regard to number of echoes and SNR.

3.5   Conclusions

Skipped echo exponential fitting schemes can make substantial improvements in T2 accuracy over all echoes exponential fitting, particularly when a short echo train number is used. However, skipped echo exponential fitting is insufficient for avoiding stimulated echo contamination in multi-echo spin echo T2 fitting. Both skipped echo approaches yielded a highly variable error that is flip angle, T2 and echo train length dependent. Errors are highest when refocusing angle deviates from 180°.

Acknowledgements

References

[1] Ishu Arpan, Sean C. Forbes, Donovan J. Lott, Claudia R. Senesac, Michael J. Daniels, William T. Triplett, Jasjit K. Deol, H. Lee Sweeney, Glenn A. Walter, and Krista Vandenborne. T2 mapping provides multiple approaches for the characterization of muscle involvement in neuromuscular diseases: a cross-sectional study of lower leg muscles in 515-year-old boys with Duchenne muscular dystrophy. *NMR in Biomedicine*, 26(3):320–328, March 2013.

[2] Timothy J. Mosher, Yi Liu, and Collin M. Torok. Functional Cartilage MRI T2 Mapping: Evaluating the Effect of Age and Training on Knee Cartilage Response to Running. *Osteoarthritis and cartilage / OARS, Osteoarthritis Research Society*, 18(3):358–364, March 2010. 00060.

[3] Shoichiro Takao, Tan B. Nguyen, Hon J. Yu, Shigeo Hagiwara, Yasuhito Kaneko, Taiki Nozaki, Seiji Iwamoto, Maki Otomo, Ran Schwarzkopf, and Hiroshi Yoshioka. T1rho and T2 relaxation times of the normal adult knee meniscus at 3t: analysis of zonal differences. *BMC Musculoskeletal Disorders*, 18, May 2017.

[4] L Yao, A Gentili, and A Thomas. Incidental magnetization transfer contrast in fast spin-echo imaging of cartilage. *Journal of magnetic resonance imaging: JMRI*, 6(1):180–184, February 1996.

[5] Daniel Kim, Jens H. Jensen, Ed X. Wu, Sujit S. Sheth, and Gary M. Brittenham. Breathhold multiecho fast spin-echo pulse sequence for accurate R2 measurement in the heart and liver. *Magnetic Resonance in Medicine*, 62(2):300–306, August 2009.

[6] Haiying Tang, Jens H. Jensen, Christina L. Sammet, Sujit Sheth, Srirama V. Swaminathan, Kristi Hultman, Daniel Kim, Ed X. Wu, Truman R. Brown, and Gary M. Brittenham. MR characterization of hepatic storage iron in transfusional iron overload. *Journal of Magnetic Resonance Imaging*, 39(2):307–316, February 2014.

[7] Bettina Baeßler, Frank Schaarschmidt, Christian Stehning, Bernhard Schnackenburg, Agathe Giolda, David Maintz, and Alexander C. Bunck. Reproducibility of three different cardiac T2-mapping sequences at 1.5t. *Journal of Magnetic Resonance Imaging*, 44(5):1168–1178, November 2016.

[8] Sean C.L. Deoni. Quantitative Relaxometry of the Brain. *Topics in magnetic resonance imaging : TMRI*, 21(2):101–113, April 2010.

[9] A.L. MacKay, I.M. Vavasour, A. Rauscher, S.H. Kolind, B. M adler, G.R.W. Moore, A.L. Traboulsee, D.K.B. Li, and C. Laule. MR Relaxation in Multiple Sclerosis. *Neuroimaging Clinics of North America*, 19(1):1–26, February 2009.

[10] Fumiyuki Mitsumori, Hidehiro Watanabe, Nobuhiro Takaya, Michael Garwood, Edward J. Auerbach, Shalom Michaeli, and Silvia Mangia. Toward understanding transverse relaxation in human brain through its field dependence. *Magnetic Resonance in Medicine*, 68(3):947–953, 2012.

[11] A. P. Crawley and R. M. Henkelman. Errors in T2 estimation using multislice multiple-echo imaging. *Magnetic Resonance in Medicine*, 4(1):34–47, January 1987.

[12] J.T. Vaughan, M. Garwood, C.m. Collins, W. Liu, L. DelaBarre, G. Adriany, P. Andersen, H. Merkle, R. Goebel, M.b. Smith, and K. Ugurbil. 7t vs. 4t: RF power, homogeneity, and signal-to-noise comparison in head images. *Magnetic Resonance in Medicine*, 46(1):24–30, July 2001.

[13] Jürgen Hennig. Echoes - how to generate, recognize, use or avoid them in MR-imaging sequences. Part I: Fundamental and not so fundamental properties of spin echoes. *Concepts in Magnetic Resonance*, 3(3):125–143, 1991.

[14] R. Marc Lebel and Alan H. Wilman. Transverse relaxometry with stimulated echo compensation. *Magnetic Resonance in Medicine*, 64(4):1005–1014, 2010.

[15] S. Majumdar, S. C. Orphanoudakis, A. Gmitro, M. O'Donnell, and J. C. Gore. Errors in the measurements of T2 using multiple-echo MRI techniques. II. Effects

of static field inhomogeneity. *Magnetic Resonance in Medicine: Official Journal of the Society of Magnetic Resonance in Medicine / Society of Magnetic Resonance in Medicine*, 3(4):562–574, August 1986.

[16] Noam Ben-Eliezer, Daniel K. Sodickson, and Kai Tobias Block. Rapid and accurate T $_2$ mapping from multi-spin-echo data using Bloch-simulation-based reconstruction: Mapping Using Bloch-Simulation-Based Reconstruction. *Magnetic Resonance in Medicine*, 73(2):809–817, 2015.

[17] Kelly C. McPhee and Alan H. Wilman. Transverse relaxation and flip angle mapping: Evaluation of simultaneous and independent methods using multiple spin echoes. *Magnetic Resonance in Medicine*, 77(5):2057–2065, May 2017.

[18] Thomas Prasloski, Burkhard M adler, Qing-San Xiang, Alex MacKay, and Craig Jones. Applications of stimulated echo correction to multicomponent T2 analysis. *Magnetic Resonance in Medicine*, 67(6):1803–1814, 2012.

[19] Mehdi Behroozi, Caroline Chwiesko, Felix Str ockens, Magdalena Sauvage, Xavier Helluy, Jutta Peterburs, and Onur G unt urk un. In vivo measurement of T1 and T2 relaxation times in awake pigeon and rat brains at 7t. *Magnetic Resonance in Medicine*, page In Press, May 2017.

[20] Christian Langkammer, Nikolaus Krebs, Walter Goessler, Eva Scheurer, Franz Ebner, Kathrin Yen, Franz Fazekas, and Stefan Ropele. Quantitative MR Imaging of Brain Iron: A Postmortem Validation Study. *Radiology*, 257(2):455–462, November 2010. 00088.

[21] Serguei Liachenko and Jaivijay Ramu. Quantification and reproducibility assessment of the regional brain T2 relaxation in nave rats at 7t. *Journal of Magnetic Resonance Imaging*, 45(3):700–709, March 2017.

[22] Luca Biasiolli, Alistair C Lindsay, Joshua T Chai, Robin P Choudhury, and Matthew D Robson. In-vivo quantitative T2 mapping of carotid arteries in

atherosclerotic patients: segmentation and T2 measurement of plaque components. *Journal of Cardiovascular Magnetic Resonance*, 15(1):69, August 2013.

[23] Marion de Roquefeuil, Pierre-André Vuissoz, Jean-Marie Escanyé, and Jacques Felblinger. Effect of physiological Heart Rate variability on quantitative T2 measurement with ECG-gated Fast Spin Echo (FSE) sequence and its retrospective correction. *Magnetic Resonance Imaging*, 31(9):1559–1566, November 2013.

[24] Vít Herynek, Dita Wagnerová, Irena Hejlová, Monika Dezortov, and Milan Hájek. Changes in the brain during long-term follow-up after liver transplantation. *Journal of Magnetic Resonance Imaging*, 35(6):1332–1337, June 2012.

[25] Michael J. Knight, Bryony McCann, Demitra Tsivos, Elizabeth Couthard, and Risto A. Kauppinen. Quantitative T1 and T2 MRI signal characteristics in the human brain: different patterns of MR contrasts in normal ageing. *Magnetic Resonance Materials in Physics, Biology and Medicine*, 29(6):833–842, December 2016.

[26] Tarja L onnfors-Weitzel, Thilo Weitzel, Johannes Slotboom, Claus Kiefer, Claudio Pollo, Michael Sch upbach, Markus Oertel, Alain Kaelin, and Roland Wiest. T2-relaxometry predicts outcome of DBS in idiopathic Parkinson's disease. *NeuroImage : Clinical*, 12:832–837, September 2016. 00000.

[27] Takashi Nishii, Toshiyuki Shiomi, Hisashi Tanaka, Youichi Yamazaki, Kenya Murase, and Nobuhiko Sugano. Loaded Cartilage T2 Mapping in Patients with Hip Dysplasia. *Radiology*, 256(3):955–965, September 2010.

[28] J. Sedlacik, K. Boelmans, U. L obel, B. Holst, S. Siemonsen, and J. Fiehler. Reversible, irreversible and effective transverse relaxation rates in normal aging brain at 3 T. *NeuroImage*, 84:1032–1041, January 2014.

[29] Tilman J. Sumpf, Martin Uecker, Susann Boretius, and Jens Frahm. Model-based nonlinear inverse reconstruction for T2 mapping using highly undersampled spin-echo MRI. *Journal of Magnetic Resonance Imaging*, 34(2):420–428, August 2011. 00057.

[30] D. Wagnerová, V. Herynek, M. Dezortová, P. Marusič, P. Krek, J. Zámečník, F. Jírøu, A. Škoch, and M. Hájek. The relationships between quantitative MR parameters in hippocampus in healthy subjects and patients with temporal lobe epilepsy. *Physiological Research*, 64(3):407–417, 2015.

[31] N. K. Focke, G. Helms, P. M. Pantel, S. Scheewe, M. Knauth, C. G. Bachmann, J. Ebentheuer, P. Dechent, W. Paulus, and C. Trenkwalder. Differentiation of Typical and Atypical Parkinson Syndromes by Quantitative MR Imaging. *American Journal of Neuroradiology*, 32(11):2087–2092, December 2011.

[32] J. Pauly, P. Le Roux, Dwight Nishimura, and A. Macovski. Parameter relations for the Shinnar-Le Roux selective excitation pulse design algorithm [NMR imaging]. *IEEE Transactions on Medical Imaging*, 10(1):53–65, 1991.

[33] Rudolf Stollberger and Paul Wach. Imaging of the active B1 field in vivo. *Magnetic Resonance in Medicine*, 35(2):246–251, 1996.

[34] Mustapha Bouhrara and Jean-Marie Bonny. B1 mapping with selective pulses. *Magnetic Resonance in Medicine*, 68(5):1472–1480, November 2012.

[35] Md. Nasir Uddin, R. Marc Lebel, and Alan H. Wilman. Transverse relaxometry with reduced echo train lengths via stimulated echo compensation. *Magnetic Resonance in Medicine*, 70(5):1340–1346, 2013.

[36] Donald W. McRobbie, Elizabeth A. Moore, Martin J. Graves, and Martin R. Prince. *MRI from Picture to Proton*. Cambridge University Press, September 2006. 00412.

[37] Gaby S. Pell, Regula S. Briellmann, Anthony B. Waites, David F. Abbott, David P. Lewis, and Graeme D. Jackson. Optimized clinical T2 relaxometry with a standard CPMG sequence. *Journal of Magnetic Resonance Imaging*, 23(2):248–252, 2006. 00058.

[38] Kelly C. McPhee and Alan H. Wilman. T2 quantification from only proton density and T2-weighted MRI by modelling actual refocusing angles. *NeuroImage*, 118:642–650, September 2015.

[39] Noam Ben-Eliezer. EMC Based T2-Mapping Package | CAI2r. http://cai2r.net/resources/software/emc-based-t2-mapping-package, 2015. Accessed 2017-09-28.

[40] R Marc Lebel. StimFit: A toolbox for robust T2 mapping with stimulated echo compensation. In *Proceedings of the Meeting of the International Society for Magnetic Resonance in Medicine*, page 2558, Melbourne, Australia, 2012.

Chapter 4

T2 Quantification from Only Proton Density and T2-Weighted MRI by Modelling Actual Refocusing Angles[1]

Proton density and transverse relaxation (T2)-weighted fast spin echo images are frequently acquired. T2 quantification is commonly performed by applying an exponential fit to these two images, despite recent evidence that an exponential fit is insufficient to correctly quantify T2 in the presence of imperfect RF refocusing due to standard 2D slice selection or use of reduced refocusing angles. Here we examine the feasibility of accurate two echo fitting using standard proton density and T2-weighted images by utilizing Bloch equation simulations and prior knowledge of refocusing angles. This method is demonstrated in simulation, phantom, and human brain experiments, in comparison to the exponential approach, and to a 32 echo multiple-echo spin echo approach. Comparison to single spin echo is also performed in phantom experiments. The two echo method, which compensates for indirect and stimulated echoes, enables accurate quantitative T2 over a wide range of flip

angle and T2 values using standard MRI methods, provided there is adequate SNR and flip angle knowledge.

4.1 Introduction

Quantification of transverse relaxation time (T2) has been used to probe tissues in the brain [1–6] and body [7–12] yielding information related to tissue properties such as water, macromolecular, or iron content. The quantitative nature of T2 improves comparisons between subjects or within subjects over time by removing signal variations found in T2-weighted images, such as those dependent on receiver gain or flip angle variation. Multiple-echo spin echo (MESE) techniques are the standard method of measuring T2, however, acquisition of full MESE data sets is not always feasible due to time constraints.

Proton density (PD) and T2-weighted Fast Spin Echo (FSE) (often referred to as TURBO spin echo, or RARE) [13] are frequently performed in clinical research studies, and T2-weighted FSE is typically included in most clinical brain exams. The resulting weighted images provide useful image contrast, however additional value could be obtained by quantifying T2. Many studies have used PD and T2-weighted images to estimate T2 using a simple exponential fit [14–21]. However, imperfect refocusing due to slice profiles, RF interference or purposeful reduction in refocusing angles all result in stimulated or indirect echoes, which contaminate the exponential T2 decay [22–25], and compromise exponential T2 fitting.

Using exponential fitting, differences between T2 values obtained from MESE experiments and pairs (or sets) of FSE images have been previously noted [26, 27]. In addition, inter-site studies have noted systematic differences between sites and vendors in T2 maps calculated from exponential fitting of pairs of PD and T2-weighted images [16]. Exponential fitting does not take into account key differences in RF pulse sequence parameters (pulse shape, relative refocusing width, refocusing angle, spoiling) between various scanners/vendors, which affect the degree of stimulated and indirect echo contamination. Further, a two point fitting approach is expected to be more sensitive to pulse sequence specific errors than a multi-echo approach, since less data is being used which

precludes averaging of errors across multiple time points. These errors include varying stimulated and indirect echo contributions, as well as signal-to-noise (SNR) effects, which all complicate the accurate fitting of T2 using only two echoes.

The goal of this work is to demonstrate that a PD and a T2-weighted image may be used to accurately determine the T2 through advanced fitting of the typically non-exponential decay. Direct fitting of the spin response for T2 quantification is an area of active research using methods such as stimulated echo compensation with echo phase graph [25, 28–32], or full Bloch modelling [33]. These methods rely on multiple echoes to obtain satisfactory fitting conditions for three fitting parameters (T2, flip angle, initial signal amplitude), which requires multiple echoes (in practice, at least four [32], but typically many more). Here, we examine the case of only two echoes (PD and T2-weighted) using simulation, phantom and human brain experiments. Unlike the original implementation of stimulated echo compensation (Lebel and Wilman, 2010) which used Fourier transform approximation of slice profile and multiple echoes, the two point method introduced here requires precise modelling of RF pulse response and prior knowledge of the refocusing flip angles.

4.2   Methods

A Bloch equation model was used to determine T2 from only a PD-weighted and a T2-weighted FSE image and prior flip angle knowledge, which was achieved with a flip angle map. Modelling of the spin response accounts for all echo pathways, providing Indirect and Stimulated Echo Compensation (ISEC). Using both simulations and human brain experiments, this two echo ISEC method was tested using a range of echo times against exponential fitting, and compared to a standard MESE approach using 32 echoes with ISEC T2 fitting. Additionally, two point fitting was investigated using the second echo, instead of the first PD-weighted echo, and a later echo.

4.2.1   T2 Fitting Model

Simulations of slice-selective T2 signal amplitudes (both MESE and FSE) were performed using the Shinnar-Le Roux (SLR) algorithm [34] to simulate RF pulses, and solutions to the Bloch equations to simulate relaxation, similar to [33]. All simulations and image processing were performed using custom in-house MATLAB (R2014a, 64 bit) programs. In order to model slice selection, magnetization vectors were calculated at 1001 points equally spaced over twice the excitation width in the slice-select direction. RF pulses were modelled using 1024 points equally spaced over the duration of the pulse. RF pulse profiles, flip angles, gradients and timing were simulated according to their respective pulse sequence parameters.

Slice selective MESE and FSE data were fitted for T2 and amplitude via minimization of the sum squared difference between experimental and simulated data. Flip angle maps were separately measured and provided to the fitting algorithm. A dictionary of decay curves with many T2 and flip angle values was created prior to fitting (similar to [35] and [33]). Voxel-wise fitting was performed using a subset of curves from the dictionary with excitation and refocusing flip angles which correspond to the measured value at that voxel. The dictionary of curves was specific to the parameters used to acquire the data (RF pulse shapes and timing, gradient amplitudes, crusher gradients, and echo spacing).

To create a dictionary of curves for T2 fitting, simulations were repeated for a range of T2 (10 - 1000 ms at 0.1 ms resolution up to 150 ms, 1 ms resolution from 150 - 200 ms, 2 ms resolution from 200 - 300 ms, 5 ms resolution from 300 - 500 ms, and 10 ms resolution from 500 - 1000 ms), and normalized flip angle values (0.20 - 1.80 at 0.005 resolution, resulting in refocusing angles from 36 - 324°), and an assumed T1 of 2 s. The dictionary contained a total of over 510 000 curves, allowing for precise fitting. The range of T1 values at 4.7 T is expected to typically be 1.0 - 2.0 s [36–38] in most brain tissue. The impact of T1 choice is examined.

4.2.2 Flip Angle Mapping With Slice Profile Correction

Flip angle maps were computed using a double angle method [39], accounting for slice profile effects. Correction for slice profile is necessary to avoid errors in the flip angle map [40]. Two FSE images were acquired with nominal excitation angles of 60° and 120°, both with the same refocusing train, effective TE 43 ms, TR 7 s, echo train length 24, and echo spacing 10.75 ms. RF pulse shapes, slice thickness, field of view, and matrix size were matched to the corresponding T2 mapping sequence. SLR simulations of the FSE imaging sequence for nominal excitation angles of 60° and 120°, and for many RF amplitude values, were performed. The relationship between RF amplitude, and the ratio of signal magnitudes from the two images, S(120°)/S(60°) was fitted with a ninth degree polynomial, which was used to rapidly generate a corrected flip angle map from acquired data. Resulting flip angle maps are median filtered with a 5×5 pixel filter before input into the T2 fitting algorithm.

Flip angle map values are expressed as a normalized parameter. We define the normalized flip angle map values, nB1, according to: $\alpha = \text{nB1} \cdot \alpha_{\text{nom}}$, where α is the flip angle achieved at the centre of the selected slice, α_{nom} is the prescribed nominal flip angle, and nB1 is the scaling factor relating the two angles.

4.2.3 In Vivo Experiments

Axial single-slice two dimensional MESE and FSE images of the human brain were acquired in six healthy volunteers (aged 29±6 years) through iron-rich deep grey matter on a 4.7 T (Varian Inova) MRI system. All subjects provided written, informed consent and this investigation was approved by the local institutional ethics board. MESE sequences were acquired with TR 4 s, TE 10 - 320 ms, constant echo spacing 10 ms, echo train length 32, excitation and refocusing pulse durations 4 ms and 1.6 ms, excitation width 4 or 5 mm, refocusing width 1.75 × excitation width, Gaussian pulse shapes (time-bandwidth product 2.69; 5 sigma width), matrix 256 x 145 x 1; voxel size = 1 x 1.25 x 4 mm^3. Eight FSE images were acquired with effective TE (10, 20, 30, 40, 50, 60, 70, or 80 ms), prescribed excitation 90°, refocusing 180°, with RF pulses and timing, TR, and

resolution matched to the multi-echo experiment. FSE images for flip angle mapping were acquired with resolution, and pulse shapes matched to MESE data.

T2 maps were computed using the ISEC model described in section 4.2.1, using the independently measured flip angle map, and various sequence and echo combinations to determine optimal parameters. Fitting was performed with the full 32 echo MESE data set, all eight FSE images, and various pairs of FSE images. FSE pairs made use of the first or second echo (effective TE = 10 or 20 ms), paired with later T2-weighted echoes (effective TE = 40 ms to 80 ms, with constant 10 ms echo spacing). For comparison, data were also fitted with an exponential model.

Regions-of-interest (ROIs) were drawn selecting six bilateral grey matter regions (putamen, globus pallidus, head of the caudate nucleus, thalamus, cortical grey matter, and insular cortex) and two bilateral white matter regions (frontal and posterior white matter). Mean ROI T2 values were reported, with bilateral ROIs combined.

4.2.4 Phantom Validation

In order to validate the ISEC method, phantom measurements were performed with comparison to a single spin echo, which exhibits no stimulated echoes due to its use of only 1 refocusing pulse. Six solutions with $MnCl_2$ concentrations ranging from 28-512 mM were placed in 28 mm diameter (55 mL) cylindrical plastic laboratory tubes. T1 and T2 were measured with inversion recovery, and single spin echo experiments. Ten single spin echo experiments were performed (TE = 13.1, 20, 30, 40, 50, 60, 70, 80, 130, 200 ms, TR 14 s, nominal excitation 90°; nominal refocusing 180°; sinc pulse shapes). T2 maps were computed from this single spin echo data using an exponential fit. T1 values were estimated with an inversion recovery experiment (Inversion times = 14, 20, 50, 100, 200, 300, 500, 1000, 2000, 3000, 4000 ms; FSE readout; 8 mm slice thickness; TR 12 s; TE 8.5 ms; matrix 192 x 256; FOV 26 x 20 cm).

MESE, eight FSE images, and a nB1 map were also acquired in the same scanning session, with parameters matched to in vivo experiments, with the following exceptions: 8 mm slice thickness for all experiments, and TR = 14 s for nB1 mapping. T2 maps using both exponential and ISEC fits were computed from MESE data, and from different

90

combinations of pairs of FSE images. Results were compared to single spin echo T2 fits.

4.2.5 Numerical Validation: Uncertainty Due to Noise

In order to determine the optimal pair of effective echoes in simulation, SNR analysis was performed. The coefficient of variation in resulting T2 fit values for 500 samples with simulated SNR of 50 for a range of T2 values (20 - 100 ms), nB1 values (0.5 - 1.5, i.e. refocusing angles from 90° - 270°), and various choices of echo combinations was computed. Analysis was repeated for a range of SNR values (3 - 300), for T2 = 50 ms and nB1 = 1.0 (corresponding to a refocusing angle of 180°), with 1000 samples at each SNR. Here, SNR is defined as simulated signal magnitude in the first echo relative to standard deviation of the noise. Random Gaussian complex noise was added to complex simulated decay curves, with fitting performed on the resulting simulated noisy magnitude data. Maps of the uncertainty in resulting T2 fits (coefficient of variation, in percent) were computed for various combinations of echoes. For all simulations, pulse shapes, gradients, and timing were matched to human experimental parameters.

4.2.6 Numerical Validation: Assumption of Uniform T1

To validate, and to assess error in the two point ISEC fitting with respect to the constant T1 assumption, simulated T2 decay curves with T1 = 1.0 s were fitted with a dictionary which used a T1 of 2 or 3 s. A range of simulated data was used with various combinations of echo times (constant echo spacing of 10 ms), T2 values (10 - 150 ms) and nB1 (0.5 - 1.5, corresponding to refocusing angles of 90 - 270°). Errors from exponential fit results were also examined.

To further explore the repercussions of an assumption of a uniform T1 value, decay curves were simulated with a range of T1 values (300 - 3000 ms) and were fitted using the two point ISEC method, assuming T1 = 2 s, as was assumed for in vivo experiments. Errors were examined for a range of T2 (25 - 300 ms) and nB1 (0.33 - 1.5, corresponding to 60 - 270° refocusing angles) values. Fitting was performed using the two point ISEC method with echoes 1 and 7 (effective TE 10, 70 ms), echoes 2 and 6 (effective TE 20,

60 ms), and again for the 32 echo MESE method (TE = 10, 20,... 320 ms).

4.3 Results

The goal of this work is clarified in Figure 4.1, whereby a PD and a T2-weighted image are used to determine T2 through advanced fitting of the typically non-exponential decay. The echo contamination is clearly evident in the non-exponential multiple-echo decay, beginning with an enhanced second echo. However, the acquisition of only a PD and a T2-weighted image, do not provide visible evidence of the contaminating echo signals. Thus two echoes may be fit with an exponential with minimal fitting errors, but producing an incorrect result.
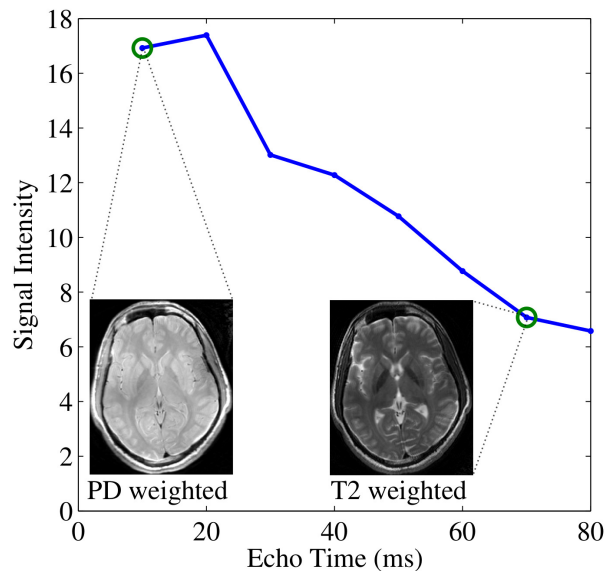
Figure 4.1: T2 decay is non-exponential. An example decay curve (data point chosen from the caudate head; T2 = 60.5 ms, measured refocusing angle = 168°), is shown with the corresponding PD and T2-weighted images.

4.3.1 In Vivo T2 Mapping

T2 values computed using the two point ISEC averaged over six healthy volunteers are reported in Table 4.1 for various possible echo combinations. T2 values derived from FSE values are reported as relative percent to ISEC fit of MESE data. The refocusing

angle, α_R, within each region is also reported, as derived from the flip angle maps. The use of first and seventh echo (TE = 10 and 70 ms) produce the best two-echo results with ISEC fitting. Corresponding T2 values from the same regions, but derived from exponential fitting are reported in Table 4.2. In exponential fitting, use of the first echo (PD-weighted) image gives very poor results, but better results are achieved using the second echo combined with a later echo.

Example T2 maps from sequences using nominal 180° refocusing pulses and the corresponding normalized B1 map are shown in Figure 4.2. The T2 map computed using ISEC and the 32 echo MESE data set (a) or FSE images (b, c) makes use of the independently measured flip angle map (d). T2 maps computed using an exponential fit are shown below (e, f). The T2 maps shown used fits from the optimal FSE pair for ISEC (TE 10 and 70 ms) and for exponential (TE 20 and 60 ms), as determined from Tables 4.1 and 4.2.

Table 4.1: Group averaged T2 values using ISEC fitting[a],[b]

	Thalamus	Globus Pallidus	Caudate Head	Putamen	Insular Cortex	Cortical GM	Posterior WM	Frontal WM
MESE (ms)	52.3±3.3	34.3±2.2	57.9±2.1	51.1±3.4	72.6±3.0	55.4±4.4	59.7±6.5	52.4±3.1
nB1	1.13±0.02	1.09±0.06	1.04±0.06	1.03±0.05	0.99±0.04	0.87±0.06	0.92±0.05	0.86±0.07
α_R	203.6°±4.4°	196.6°±10.3°	186.6°±10.0°	186.0°±9.0°	178.3°±6.4°	157.4°±10.1°	166.2°±9.3°	154.9°±13.5°
FSE Data Set	Percentage T2 fit accuracy (relative to gold standard MESE, %)							
Echo 1-8 (TE 10 - 80 ms)	94±3	99±6	98±6	98±8	97±5	96±5	96±5	96±5
Echo 1, 3 (TE 10, 30 ms)	90±2	96±8	96±8	95±9	89±1	91±11	87±2	105±19
Echo 1, 4 (TE 10, 40 ms)	90±2	95±9	95±9	95±10	89±3	92±8	89±6	95±9
Echo 1, 5 (TE 10, 50 ms)	97±5	101±8	99±8	100±10	95±3	95±8	95±4	102±11
Echo 1, 6 (TE 10, 60 ms)	92±2	97±7	94±5	96±9	91±6	94±8	92±5	95±7
Echo 1, 7 (TE 10, 70 ms)	97±4	104±7	100±8	100±10	98±6	98±6	98±5	100±7
Echo 1, 8 (TE 10, 80 ms)	94±4	97±6	98±7	97±8	100±5	95±8	95±5	96±7
Echo 2, 4 (TE 20, 40 ms)	88±3	94±8	93±5	92±8	90±4	94±3	91±9	83±5
Echo 2, 5 (TE 20, 50 ms)	99±8	102±7	99±6	98±8	98±3	97±5	98±6	95±5
Echo 2, 6 (TE 20, 60 ms)	91±3	97±8	93±4	95±8	92±6	95±4	94±7	89±4
Echo 2, 7 (TE 20, 70 ms)	98±5	104±7	100±6	99±9	100±6	100±5	100±6	96±4
Echo 2, 8 (TE 20, 80 ms)	94±5	97±7	97±6	96±7	102±6	96±6	97±6	92±4

[a] Gold standard T2 fit values from ISEC fitting of MESE data are reported as mean (ms) ± standard deviation within the group. All other T2 values are expressed as the relative value compared to the gold standard (%).
[b] n = 6 subjects, aged 29.0 ± 6.2 years

4.3.2 Phantom Validation

T2 fit results from single spin echo measurements, and from ISEC and exponential fitting of MESE and pairs of FSE images are reported in Table 4.3. T1 values from inversion recovery are also reported. Phantom results show excellent agreement between ISEC
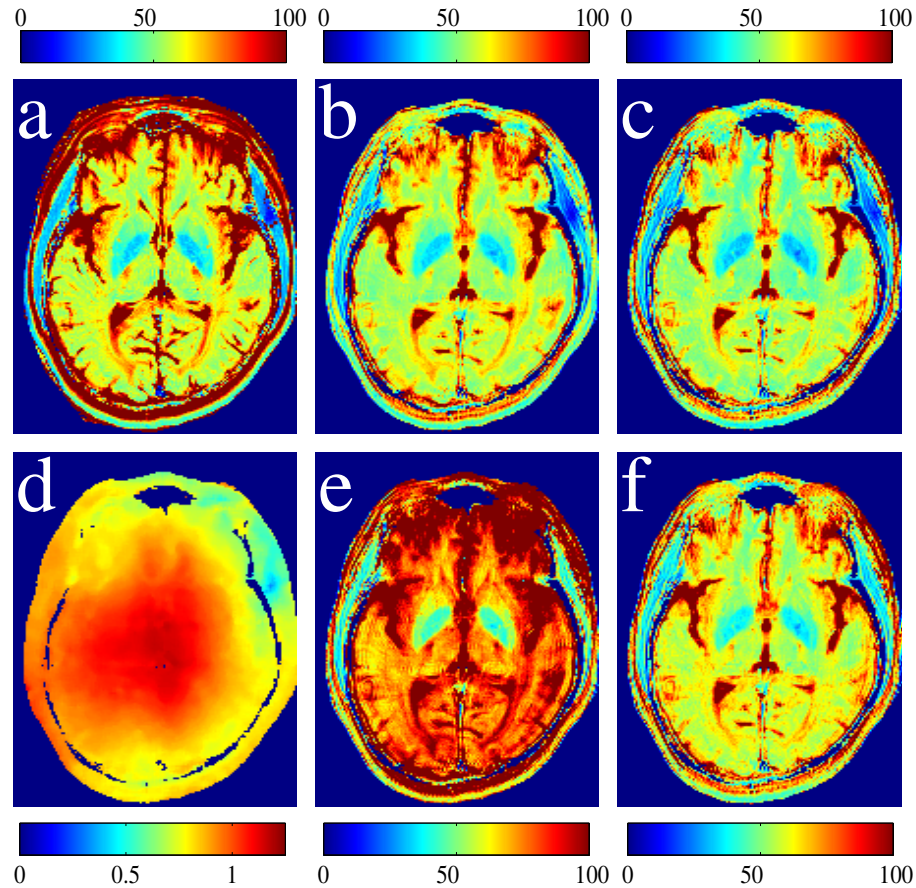
Figure 4.2: Comparing T2 maps from ISEC and exponential fit. T2 maps (ms) computed using ISEC: (a) 32 echo MESE experiment, (b) two FSE images TE = 10 and 70 ms, (c) TE = 20 and 60 ms. Exponential T2 fitting with two FSE images (e) TE = 10 and 70 ms, (f) TE = 20 and 60 ms. (d) Independently measured nB1 map used for fits a-c. All FSE and MESE data shown were acquired with a nominal 180° refocusing pulse and 10 ms echo spacing.

methods and single spin echo results across a wide range of T2 values. Exponential fits of FSE and MESE data overestimate T2 results in most cases.

4.3.3   Numerical Assessment of T2 fitting

Uncertainty in the T2 measurement is examined in Fig. 4.3 by mapping the coefficient of variance in T2 fitting results from 500 simulated data sets using an SNR of 50. Results are shown for various combinations of echo pairs, for a range of T2 (20 - 100 ms) and nB1 values (0.5 - 1.5, resulting in a refocusing angle of 90° - 270°). SNR simulations show that for experiments where T2 is expected in that range, the optimal TE pair is 10 ms

Table 4.2: Group averaged T2 values using exponential fit[a],[b]

	Thalamus	Globus Pallidus	Caudate Head	Putamen	Insular Cortex	Cortical GM	Posterior WM	Frontal WM
MESE, ISEC fit (ms)	52.3±3.3	34.3±2.2	57.9±2.1	51.1±3.4	72.6±3.0	55.4±4.4	59.7±6.5	52.4±3.1
nB1	1.13±0.02	1.09±0.06	1.04±0.06	1.03±0.05	0.99±0.04	0.87±0.06	0.92±0.05	0.86±0.07
α_R	203.6°±4.4°	196.6°±10.3°	186.6°±10.0°	186.0°±9.0°	178.3°±6.4°	157.4°±10.1°	166.2°±9.3°	154.9°±13.5°
FSE Data Set	Percentage T2 fit accuracy (relative to gold standard MESE, %)							
Echo 1-8 (TE 10 - 80 ms)	128±3	134±6	128±6	128±7	128±5	128±4	125±6	129±4
Echo 1, 3 (TE 10, 30 ms)	189±9	159±13	200±13	177±12	212±7	185±12	167±10	356±66
Echo 1, 4 (TE 10, 40 ms)	175±5	160±10	179±12	169±11	184±9	177±10	165±18	189±13
Echo 1, 5 (TE 10, 50 ms)	148±6	140±8	148±10	143±10	151±4	143±9	142±11	158±10
Echo 1, 6 (TE 10, 60 ms)	143±4	142±9	142±8	141±9	143±8	143±7	138±10	148±8
Echo 1, 7 (TE 10, 70 ms)	136±4	136±8	137±9	133±10	139±7	135±5	133±9	140±6
Echo 1, 8 (TE 10, 80 ms)	135±4	137±8	137±8	134±8	145±7	135±6	133±8	139±6
Echo 2, 4 (TE 20, 40 ms)	94±2	105±7	97±4	97±7	91±4	97±3	94±8	88±4
Echo 2, 5 (TE 20, 50 ms)	97±7	104±7	97±6	97±8	93±3	95±4	96±6	93±5
Echo 2, 6 (TE 20, 60 ms)	103±3	113±8	102±5	105±7	98±6	104±3	102±6	99±4
Echo 2, 7 (TE 20, 70 ms)	104±4	112±7	105±6	105±8	102±5	104±5	104±5	101±3
Echo 2, 8 (TE 20, 80 ms)	108±4	117±7	109±5	109±7	111±5	108±4	108±5	105±3

[a] Gold standard T2 fit values from ISEC fitting of MESE data are reported as mean (ms) ± standard deviation within the group. T2 values resulting from two point fits are expressed as the relative value compared to the gold standard (%).
[b] n = 6 subjects, aged 29.0 ± 6.2 years

Table 4.3: Phantom T2 values from ISEC and Exponential Fit[a]

Sample:	1	2	3	4	5	6
[MnCl2] (mM)	27.7	67.9	124.6	270.0	401.5	512.3
T1 (ms)	2055±53	1383±24	912±43	515±16	306±21	353±7
nB1	1.11±0.03	1.17±0.03	1.20±0.05	1.01±0.04	0.90±0.03	1.03±0.04
α_R	200°±5°	211°±6°	217°±10°	183°±8°	161°±6°	186°± 8°
T2 values from various fitting methods and data sets (ms)						
Single Spin Echo	239±11	108±3	53.2±2.2	26.4±1.4	17.6±0.2	13.7±0.5
MESE (ISEC)	227±5	98±2	50.6±2.4	24.6±0.9	17.3±0.5	13.2±0.7
MESE (exponential)	267±7	124±4	68.8±3.7	32.9±1.3	24.6±0.9	19.3±1.0
FSE echo 1,7 ISEC fit	220±40	101±8	51.3±3.4	25.8±2.1	16.2±2.5	13.0±2.0
FSE echo 2,6 ISEC fit	192±19	94±6	52.5±3.5	25.1±1.9	15.6±2.2	11.8±2.0
FSE echo 1,7 exponential fit	893±704	187±24	79.0±7.2	31.7±2.6	19.2±3.1	14.8±3.2
FSE echo 2,6 exponential fit	180±14	99±6	59.5±3.6	29.8±1.9	20.8±1.9	17.3±2.1

[a] values are reported as mean ± standard deviation within the ROI.

and 70 ms (1st and 7th echoes), which agrees with the in vivo findings from Table 4.1.

Uncertainty in a T2 measurement for a range of SNR values is examined in Fig. 4.4, for a simulated T2 of 50 ms, and refocusing angle of 180°. Using ISEC, T2 fit values are increased by approximately 0 - 3% when SNR > 30 (Fig. 4.4), relative to zero noise simulations. Low SNR value results in a bias to overestimate T2 due to the noise floor. Even at high SNR values, exponential fitting fails to provide accurate results. Even where nB1 = 1 (refocusing angle = 180°), slice profile effects result in indirect and stimulated echo contamination, leading to significant errors in T2 estimation with exponential fitting.

Figure 4.5 shows the percent error in T2 fit results across a range of flip angle and
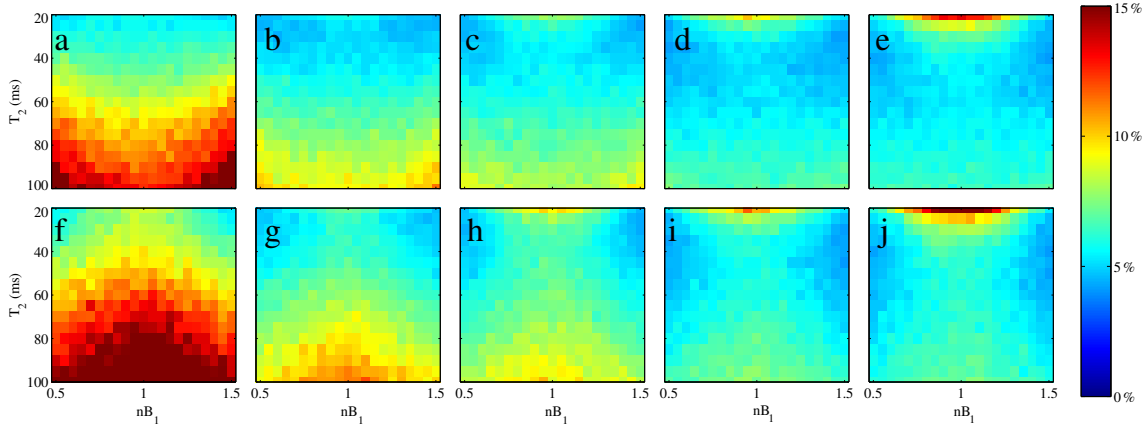
Figure 4.3: Examining instability in two point ISEC fitting. Coefficient of Variance (%) in ISEC T2 fitting results for simulated SNR of 50 are shown for a range of T2 and nB1 values, and the following echo pairs: (a) 10 and 40 ms (b) 10 and 50 ms, (c) 10 and 60 ms (d) 10 and 70 ms (e) 10 and 80 ms (f) 20 and 40 ms (g) 20 and 50 ms (h) 20 and 60 ms (i) 20 and 70 ms (j) 20 and 80 ms.
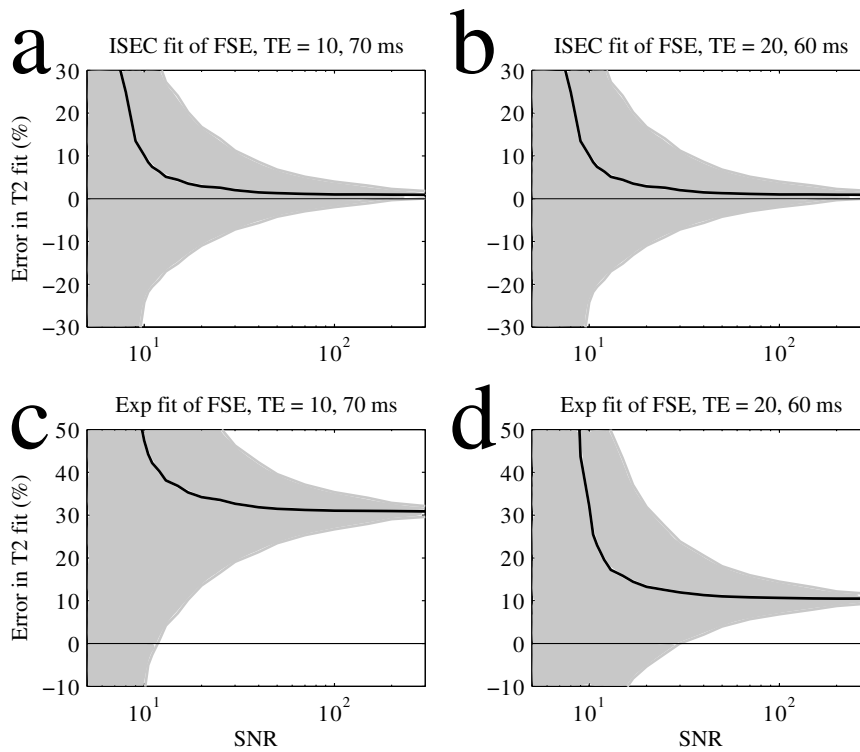
Figure 4.4: Examining SNR limitations. Mean ± standard deviation in T2 fitting error for simulated T2 of 50 ms and nB1 of 1.0 (refocusing angle of 180°) are shown for two echo choices using either (a,b) ISEC or (c,d) exponential (Exp) fitting. Mean lines are shown in black, with plus/minus one standard deviation limits shaded in grey. In general, T2 is overestimated by 0-3% with ISEC fitting when SNR > 30.

T2 values using different pairs of echoes: the first and seventh (a and c), and the second and sixth (b and d). Effects of T1 overestimation are also explored using a 1 or 2 s overestimation of the actual 1 s value. Errors in ISEC T2 fit results are larger when T1 over-estimate increases (Fig. 4.5, curves where $T_{1,dictionary} = 3$ s). Error curves from exponential fitting where the first and seventh echo are used exceed 30%, and are not shown. When T1 is overestimated by 2 s, errors occur which have a strong flip angle dependence.
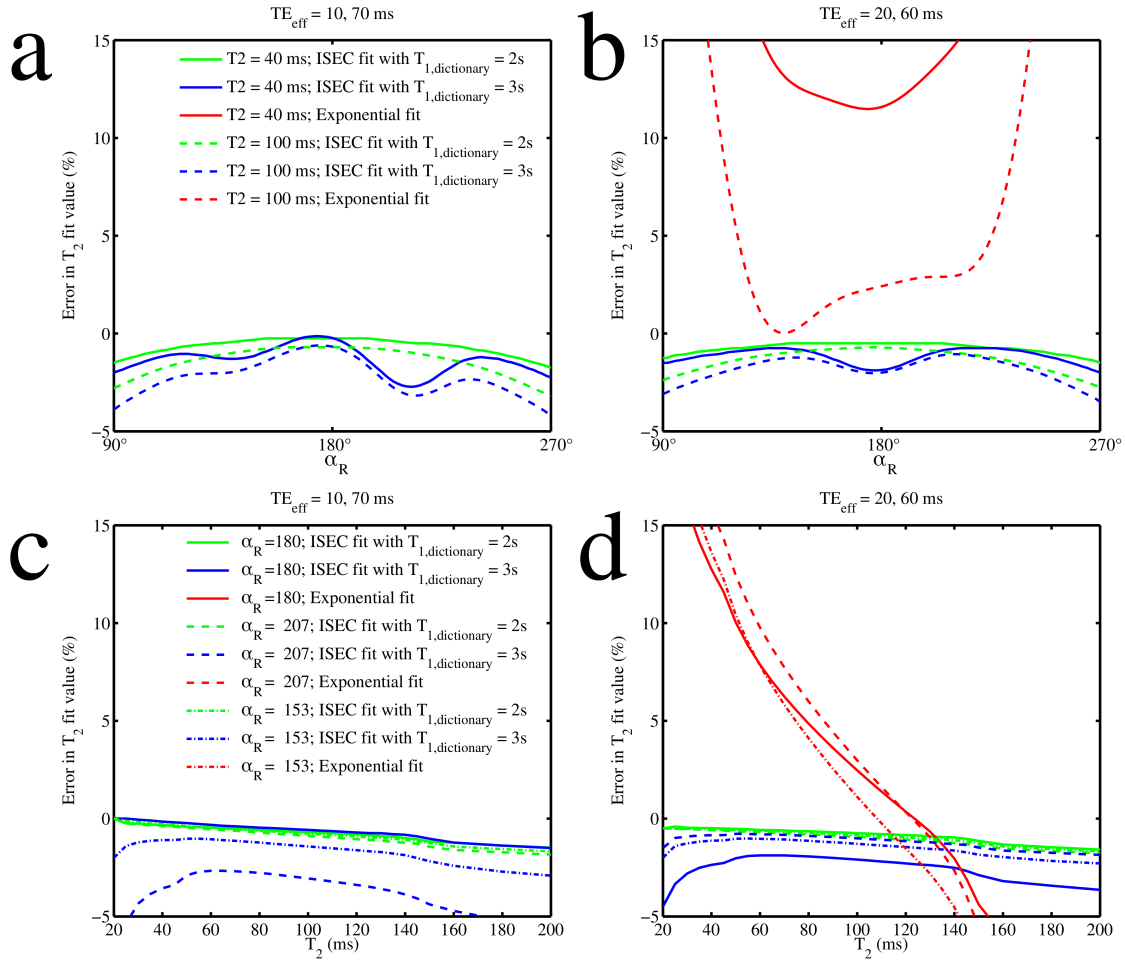
Figure 4.5: Examining T2 fit accuracy. T2 fitting accuracy is examined for a range of T2 and refocusing angles (α_R) using only two echo times: (a,c) 10 and 70 ms (1st and 7th echo), and (b,d) 20 and 60 ms (2nd and 6th echo). Here, T1 is simulated to be 1.0 s, but the lookup table used for fitting assumes 2 or 3 s. In (a,c), the exponential fit is off the graph due to errors exceeding 30%.

Error due to the assumption of a constant T1 is further examined in Fig. 4.6 using

a wide range of simulated T1 from 300 - 3000 ms, while assuming a constant T1 of 2 s. Error is shown as a function of T2 and refocusing flip angle for two point ISEC fit using the first and seventh echo. Error maps from using ISEC fitting on the second and sixth echo, and with 32 echoes contained the same features, with similar resulting fit error (within 0.5% for the majority of T1 and refocusing values), and are not shown. In general, error in the T2 measurement was found to be less than 2% when the T1 estimate was within 1 s of the actual value when refocusing angles exceeded 85°. Over-estimate of T1 by ≤1.5 s caused less than 2% error in T2 measurement error when the refocusing angle was near 180°. The importance of an accurate T1 estimate increases with increased stimulated echoes.
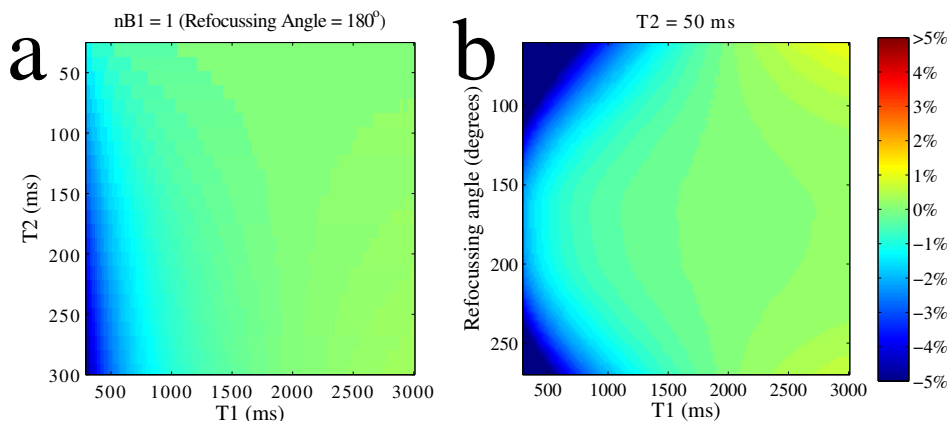
Figure 4.6: T2 error maps examining uniform T1 assumption. Error due to the assumption of a global T1 value is examined in the two point ISEC, where echoes 1 and 7 (TE = 10, 70 ms) were used. A range of T2, nB1 and T1 were simulated, and fit, assuming a global T1 of 2 s. Error in the resulting T2 fit is shown for (a) nB1 = 1, and a range of actual T1 and T2 values, and (b) T2 = 50 ms, and a range of actual T1 and nB1 values.

4.4   Discussion

The two point ISEC method described here enables accurate T2 quantification from only two FSE images (PD and T2-weighted) by modelling the pulse sequence, taking into account stimulated and indirect echoes via prior knowledge of the flip angles and slice profiles. Human brain T2 values obtained from the two point FSE method with ISEC fitting (Table 4.1) agreed very well (within 4% for most combinations of data) with the

T2 results from ISEC fitting of the 32 echo MESE data set. In phantom experiments, T2 values from both ISEC fitting of two echoes and MESE data sets agreed within uncertainty with T2 measurements from single spin echo experiments.

Exponential fits of the MESE and FSE data were not as robust (Table 4.2). The two point exponential fits of PD (TE = 10 ms) weighted and T2-weighted images grossly overestimated T2 values (33 - 112%, depending on chosen echo times), as expected from simulations.

However, exponential fits of in vivo experiments with certain combinations of data showed reasonable T2 values (Table 4.2). In particular, when the second echo (TE = 20 ms) is combined with a later echo, the exponential T2 map is much closer to the gold standard values. However, the echo time of the second echo is too late for a true PD-weighted image. Further, the T2 map is visibly warmer on the color scale (Fig. 4.2 f), and resulting values within ROIs are typically found to be larger, compared to ISEC fitting of the MESE data (Table 4.2). The error in exponential fitting results depended on both T2 and refocusing angle, when the second echo is paired with a later echo. Regions with shorter T2 values (less than $\sim$50 ms) typically overestimated T2, while moderate T2 values (50 - 80 ms) seemed to be near gold standard values. Conventionally, one may assume that using only even pairs of echoes would be sufficient to minimize stimulated echo effects; however, we have found that this approach does not remove errors, as T1 contamination is introduced via alternate echo pathways.

Knowledge of the actual flip angle and RF pulse shapes are an essential part of this advanced fitting method. The flip angle knowledge removes a parameter from the fitting process, which enables only two points to yield an accurate solution. Accurate knowledge of the flip angle and slice profile allow for appropriate compensation of indirect and stimulated echo pathways. At high magnetic field, an actual flip angle map was needed due to substantial in-plane RF variation. However at lower fields, with RF variation reduced, a flip angle map may not be necessary. At any field strength, knowledge of the RF pulse shape is required for the simulation process. If the RF pulse shapes are not provided by the vendor, they may be measured using a digital oscilloscope.

SNR simulations show that for T2 between 20 and 100 ms, the optimal pair of effective

TEs for ISEC fitting is 10 ms and 70 ms, which is supported by in vivo results (Table 4.1). Using a combination of images with TEs of 10 ms and 50 or 60 ms also performs well if T2 is between 20 and 50 ms, however, the accuracy of larger T2 values is compromised. Other combinations of FSE images could provide accurate measurements, though the accuracy depends on the TEs, and the T2 range expected. The pair of images chosen here compromises between accuracy of specific T2 values, and accuracy over the desired range of T2 values. For other applications, a different T2 weighting may be optimal. However, for clinical applications, the choice of TE of PD and T2 weighting are usually fixed, with PD being the first echo and T2-weighted using TE of 60 - 100 ms [16–18, 20]. The values found to be optimal here fall within that range.

Without previous T1 measurement, an assumption of T1 is required in calculation of the fitting model. We found that errors due to the T1 assumption were small when the T1 of the model was within 1 s of the actual T1 value (Fig. 4.5 and Fig. 4.6). Errors increase with increased stimulated echo contributions, and, when the T1 assumption is inaccurate (particularly when overestimated by 2 s), resulting errors vary significantly with refocusing angle (Fig. 4.5) due to varied contributions from indirect and stimulated echo pathways. The original implementation of ISEC found T2 measurement to be relatively insensitive to T1 when the T1/T2 ratio is large [25], however that work used a 20 echo MESE data set, allowing for averaging of T1 error across 20 points and only 10 ms between measured points. In the two point approach, the points may be 60 ms apart (10 and 70 ms). Further, the amount of T1 contamination varies with refocusing flip angle and the number of RF pulses that spins have experienced, and therefore does not contribute equally to all possible effective echo times, resulting in potential increases in error in two point fitting. We find that, when the difference between actual and assumed T1 values in fitting is greater than 1 s, errors with strong dependence on refocusing angle can occur (see Fig. 4.5, curves where the assumed T1 = 3 s). Estimating T1 to within 1 s is generally straightforward for healthy tissues. However, inclusion of an approximate T1 map could aid pathological T2 measurements.

The only difference between the pairs of FSE acquisitions used for two point ISEC fitting in this work was the effective TE, with all other parameters kept consistent. In

practice, TR, echo spacing, echo train length, or other parameters might differ between PD and T2-weighted images, which would compromise the approach used here, although potential corrections might be possible. For example, if TR is changed between sequences, this could lead to different initial magnetization in each acquisition, and result in substantial errors in T2 estimation, unless a correction factor was included for different TRs which would require knowledge of T1. Alternatively, one could use a dual echo protocol to maintain the same TR for both images, and minimize total acquisition time.

This work builds on previous implementations of spin response fitting for T2 mapping by [25], and [33]. These methods fit simultaneously for T2, flip angle, and a scaling parameter from MESE data. In order to fit for T2 from only two data points, the flip angle must be measured separately. The Lebel method underestimates nB1 [25] due to the slice profile approximation, and restricts fitting of nB1 to less than 1. Symmetry around nB1 of 1 is assumed, but has since been shown not to be the case [41]. When providing a flip angle map to a T2 fit which accounts for stimulated echoes, accurate simulations of decay curves including flip angles and slice profiles are required. In this work, we make use of the Shinnar-Le Roux algorithm for simulation of slice selective RF pulses and Bloch simulations for decay curves in order to fully simulate signal intensities of FSE images and avoid making approximations for slice profile effects.

In clinical practice, lower refocusing angles are typically used due to specific absorption rate constraints. With lower refocusing angles, stimulated echo contamination will increase, resulting in an increase in errors in exponential fitting over those examined here. Further, clinical sequences may have increased amounts of stimulated echo contributions due to the use of narrow refocusing widths relative to the excitation width. Here, we have used a refocusing slice of 1.75 x excitation width, which helps to reduce non-exponential echo contamination.

This work was performed using a single slice acquisition. It is readily extendible to multi-slice protocols, provided SNR is sufficient. Previous work has found that incidental magnetization transfer (MT) does not significantly affect grey matter T2 values, however a reduction in SNR was observed [32]. For white matter, increased delay between off-resonant RF pulses and on-resonant readout processes minimizes differential MT effects

between myelin water and other pools, due to exchange [42].

The limitations of the method quantified here are specific to the acquisition parameters (in particular, pulse shapes and timing, and echo time). For example, the use of 3D sequences may limit the effects of slice selection profile, and experiments at standard 1.5 T may limit in-plane flip angle variations. Nevertheless, any use of imperfect or non-180° refocusing angles can cause stimulated and indirect echo pathways. Simulations and experiments indicate that exponential fits using the PD (first echo) image are insufficient for T2 quantification, with errors depending on both the flip angle, and T2 value (Fig. 4.5). The experiments here used nominal refocusing angles of 180°, which varied up to 30% across the brain in a single experiment, due to high field (4.7 T) interference effects. Simulations indicate that much lower refocusing angles would result in even poorer two echo exponential fitting performance (Fig. 4.5).

In addition to allowing for rapid T2 quantification in future studies, this method potentially allows for retrospective studies on existing databases that contain PD and T2-weighted images, where flip angle maps are also available or can be predicted. Studies such as that by [16] have attempted exponential fitting of PD and T2-weighted images for T2 quantification, but found systematic differences when trying to combine data from multiple sites. This is likely due to different refocusing pulse shapes and angles, to which exponential fitting is highly sensitive. The experiments and simulations here included nominal 180° refocusing pulse trains, though a range of potential refocusing angles were examined. In clinical applications, lower refocusing pulses, or variable refocusing pulse trains may be used, further increasing the likelihood of seriously compromised results from exponential fitting.

4.5   Conclusions

In conclusion, ISEC fitting of a PD and a T2-weighted FSE image allows for accurate T2 fitting. By incorporating the actual refocusing angle into the fitting process, ISEC fitting achieves a two point fit while providing much greater accuracy and less sensitivity to refocusing pulse shape and angle than exponential fitting. This method can enable accu-

rate quantitative T2 mapping, without the need of a specialized T2 mapping acquisition, by utilizing existing PD and T2-weighted images with known flip angles.

Acknowledgements

References

[1] Alex MacKay, Cornelia Laule, Irene Vavasour, Thorarin Bjarnason, Shannon Kolind, and Burkhard M adler. Insights into brain microstructure from the T2 distribution. *Magnetic Resonance Imaging*, 24(4):515–525, May 2006.

[2] A.L. MacKay, I.M. Vavasour, A. Rauscher, S.H. Kolind, B. M adler, G.R.W. Moore, A.L. Traboulsee, D.K.B. Li, and C. Laule. MR Relaxation in Multiple Sclerosis. *Neuroimaging Clinics of North America*, 19(1):1–26, February 2009.

[3] John F. Schenck and Earl A. Zimmerman. High-field magnetic resonance imaging of brain iron: birth of a biomarker? *NMR in Biomedicine*, 17(7):433–445, 2004.

[4] Josef Vymazal, Rodney A. Brooks, Charles Baumgarner, Vu Tran, David Katz, Jeff W. M. Bulte, E. Rivka Bauminger, and Giovanni Di Chiro. The relation between brain iron and NMR relaxation times: An in vitro study. *Magnetic Resonance in Medicine*, 35(1):56–61, 1996.

[5] R. Marc Lebel, Amir Eissa, Peter Seres, Gregg Blevins, and Alan H. Wilman. Quantitative high-field imaging of sub-cortical gray matter in multiple sclerosis. *Multiple Sclerosis Journal*, 18(4):433–441, April 2012.

[6] Sean C.L. Deoni. Quantitative Relaxometry of the Brain. *Topics in magnetic resonance imaging : TMRI*, 21(2):101–113, April 2010.

[7] José M. Alústiza, José Artetxe, Agustín Castiella, Cristina Agirre, José I. Emparanza, Pedro Otazua, Manuel García-Bengoechea, Jess Barrio, Fernando Mjica, and José A. Recondo. MR Quantification of Hepatic Iron Concentration1. *Radiology*, 230(2):479–484, February 2004.

[8] Timothy C. Dunn, Ying Lu, Hua Jin, Michael D. Ries, and Sharmila Majumdar. T2 Relaxation Time of Cartilage at MR Imaging: Comparison with Severity of Knee Osteoarthritis. *Radiology*, 232(2):592–598, August 2004.

[9] Shivraman Giri, Yiu-Cho Chung, Ali Merchant, Georgeta Mihai, Sanjay Rajagopalan, Subha V. Raman, and Orlando P. Simonetti. T2 quantification for improved detection of myocardial edema. *Journal of Cardiovascular Magnetic Resonance*, 11(1), December 2009.

[10] Stephen J Matzat, Jasper van Tiel, Garry E Gold, and Edwin H G Oei. Quantitative MRI techniques of cartilage composition. *Quantitative imaging in medicine and surgery*, 3(3):162–174, June 2013.

[11] David Verhaert, Paaladinesh Thavendiranathan, Shivraman Giri, Georgeta Mihai, Sanjay Rajagopalan, Orlando P. Simonetti, and Subha V. Raman. Direct T2 Quantification of Myocardial Edema in Acute Ischemic Injury. *JACC: Cardiovascular Imaging*, 4(3):269–278, March 2011.

[12] Marnix C. Maas, Eline K. Vos, Miriam W. Lagemaat, Andreas K. Bitz, Stephan Orzada, Thiele Kobus, Oliver Kraff, Stefan Maderwald, Mark E. Ladd, and Tom W. J. Scheenen. Feasibility of T2-weighted turbo spin echo imaging of the human prostate at 7 tesla. *Magnetic Resonance in Medicine*, 71(5):1711–1719, May 2014.

[13] J. Hennig, A. Nauerth, and H. Friedburg. RARE imaging: A fast imaging method for clinical MR. *Magnetic Resonance in Medicine*, 3(6):823–833, December 1986.

[14] Peter Gibbs, Daniel J. Tozer, Gary P. Liney, and Lindsay W. Turnbull. Comparison of quantitative T2 mapping and diffusion-weighted imaging in the normal and pathologic prostate. *Magnetic Resonance in Medicine*, 46(6):1054–1058, 2001.

[15] Gary P. Liney, Adrian J. Knowles, David J. Manton, Lindsay W. Turnbull, Stephen J. Blackband, and Anthony Horsman. Comparison of conventional single echo and multi-echo sequences with a fast spin-echo sequence for quantitative T2 mapping: Application to the prostate. *Journal of Magnetic Resonance Imaging*, 6(4):603–607, 1996.

[16] Corinna M Bauer, Hernan Jara, and Ron Killiany. Whole brain quantitative T2

MRI across multiple scanners with dual echo FSE: Applications to AD, MCI, and normal aging. *NeuroImage*, 52(2):508–514, August 2010.

[17] Khader M. Hasan, Christopher Halphen, Arash Kamali, Flavia M. Nelson, Jerry S. Wolinsky, and Ponnada A. Narayana. Caudate Nuclei Volume, Diffusion Tensor Metrics, and T2 Relaxation in Healthy Adults and Relapsing-Remitting Multiple Sclerosis Patients: Implications to Understanding Gray Matter Degeneration. *Journal of magnetic resonance imaging : JMRI*, 29(1):70–77, January 2009.

[18] Khader M. Hasan, Indika S. Walimuni, Larry A. Kramer, and Richard E. Frye. Human brain atlas-based volumetry and relaxometry: Application to healthy development and natural aging. *Magnetic Resonance in Medicine*, 64(5):1382–1389, 2010.

[19] Sonja Bauer, Marlies Wagner, Alexander Seiler, Elke Hattingen, Ralf Deichmann, Ulrike Nöth, and Oliver C. Singer. Quantitative T2-Mapping in Acute Ischemic. *Stroke*, 45(11):3280–3286, November 2014.

[20] Jody L. Tanabe, Martina Vermathen, Robert Miller, Deborah Gelinas, Michael W. Weiner, and William D. Rooney. Reduced MTR in the corticospinal tract and normal T2 IN amyotrophic lateral sclerosis. *Magnetic resonance imaging*, 16(10):1163–1169, December 1998.

[21] Lili He and Nehal A. Parikh. Automated detection of white matter signal abnormality using T2 relaxometry: application to brain segmentation on term MRI in very preterm infants. *NeuroImage*, 64:328–340, January 2013.

[22] S. Majumdar, S. C. Orphanoudakis, A. Gmitro, M. O'Donnell, and J. C. Gore. Errors in the measurements of T2 using multiple-echo MRI techniques. I. Effects of radiofrequency pulse imperfections. *Magnetic Resonance in Medicine*, 3(3):397–417, 1986.

[23] S. Majumdar, S. C. Orphanoudakis, A. Gmitro, M. O'Donnell, and J. C. Gore. Errors in the measurements of T2 using multiple-echo MRI techniques. II. Effects

of static field inhomogeneity. *Magnetic Resonance in Medicine: Official Journal of the Society of Magnetic Resonance in Medicine / Society of Magnetic Resonance in Medicine*, 3(4):562–574, August 1986.

[24] Jürgen Hennig. Echoes - how to generate, recognize, use or avoid them in MR-imaging sequences. Part I: Fundamental and not so fundamental properties of spin echoes. *Concepts in Magnetic Resonance*, 3(3):125–143, 1991.

[25] R. Marc Lebel and Alan H. Wilman. Transverse relaxometry with stimulated echo compensation. *Magnetic Resonance in Medicine*, 64(4):1005–1014, 2010.

[26] Ilana R. Leppert, C. Robert Almli, Robert C. McKinstry, Robert V. Mulkern, Carlo Pierpaoli, Michael J. Rivkin, and G.Bruce Pike. T2 Relaxometry of Normal Pediatric Brain Development. *Journal of magnetic resonance imaging : JMRI*, 29(2):258–267, February 2009.

[27] Joseph R. Roebuck, Steven J. Haker, Dimitris Mitsouras, Frank J. Rybicki, Clare M. Tempany, and Robert V. Mulkern. Carr-Purcell-Meiboom-Gill imaging of prostate cancer: quantitative T2 values for cancer discrimination. *Magnetic Resonance Imaging*, 27(4):497–502, May 2009.

[28] Thomas Prasloski, Burkhard M adler, Qing-San Xiang, Alex MacKay, and Craig Jones. Applications of stimulated echo correction to multicomponent T2 analysis. *Magnetic Resonance in Medicine*, 67(6):1803–1814, 2012.

[29] W. D. Rooney, J. R. Poolaro, S. C. Forbes, D. J. Wang, K Vanderborne, and G. A. Walter. Application of the Extended Phase Graph Technique to Improve T2 Quantitation Across Sites. In *Proceedings of International Society for Magnetic Resonance in Medicine Annual Meeting 19*, volume 19, page 138, 2011.

[30] Chuan Huang, Ali Bilgin, Tomoe Barr, and Maria I. Altbach. T2 relaxometry with indirect echo compensation from highly undersampled data. *Magnetic Resonance in Medicine*, 70(4):1026–1037, 2013.

[31] Chuan Huang, Maria I. Altbach, and Georges El Fakhri. Pattern recognition for rapid T2 mapping with stimulated echo compensation. *Magnetic Resonance Imaging*, 32(7):969–974, September 2014.

[32] Md. Nasir Uddin, R. Marc Lebel, and Alan H. Wilman. Transverse relaxometry with reduced echo train lengths via stimulated echo compensation. *Magnetic Resonance in Medicine*, 70(5):1340–1346, 2013.

[33] Noam Ben-Eliezer, Daniel K. Sodickson, and Kai Tobias Block. Rapid and accurate T_2 mapping from multi-spin-echo data using Bloch-simulation-based reconstruction: Mapping Using Bloch-Simulation-Based Reconstruction. *Magnetic Resonance in Medicine*, 73(2):809–817, 2015.

[34] J. Pauly, P. Le Roux, Dwight Nishimura, and A. Macovski. Parameter relations for the Shinnar-Le Roux selective excitation pulse design algorithm [NMR imaging]. *IEEE Transactions on Medical Imaging*, 10(1):53–65, 1991.

[35] G. J. Parker, G. J. Barker, and P. S. Tofts. Accurate multislice gradient echo T(1) measurement in the presence of non-ideal RF pulse shape and RF field nonuniformity. *Magnetic Resonance in Medicine: Official Journal of the Society of Magnetic Resonance in Medicine / Society of Magnetic Resonance in Medicine*, 45(5):838–845, May 2001.

[36] N Takaya, H Watanabe, and F Mitsumori. Elongated T1 values in human brain and the optimization of MDEFT measurements at 4.7t. In *Proceedings of the 12th Annual Meeting of ISMRM*, volume 12, page 2339, Kyoto, Japan, 2004.

[37] David L. Thomas, Enrico De Vita, Ralf Deichmann, Robert Turner, and Roger J. Ordidge. 3d MDEFT imaging of the human brain at 4.7 T with reduced sensitivity to radiofrequency inhomogeneity. *Magnetic resonance in medicine : official journal of the Society of Magnetic Resonance in Medicine / Society of Magnetic Resonance in Medicine*, 53(6):1452–1458, June 2005.

[38] P Jezzard, S Duewell, and R S Balaban. MR relaxation times in human brain: measurement at 4 T. *Radiology*, 199(3):773–779, June 1996.

[39] Rudolf Stollberger and Paul Wach. Imaging of the active B1 field in vivo. *Magnetic Resonance in Medicine*, 35(2):246–251, 1996.

[40] Mustapha Bouhrara and Jean-Marie Bonny. B1 mapping with selective pulses. *Magnetic Resonance in Medicine*, 68(5):1472–1480, November 2012.

[41] Dylan Breitkreutz, Kelly C McPhee, and Alan H. Wilman. Value of Independent Flip Angle Mapping for Transverse Relaxometry with Stimulated Echo Compensation. In *Proceedings of ISMRM 21*, page 2466, Salt Lake City, Utah, USA, 2013.

[42] Irene M. Vavasour, Kenneth P. Whittall, David K.B. Li, and Alex L. MacKay. Different magnetization transfer effects exhibited by the short and long T2 components in human brain. *Magnetic Resonance in Medicine*, 44(6):860–866, 2000.

Chapter 5

T1 and T2 Quantification from Standard Images

Purpose: To extract quantitative longitudinal and transverse (T1 and T2) relaxation maps from standard MRI methods.

Methods: Bloch simulations and known flip angles were used to model relative signal amplitudes from standard turbo spin echo sequences: Proton Density (PD) weighted, T2-weighted and T1-weighted or T2-weighted FLuid Attenuated Inversion Recovery (FLAIR). Simulations over a range of expected parameter values yielded a look-up table which was used to determine T1 and T2 from these weighted images. The same sequences and a flip angle map were acquired in 8 subjects at 3.0 T using both multi-slice and single slice acquisitions. T1 and T2 maps were fit from the resulting data using PD and T2 weighting and either T1-weighted or FLAIR images, and the flip angle map. Results are compared to inversion recovery experiments for T1, and 20 echo multi-echo spin echo sequences for T2.

Results: T1 and T2 maps may be acquired from only three weighted images and a flip angle map. In comparison to the gold standard methods, single slice PD-T2 and T1-weighted images provided average T1 values within 7% in grey matter and 13% in white matter, and T2 values within 5% in grey mat-

ter and 7% in white matter. In multi-slice acquisitions optimized to reduce cross talk and incidental magnetization transfer, average T1 and T2 values were within 10% and 7% of gold standard, respectively. Best results were achieved using PD-T2 and standard T1-weighting rather than FLAIR. Incidental magnetization transfer reduced T1 accuracy in multi-slice acquisitions with a standard interleaved acquisition. T2 maps were largely unaffected by the choice of T1-weighted or T2-FLAIR image, paired with PD-T2 weighting.

Conclusions: Through exact sequence modelling, and separate measurement of flip angles, T2 and T1 may be quantified from a standard brain protocol of TSE images with PD, T2 and T1-weighting. This approach may enable the introduction of quantitative relaxation into radiology protocols without substantial time penalties.

5.1 Introduction

Relaxation mapping may be used for investigation of the brain [1–4] and body [5–11]. Accurate measurement of relaxation times, rather than the acquisition of only weighted images allows for direct tissue quantification of a biological parameter with removal of variations arising from transmit and receive RF fields and scanner gain.

In the clinic, relaxation-weighted images are routinely acquired, but quantifying the relaxation times typically requires additional specialized pulse sequences and hence additional imaging time, which is not typically feasible in standard clinical practice.

Researchers have sought to acquire quantitative maps rapidly by either directly fitting weighted images [12–14] or through use of specialized sequences (for example, fingerprinting [15, 16], DESPOT1 and DESPOT2 [17, 18], QRAPMASTER [19, 20], or multi-slice inversion recovery [21]). Some authors have used these parameter maps to then create synthetic weighted MR images [20, 22]. While these methods have shown promise, they still rely on additional pulse sequences and often sacrifice the spatial precision found in common weighted images (in order to save time or due to inherent SNR and artefact limitations). Weighted images have dominated radiology practice because they have provided

adequate spatial resolution and contrast differences between tissues. Weighted images will likely continue to dominate the practice of Radiology; however, if quantitative maps could be obtained from the same data, the pathway to acceptance of these maps might be more open.

Our goal is to produce relaxation maps directly from weighted images that are commonly used. All weighted sequences have a Turbo (or fast) Spin Echo (TSE) base and use the standard forms of contrast for brain imaging: Proton Density (PD), T2-weighted (T2w), T1-weighted (T1w) and T2-weighted FLuid Attenuated Inversion Recovery (FLAIR). Through exact modelling of these pulse sequences using the Bloch equations and a flip angle map, we propose direct extraction of quantitative T1 and T2 relaxation maps.

Recently, we introduced methods for accurately quantifying T2 from only a PD and a T2w TSE, and a flip angle (B1) map [13]. This current work extends these methods to quantify T1 and T2 simultaneously, with the addition of either a T1w image, or a T2w FLAIR image. Through simultaneous fitting, we demonstrate both T2 and T1 mapping in comparison to gold standard approaches of inversion recovery experiments and multiple-echo spin echoes in human brain at 3.0 T.

5.2 Methods

5.2.1 In Vivo Experiments

All experiments were performed at 3.0 T (PRISMA; Siemens Healthcare; Erlangen, Germany). All subjects provided written, informed consent, and this investigation was approved by the local institutional ethics board. Brain imaging was performed on eight volunteers (4 male, mean age 29, range 23 - 34 years) using a 64 channel head coil. Dual Echo TSE (TE = 10.3 , 92.7 ms; TR = 5 s; turbo factor = 8; Refocusing angle = 165°; 2 concatenations; Time of Acquisition (TA) = 2:42 × 2), T2w FLAIR (TI = 2200 ms; TE = 82.4 ms; TR = 5 s; turbo factor = 8; Refocusing angle = 165°; 2 concatenations; TA = 2:42 × 2), and T1-weighted TSE (TE = 10.3; TR = 600 ms; turbo factor = 8;

Refocusing angle = 165°; 4 concatenations; TA = 0:40 × 2) images were acquired in 2D multi-slice axial acquisitions with 30 contiguous slices. Parallel imaging (GRAPPA) with acceleration factor of 2 was used in all cases. Odd and even slices were collected on separate acquisitions in all cases, with each in an interleaved slice acquisition order to reduce incidental MT and avoid cross-talk between slices. Images were acquired with matched resolution (3 mm slices, voxel size = 0.86 × 0.86 × 3 mm^3; typical matrix = 256 × 208). These sequences were repeated as single slice acquisitions, matching a slice from the multi-slice acquisition through deep grey matter. In 5 subjects, the dual echo TSE was repeated with a refocussing angle of 150° (PD-T2$_{150}$) to compare to the typical 165°(PD-T2$_{165}$). In addition, all multi-slice images were repeated in 6 subjects using a more standard single acquisition with all slices interleaved. Flip angle maps were collected on all subjects using a Bloch-Seigert approach (TE 2.24 ms; TR 16150 ms, flip angle 80; voxel size 1.1 × 1.1 × 3.0 mm; matrix = 192 × 192 × 36; TA = 0:33). B1 maps were interpolated to match TSE data. B1 is expressed here as a normalized parameter relating the resulting flip angle to the prescribed flip angle: $\alpha = B1\alpha_{prescribed}$.

For traditional gold standard relaxation measurement, single slice multi-echo spin echo (20 echoes; TE = 10 - 200 ms with 10 ms echo spacing; TR = 5 s; Refocussing angle = 180°; voxel size = 1.14 × 1.14 × 3 mm^3; matrix = 192 × 156 × 1; TA = 5:32), and an inversion recovery experiment (eight inversion prepared TSE; TI = 50, 100, 200, 500, 1000, 2200, 3000, 4500 ms; TE =10 ms; TR modified for each acquisition for constant TR - TI = 5 s [23]; turbo factor = 8; Refocussing angle = 165°; voxel size = 0.86 × 0.868 × 3 mm^3; matrix = 256 × 208 × 1; 1 concatenation; total TA 13:59) was also performed. One subject had only the first 7 inversion times.

Images were coregistered to the PD-weighted image from the dual echo TSE using a rigid in-plane transform. No subject moved sufficiently to require 3D registration. Regions-of-interest (ROIs) were drawn using the T2w image from the multi-slice dual echo image, and the TI = 500 ms image from the inversion recovery experiment. ROIs were drawn selecting five grey matter (globus pallidus, putamen, caudate head, thalamus, cortical grey matter), and three white matter (frontal white matter, posterior white matter, internal capsule) regions. Bilateral ROIs were combined to provide parameter

113

averages in chosen regions. To enable comparison, only the slice from multi-slice images which corresponded to the single slice images were used.

5.2.2   Sequence Modelling and Fitting

All experimental pulse sequences used for relaxation measurements were simulated using the exact experimental waveforms, specifically: PD, T2 and T1-weighted TSE, FLAIR and the gold standard comparisons of multiple echo spin echo and multiple inversion recovery TSE. Bloch equations were used to model relaxation and SLR simulations were used for RF pulses, as previously described [13, 24]. All simulations were performed using in-house MATLAB (R2014a, 64 bit) code.

T2 fitting from only a dual echo TSE data set has previously been described [13]. Here, we examine a modified approach to the previously presented method, where a T1-weighted data point is also considered (either a T1w TSE, or T2w FLAIR TSE image), and the three data points are simultaneously compared to lookup tables which include a range of T1, T2 and flip angle values. Tables of the steady state SE signal intensities were pre-computed for a range of parameters for each sequence (reported as minimum: step size: maximum): dual echo (T1 = 300:100:3500 ms, T2 = 20:0.1:200 201:1:300 300:5:500 500:10:1000 ms, normalized B1 = 0.6:0.005:1.4), T1-weighted (T1 = 300:50:3500 ms, T2 = 20:1:200 205:.5:260 280:20:500 550:50:1000 1000:100:1000 ms, B1 = 0.6:0.005:1.4), and T2w FLAIR (T1 = 300:50:3500, T2 = 20:2:200 200:10:300 300:50:1000 ms, B1 = 0.6:0.005:1.4) . RF pulses were modelled with the SLR algorithm [25], at a resolution of 1024 points equally spaced over the duration of the pulse. In order to model slice selection, typically 1001 points equally spaced over three times the excitation width in the slice-select direction were modelled independently, and summed together. The previously described model was expanded to account for variation in TR, and to allow for the addition of an inversion preparation pulse to the TSE acquisition. Steady state signal amplitudes were calculated by repeating the sequence simulation, to achieve a steady state. The sequence was repeated a minimum of 5 times, or until the amplitude of the first echo changed by less than 0.1% in subsequent repetitions.

The fitting routine minimizes the sum of squares of the difference between each data

point (PDw, T2w, and either T1w or T2w-FLAIR) and the corresponding signal ampli-
tudes from each look-up table to fit for T1, T2 and a scaling parameter. The PD-T2
table is interpolated in the T1 direction to the estimated point, and uses the nearest
point in the T2 and B1 indexes. The T1w (or FLAIR) table is interpolated to the same
T2, B1, and T1 values. A diagram indicating the fitting procedure for PD, T2w, and
T1w images is shown in Figure 5.1. The same procedure is used to compute parameter
maps when T2w FLAIR images are used. M0 maps, true TE = 0 images, or synthetic
images at any other echo time in the echo train may be extracted from the look-up table,
if desired.
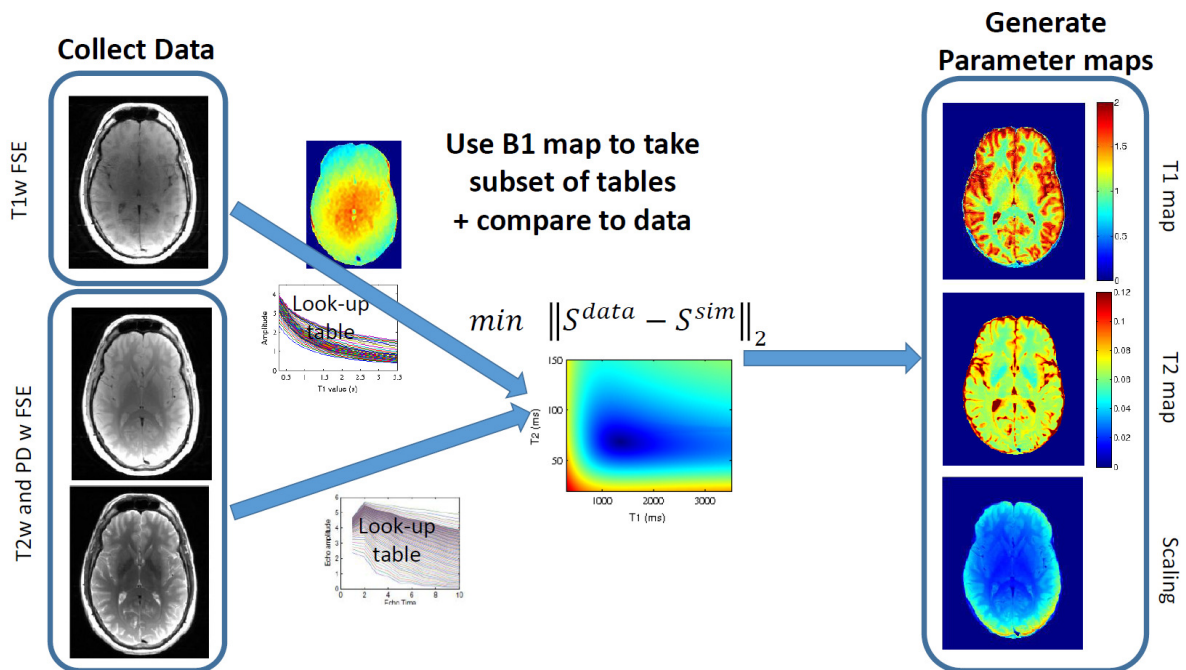
Figure 5.1: The flow chart indicates the process for acquiring data and generating relax-
ation maps. Dual echo PD-T2-weighted TSE, T1-weighted TSE, and a rapid B1 map
are acquired. The B1 map is used to take a subset of data from the tables, resulting in a
T1-T2 fitting space for each 3 point data set. The fitting algorithm finds the minimum
of the sum squared residuals, and T1, T2, and amplitude maps (scaling) are generated.

5.2.3   Simulated Experiments

Simulations were performed to investigate the impact of noise on the simultaneous T1-
T2 measurement, and induced error if the flip angle measurement is inaccurate. Signal

amplitudes for PD-T2, and T1w data with T2 = 60 ms, T1 = 1.0 s, and refocussing angle = 165° were simulated with added noise. Random complex Gaussian noise with a range of amplitudes to simulate a PDw image with SNR ranging from 5 - 200 was added to simulated complex data. Each point was simulated 500 times. The resulting signal magnitudes were fit, and the mean and standard deviation in resulting T1 and T2 values were plotted. Signal amplitudes for PD-T2, and T1w data with T2 = 60 ms, T1 = 1.0s, and nominal refocussing angle = 165°, were simulated for a range of B1 values (0.8 - 1.2). The results were fit with a range of erroneous B1 values (0.05).

5.2.4   Statistics

Shapiro-Wilk tests, Q-Q plots and histograms were used to check for normality of data. Wilcoxon rank sum tests were performed to test if T1 and T2 fit results from each three point data set was significantly different from the gold standard. Values from each multi-slice protocol were compared to each other and to results from single slice acquisitions. Results from data sets including T1w were compared to results from data sets which included FLAIR data. Multiple comparisons of methods were accounted for with Bonferroni correction, and analysis was carried out using $\alpha = 0.05$.

5.3   Results

T1 and T2 maps may be fit using only three TSE images (PDw, T2w, and either T1w or T2w-FLAIR), and a B1 map, as demonstrated in Figure 5.1. T1 and T2 maps provide the added benefit over use of weighted images in that variations in signal intensity due to transmit and receive coils are removed (Figure 5.2). Example T1 and T2 maps derived from one volunteer are shown in Figure 5.3 and Figure 5.4 respectively, where the gold standard methods shown in 5.3a and 5.4a, in comparison to maps computed from weighted images. Averages from each ROI are displayed in Tables 5.1 and 5.2 for single and multi-slice experiments, compared to gold standard T1 and T2 measurements. T1 and T2 results from four ROIs are compared in box plots in Figure 5.5. T2 values are similar, regardless of which TSE data set they are derived from, and are generally within

116

~ 5% of the MESE derived value, though in most cases the values from TSE data sets underestimated the MESE value. The T2 values are not found to be significantly different across methods (except in frontal white matter, as indicated in Table 5.2). However, T1 values vary substantially, depending on the ROI and data acquisition method. In many cases T1 values are significantly different across methods (as indicated in Table 5.1 and 5.2). The T1 values derived from PD-T2 and T2w-FLAIR images, and values derived from images with contiguous slices (vs odd and even separately acquired) are the least accurate (up to 51% error). Single slice acquisitions of PD-T2 and T2w-FLAIR mis-estimate T1 by as much as 20%. T1 values from single slice data sets (PD-T2 and T1w) are the most accurate (average values were within 7% in grey matter and 13% in white matter), compared to the inversion recovery experiment. In grey matter, T1 from single slice experiments were not found to be significantly different from gold standard. Average T1 values from single slice PD-T2 and T2w-FLAIR are within 19% of inversion recovery T1 values. Values from multi-slice acquisition of PD-T2 and T1w images have similar accuracy (up to 10% error) in grey matter and improved results in white matter (within 3%).

Table 5.1: T1 and T2 (ms) values from Single Slice Experiments

	Data Set	N	Globus Pallidus	Caudate	Putamen	Thalamus	Cortical GM	Frontal WM	Posterior WM	Internal Capsule
B1			1.12 ± 0.02	1.07 ± 0.01	1.10 ± 0.01	1.17 ± 0.02	1.01 ± 0.02	0.94 ± 0.02	1.04 ± 0.02	1.13 ± 0.02
T1	IR	8	1013 ± 23	1427 ± 20	1270 ± 31	1184 ± 25	1428 ± 75	851 ± 33	855 ± 25	924 ± 38
T1	PD-T2, T2w-FLAIR	8	1011 ± 20¶	1205 ± 25*¶	1131 ± 31*¶	1062 ± 17*¶	1249 ± 73*¶	838 ± 25¶	879 ± 23¶	993 ± 58¶
T1	PD-T2, T1w	8	1068 ± 34¶	1463 ± 61¶	1311 ± 57¶	1197 ± 31¶	1528 ± 101¶	954 ± 31*¶	963 ± 23*¶	1006 ± 57*
T2	MESE	8	47.4 ± 1.7	70.8 ± 2.5	60.5 ± 2.3	63.9 ± 1.0	73.2 ± 5.8	58.5 ± 1.1	70.5 ± 2.2	78.3 ± 6.8
T2	PD-T2, T2w-FLAIR	8	47.2 ± 2.5	68.2 ± 1.8	59.0 ± 1.4	62.0 ± 1.6	70.3 ± 4.5	57.7 ± 1.6	67.6 ± 2.5	72.5 ± 4.7
T2	PD-T2, T1w	8	47.2 ± 2.5	67.8 ± 1.7	58.7 ± 1.4	61.8 ± 1.5	69.9 ± 4.4	57.5 ± 1.6	67.4 ± 2.5	72.5 ± 4.7
SNR	PD		49	65	63	49	128	70	83	49
ROI Size	# pixels		206 ± 54	122 ± 52	500 ± 75	335 ± 43	50 ± 14	177 ± 70	153 ± 60	57 ± 8

* indicates values is significantly different from gold standard
¶indicates that the 3 point method using PD-T2 and T1w is significantly different from the value derived from PD-T2 and FLAIR.

In the multi-slice acquisition with even and odd slices separately acquired, reducing the refocussing angle in the PD-T2 resulted in similar T1 values with only average 2% difference (not shown). This improvement was larger in data sets including FLAIR, than in data sets including a T1w image. The use of the FLAIR image for T1 fitting in multi-slice acquisition was less accurate, though the methods appear to have similar
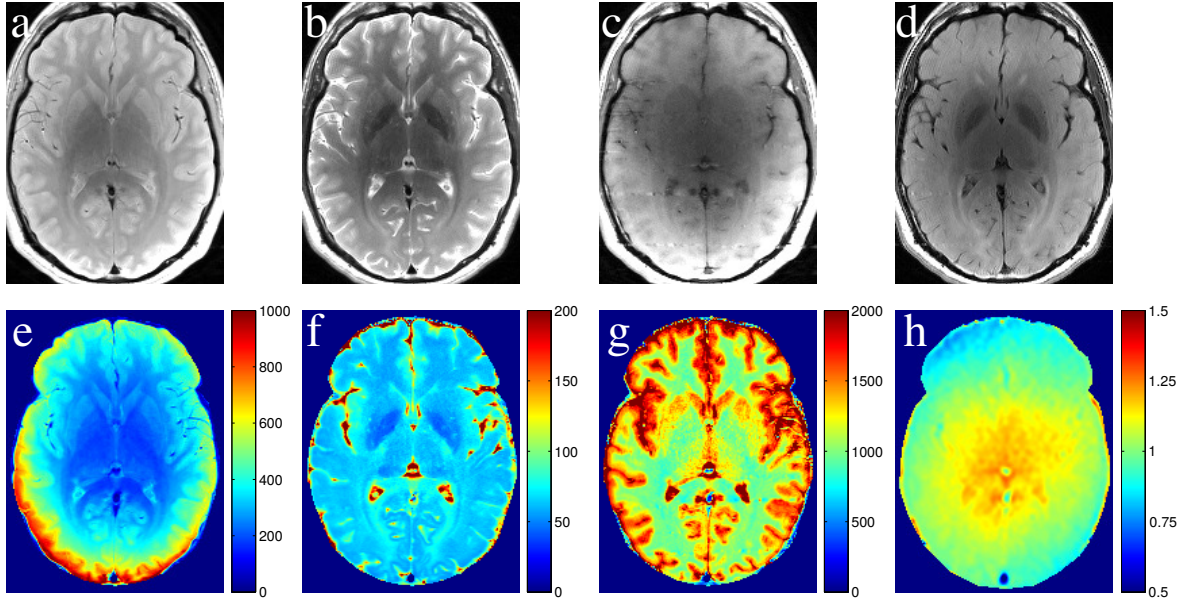
Figure 5.2: Raw (a) PDw, (b) T2w, (c) T1w, (d) T2-FLAIR images processed in N4 to reduce inhomogeneity due to receiver profile and RF inhomogeneity, are compared to the corresponding parameter maps (e) scaling amplitude, (f) T2 map, (g) T1 map, resulting from fitting the TSE images with an input measured (h) B1 map. Parameter maps were calculated using raw images prior to N4 processing.

precision.

Ratios of each multi-slice PD-weighted, FLAIR and T1w TSE image to their single slice equivalent are compared in Figure 5.6. In each case, the acquisitions with contiguous slices showed the largest reduction in signal intensity relative to the single slice acquisition. The signal loss in the T1w image is most similar to the PD with 150° refocussing. Signal loss in the FLAIR image due to incidental MT has different features than any of the PDw TSE images. This is consistent with larger errors in T1 values derived from data sets including the T2w-FLAIR images.

Simulations show that T1 and T2 fitting are sensitive to inaccuracies in the measured B1 map (Figure 5.7a-b). However, if the B1 value is accurate within 5%, the error in T1 and T2 is lower than 5%. SNR simulations (Figure 5.7c-d) show that average T1 and T2 values remain accurate, even at low SNR. However the standard deviation in the resulting values exceeds 8% in T1, and 5% in T2 where SNR < 40. Typically, SNR in experiments exceeded 40.
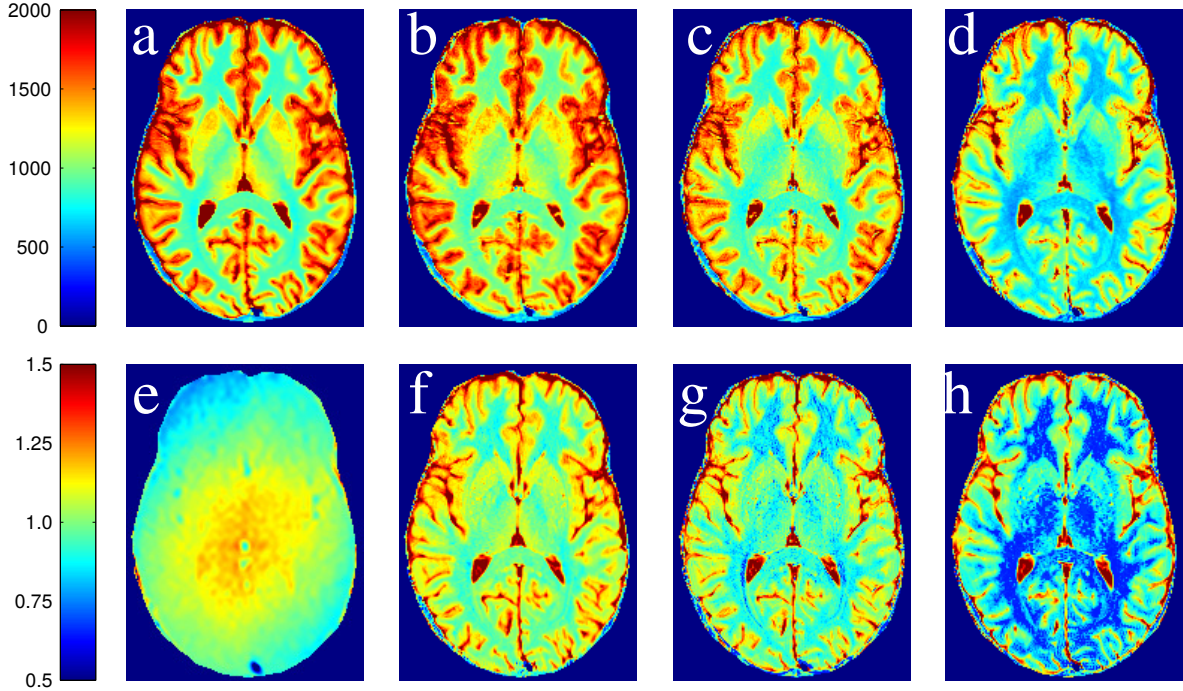
Figure 5.3: T1 maps (ms) from (a) single slice inversion recovery, and (e) the measured B1 map are compared to T1 maps determined from each combination of dual echo and T1w or T2-FLAIR images: (b) single slice dual echo and T1w, (c) multi-slice dual echo and T1w with even and odd separately acquired, (d) multi-slice dual echo and T1w with contiguous slice acquisition, (f) single slice dual echo and T2-FLAIR, (g) multi-slice dual echo and T2-FLAIR with even and odd separately acquired, (h) multi-slice dual echo and T2-FLAIR with contiguous slice acquisition. T1 values vary, depending on which set of data is used to compute parameter maps. These maps correspond to the T2 maps shown in Figure 5.4

5.4 Discussion

Combination of a dual echo TSE, T1w TSE, and a B1 map was sufficient to measure T1 and T2. Single slice acquisitions provided T1 values within 7% in grey matter, and within 13% in white matter. Corresponding T2 values are within 5% in grey matter and 7% in white matter. Multi-slice protocols are less accurate, and are within 10% of gold standard for the separate odd/even acquisition, and up to 32% error compared to inversion recovery results in standard contiguous multi-slice acquisitions. Thus, slice order is an important consideration with this approach. T2 values are less sensitive to acquisition and are not found to be significantly different across methods (P>0.005 except in frontal white matter, comparing values from contiguous FLAIR and PD-T2),
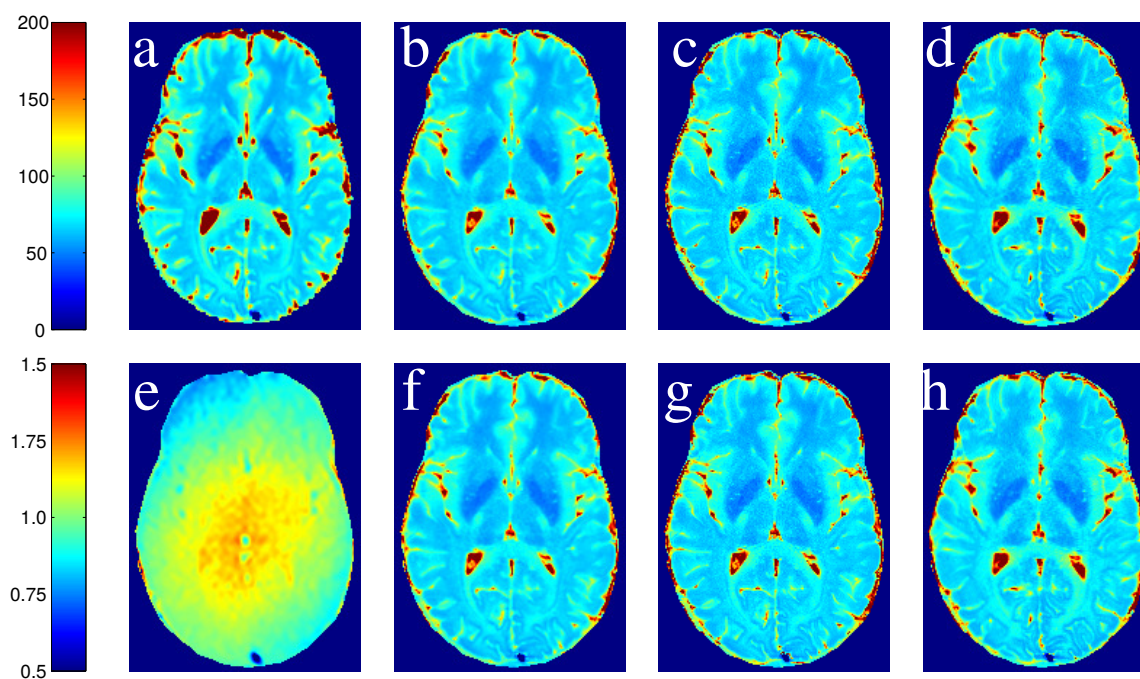
Figure 5.4: The T2 map (ms) from (a) MESE with ISEC fitting and (e) the measured B1 map are compared to maps determined from each combination of dual echo and T1w or T2-FLAIR images: (b) single slice dual echo and T1w, (c) multi-slice dual echo and T1w with even and odd separately acquired, (d) multi-slice dual echo and T1w with contiguous slice acquisition, (f) single slice dual echo and T2-FLAIR, (g) multi-slice dual echo and T2-FLAIR with even and odd separately acquired, (h) multi-slice dual echo and T2-FLAIR with contiguous slice acquisition. These maps correspond to the T1 maps shown in Figure 5.3. T2 maps are scaled 0 to 200 ms, and the B1 map is scaled 0.5 to 1.5.

though results varied slightly ($\sim$5% variation) across methods.

Using only weighted images for T1 and T2 mapping, removes the requirement for specialized sequences. However, incidental MT in multi-slice acquisitions resulted in a loss in signal intensity, which had unequal effects for each of the T1-weighted, dual echo, and FLAIR acquisitions, and does not equally affect different regions of the brain due to variations in B1 and tissue MT sensitivity [26]. This resulted in variable error in T1 measurement, depending on sequences used, and brain region. Multi-slice data acquired with odd and even data sets in separate acquisitions minimize these MT differences, compared to interleaved multi-slice acquisition of all contiguous slices. Separating even
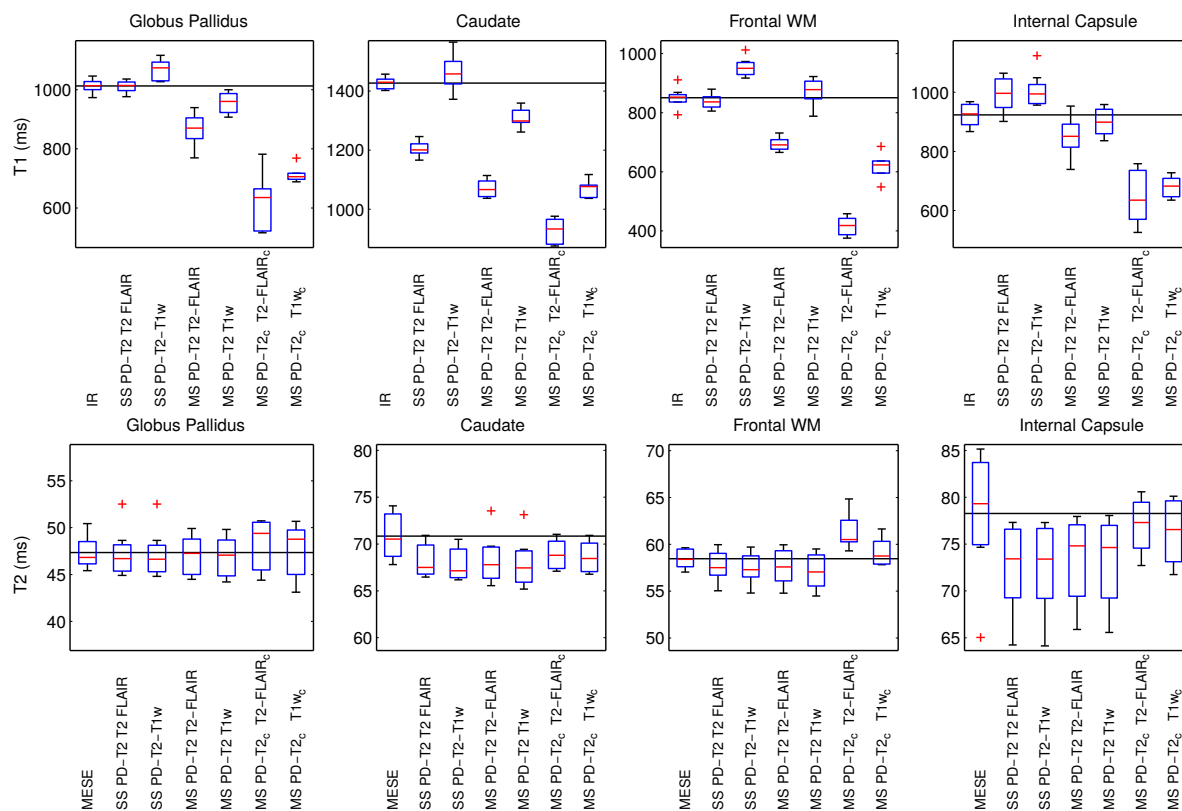
Figure 5.5: T1 (top row) and T2 (bottom row) values (ms) derived from the various possible combinations of data are compared in four ROIs using a box and whisker diagram. Multi-slice and single slice are abbreviated MS and SS. Subscript c indicates the contiguous acquisition. On each box, the central mark indicates the median value and the bottom and top edges of the box indicate the 25th and 75th percentiles, respectively. Whiskers show the maximum and minimum data points, not including outliers. Outliers are plotted using + symbol.

and odd slices into two acquisitions also avoids cross talk, which may be present in unequal amounts in the contiguous acquisition. For this reason, combinations of data from each acquisition type were not considered. The even and odd separate acquisitions are non-standard. In future, improved slice interleaving options could be implemented to further reduce incidental MT and cross talk. All multi-slice acquisitions resulted in variable MT across each image type, and hence errors in T1 measurement. Balancing MT effects across experiments is a future direction of this work. Nevertheless, T2 measurements were relatively consistent, regardless of the data combination used, likely because the dual echo images provide most of the contrast for the T2 fitting, and both echoes are equally impacted by MT and cross-talk effects. The issues with slice cross-talk and MT

Table 5.2: T1 and T2 (ms) values from Multi-slice Experiments

	Data Set	N	Globus Pallidus	Caudate	Putamen	Thalamus	Cortical GM	Frontal WM	Posterior WM	Internal Capsule
B1			1.12 ± 0.02	1.07 ± 0.01	1.10 ± 0.01	1.17 ± 0.02	1.01 ± 0.02	0.94 ± 0.02	1.04 ± 0.02	1.13 ± 0.02
T1	IR	8	1013 ± 23	1427 ± 20	1270 ± 31	1184 ± 25	1428 ± 75	851 ± 33	855 ± 25	924 ± 38
T1	PD-T2, T2w-FLAIR	8	$866 \pm 54^{*\dagger\P}$	$1070 \pm 30^{*\dagger\P}$	$1004 \pm 45^{*\dagger\P}$	$918 \pm 24^{*\dagger\P}$	$1113 \pm 82^{*\P}$	$694 \pm 22^{*\dagger\P}$	$729 \pm 25^{*\dagger\P}$	$851 \pm 65^{*\dagger\P}$
T1	PD-T2c, T2w-FLAIR$_c$	6	$626 \pm 100^{*\dagger\P}$	$928 \pm 42^{*\dagger\P}$	$824 \pm 30^{*\dagger\P}$	$692 \pm 82^{*\dagger\P}$	$908 \pm 36^{*\dagger\P}$	$417 \pm 33^{*\dagger\P}$	$415 \pm 41^{*\dagger\P}$	$643 \pm 91^{*\dagger\P}$
T1	PD-T2, T1w	8	$956 \pm 36^{*\dagger\P}$	$1310 \pm 31^{*\dagger\P}$	$1179 \pm 55^{\dagger\P}$	$1061 \pm 48^{*\dagger\P}$	$1353 \pm 112^{\P}$	$872 \pm 44^{\P}$	$875 \pm 28^{\dagger\P}$	$900 \pm 46^{\dagger}$
T1	PD-T2c, T1w$_c$	6	$714 \pm 29^{*\dagger\P}$	$1072 \pm 30^{*\dagger\P}$	$934 \pm 27^{*\dagger\P}$	$808 \pm 41^{*\dagger\P}$	$1055 \pm 64^{*\dagger\P}$	$619 \pm 46^{*\dagger\P}$	$644 \pm 26^{*\dagger\P}$	$681 \pm 36^{*\dagger\P}$
T2	MESE	8	47.4 ± 1.7	70.8 ± 2.5	60.5 ± 2.3	63.9 ± 1.0	73.2 ± 5.8	58.5 ± 1.1	70.5 ± 2.2	78.3 ± 6.8
T2	PD-T2, T2w-FLAIR	8	47.1 ± 2.1	68.3 ± 2.6	59.0 ± 2.7	62.8 ± 1.1	70.3 ± 5.1	57.6 ± 2.0	68.2 ± 2.8	73.3 ± 4.6
T2	PD-T2c, T2w-FLAIR$_c$	6	48.3 ± 2.7	68.9 ± 1.6	58.4 ± 1.0	63.2 ± 1.4	69.6 ± 1.9	$61.3 \pm 2.0^{\dagger}$	71.7 ± 2.0	77.0 ± 3.0
T2	PD-T2, T1w	8	46.9 ± 2.2	68.0 ± 2.6	58.8 ± 2.7	62.6 ± 1.1	69.9 ± 5.1	57.1 ± 2.0	67.8 ± 2.8	73.2 ± 4.7
T2	PD-T2c, T1w$_c$	6	47.7 ± 3.0	68.6 ± 1.6	58.2 ± 1.0	62.7 ± 1.6	69.3 ± 1.9	59.2 ± 1.5	69.1 ± 1.8	76.3 ± 3.4
SNR	PD		43	60	57	43	113	61	72	41
ROI Size	(# pixels)		206 ± 54	122 ± 52	500 ± 75	335 ± 43	50 ± 14	177 ± 70	153 ± 60	57 ± 8

* indicates values is significantly different from gold standard

† indicates the value derived from the multi-slice protocol is significantly different from the value derived from the single slice protocol.

¶indicates that the 3 point method using PD-T2 and T1w is significantly different from the value derived from PD-T2 and FLAIR.

subscript c indicates multislice acquisitions where slices were acquired contiguously.
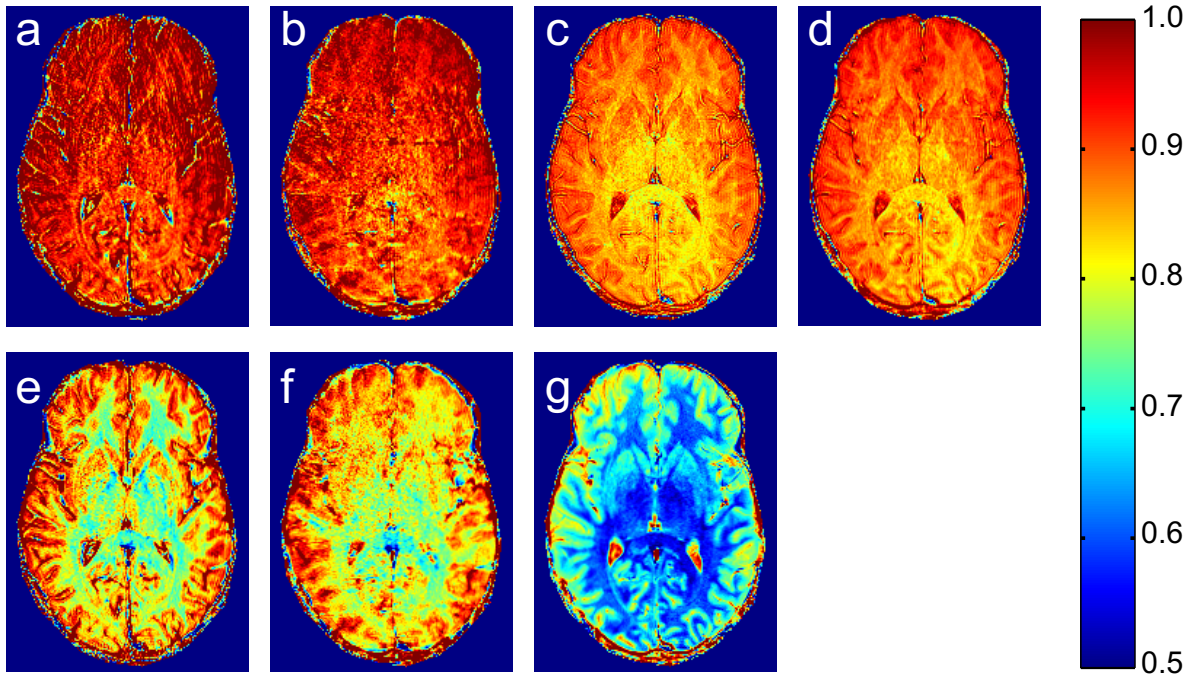
Figure 5.6: The ratio of image intensity of multi-slice weighted images relative to the single slice equivalent acquisition are shown for: (a) T2w-FLAIR (b) T1w (c) PD$_{165}$,(d) PD$_{150}$, where even and odd were collected on separate acquisitions, (e) T2w-FLAIR$_c$ (f) T1w$_c$ (g) PD$_{165}$, contiguous slice acquisitions. The contiguous slice acquisitions (e-g) show much more signal loss than the corresponding multi-slice acquisitions where odd and even slices were collected in separately (a-c). A value of 1.0 indicates no change in signal intensity.
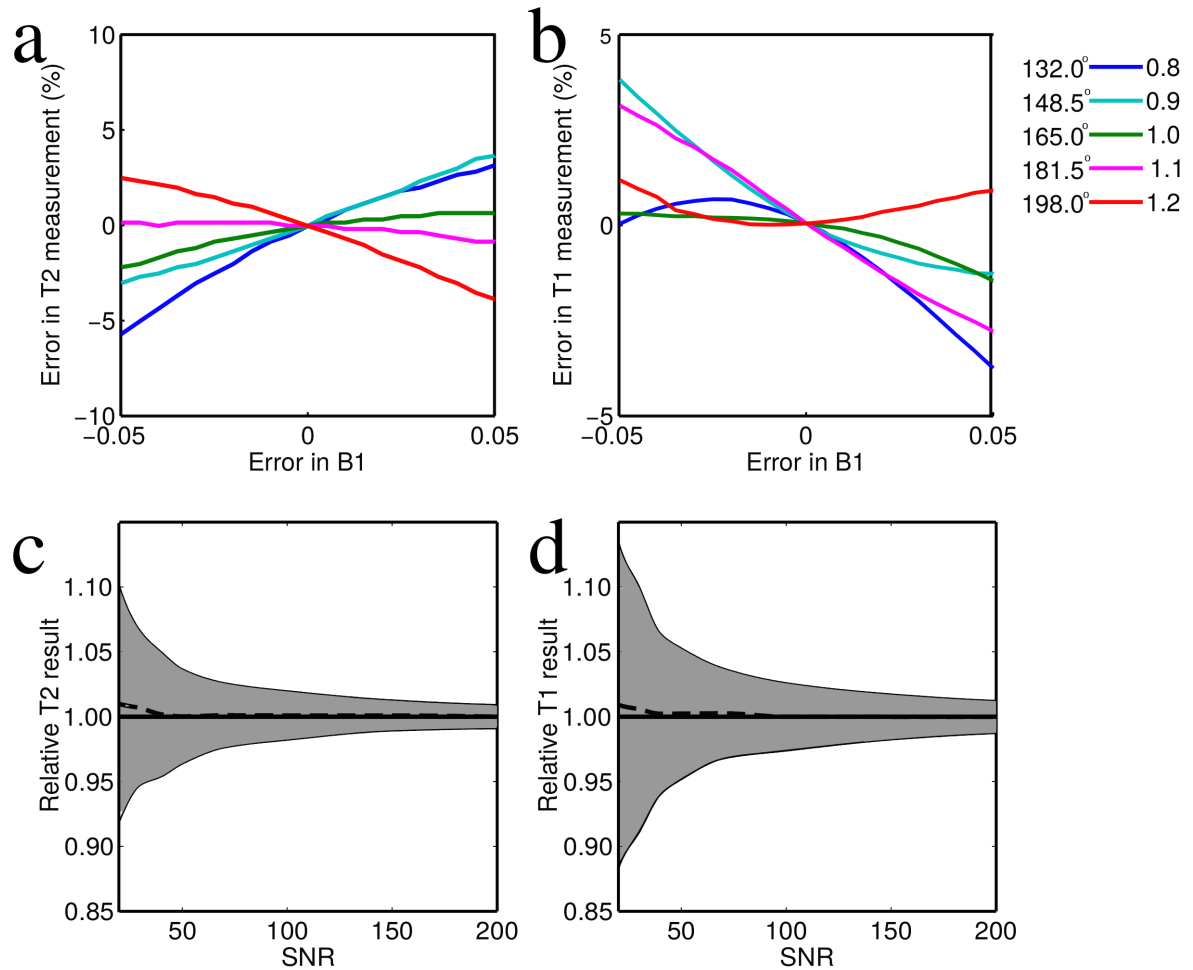
Figure 5.7: (a-b) Fitting of simulated PD-T2 and T1w image intensities with T1 = 1s, T2 = 60 ms, and a range of B1 show how the input of erroneous B1 values into the fitting algorithm results in erroneous (a) T2 and (T1) values. (c-d) Relative mean standard deviation in T2 (c) and T1 (d) fit results from simulated PD-T2 and T1w signal intensities with added Gaussian complex noise for a range of signal to noise ratios (T1 = 1s, T2 = 60 ms, refocussing angle = 165°).

could be eliminated by moving to 3D imaging, which is becoming more common [27, 28]. These 3D TSE scans use very long echo trains, and often make use of variable refocusing flip angles and short inter-echo spacings via non-selective excitation to minimize blurring effects.

FLAIR images in place of standard T1-weighted images gave poorer results with reduced accuracy for T1. The long echo time and the long inversion time, result in mixed T1 and T2 weighting which limits the ability of FLAIR to discriminate between

T1 and T2 contrast. FLAIR images with reduced echo times, or inversion recovery images with reduced inversion time would be of greater value for relaxation mapping, yet are not standard in clinical exams. For example, QRAPMASTER [19, 20] employs multiple inversion times and echo times for simultaneous T1 and T2 quantification.

Simulations show that the typical SNR of the acquired data was sufficient for precision within 5%, and that the T1 and T2 mapping are relatively insensitive to small errors ($\leq$ 0.05) in B1 value. However, lower prescribed refocussing values would result in increased sensitivity to B1 errors. T2 estimates from the TSE data were typically lower than values from the MESE experiment. Based on simulation results, we conclude that this is likely due to small errors in the B1 measurement rather than noise.

The three point T1 and T2 fit does not and cannot account for multi-component T1 or T2 relaxation. While the T2 measurement appears relatively insensitive to T1, the assumption of single component T2 can impact the T1 measurement, particularly when using the T2w FLAIR, since a single component T2 estimate is insufficient to unravel the mixed T1 and T2-weighted contrast. Further, incidental MT may not impact individual T2 components equally [26, 29] and magnetization transfer will depend on timing between slices [26], which varies between FLAIR, T1w and PD-T2 sequences. Multiple component relaxation demands use of advanced sequences that are not part of standard clinical protocols. Here our goal is to estimate single component parameters from standard radiology sequences. If time is not limited, we still recommend full inversion recovery or multiple echo experiments for single component T1 or T2 mapping respectively. However, the need for these specializes sequences has led to minimal impact of quantitative relaxation mapping in clinical settings to date. Using the methods proposed here, standard sequences can be converted into quantitative maps.

This work makes use of PD-weighted images, achieved through dual echo TSE. While PD images were commonly used in historical brain protocols, and remain common in clinical research, they are often not used in modern clinical brain exams, though still common in some regions of the body such as spine and cartilage imaging. Thus the addition of PD weighting may be perceived as a limitation of this work. However dual echo use of PD-T2 can be achieved with only moderate time increase over standard T2.

124

Finally, this work required the addition of a flip angle map which was is also non-standard in the clinic. Nevertheless since B1 varies slowly across the brain, a rapid technique requiring only 33 seconds was used. In the future, it may be possible to predict the B1 without need for an actual map [3].

5.5 Conclusions

In conclusion, Bloch modelling of TSE sequences allows for T1 and T2 relaxation measurements from only PD, T2 and T1-weighted TSE images. By the incorporation of a measured B1 map, fitting of T1 and T2 may be achieved from only three points. A T1w TSE image is preferred over a T2w-FLAIR for T1 estimation. The best results were achieved in single slice acquisitions. Accuracy in T1 is reduced in multi-slice acquisitions due to cross talk and incidental MT variation between sequences which needs to be managed. Accuracy in T2 was unaffected by variations in incidental MT. When variation in incidental MT across sequences is reduced, this method enables reasonably accurate relaxation quantification without the need for specialized sequences, by utilizing existing weighted images and measured flip angles.

Acknowledgements

References

[1] Sean C.L. Deoni. Quantitative Relaxometry of the Brain. *Topics in magnetic resonance imaging : TMRI*, 21(2):101–113, April 2010.

[2] A.L. MacKay, I.M. Vavasour, A. Rauscher, S.H. Kolind, B. M adler, G.R.W. Moore, A.L. Traboulsee, D.K.B. Li, and C. Laule. MR Relaxation in Multiple Sclerosis. *Neuroimaging Clinics of North America*, 19(1):1–26, February 2009.

[3] Md. Nasir Uddin, Kelly C. McPhee, Gregg Blevins, and Alan H. Wilman. Recovery of accurate T2 from historical 1.5 tesla proton density and T2-weighted images: Application to 7-year T2 changes in multiple sclerosis brain. *Magnetic Resonance Imaging*, 37:21–26, April 2017.

[4] Andrew J. Walsh, R. Marc Lebel, Amir Eissa, Gregg Blevins, Ingrid Catz, Jian-Qiang Lu, Lothar Resch, Edward S. Johnson, Derek J. Emery, Kenneth G. Warren, and Alan H. Wilman. Multiple Sclerosis: Validation of MR Imaging for Quantification and Detection of Iron. *Radiology*, 267(2):531–542, May 2013.

[5] José M. Alústiza, José Artetxe, Agustín Castiella, Cristina Agirre, José I. Emparanza, Pedro Otazua, Manuel García-Bengoechea, Jess Barrio, Fernando Mjica, and José A. Recondo. MR Quantification of Hepatic Iron Concentration1. *Radiology*, 230(2):479–484, February 2004.

[6] Timothy C. Dunn, Ying Lu, Hua Jin, Michael D. Ries, and Sharmila Majumdar. T2 Relaxation Time of Cartilage at MR Imaging: Comparison with Severity of Knee Osteoarthritis. *Radiology*, 232(2):592–598, August 2004.

[7] Nilesh R. Ghugre, Thomas D. Coates, Marvin D. Nelson, and John C. Wood. Mechanisms of Tissue-Iron Relaxivity: Nuclear Magnetic Resonance Studies of Human Liver Biopsy Specimens. *Magnetic resonance in medicine : official journal of the*

Society of Magnetic Resonance in Medicine / Society of Magnetic Resonance in Medicine, 54(5):1185–1193, November 2005.

[8] Shivraman Giri, Yiu-Cho Chung, Ali Merchant, Georgeta Mihai, Sanjay Rajagopalan, Subha V. Raman, and Orlando P. Simonetti. T2 quantification for improved detection of myocardial edema. *Journal of Cardiovascular Magnetic Resonance*, 11(1), December 2009.

[9] Ke Li, Richard D. Dortch, E. Brian Welch, Nathan D. Bryant, Amanda K.W. Buck, Theodore F. Towse, Daniel F. Gochberg, Mark D. Does, Bruce M. Damon, and Jane H. Park. Multi-parametric MRI characterization of healthy human thigh muscles at 3.0T - relaxation, magnetization transfer, fatwater, and diffusion tensor imaging. *NMR in biomedicine*, 27(9):1070–1084, September 2014.

[10] Stephen J. Matzat, Emily J. McWalter, Feliks Kogan, Weitian Chen, and Garry E. Gold. T2 Relaxation time quantitation differs between pulse sequences in articular cartilage. *Journal of Magnetic Resonance Imaging*, pages n/a–n/a, 2014.

[11] David Verhaert, Paaladinesh Thavendiranathan, Shivraman Giri, Georgeta Mihai, Sanjay Rajagopalan, Orlando P. Simonetti, and Subha V. Raman. Direct T2 Quantification of Myocardial Edema in Acute Ischemic Injury. *JACC: Cardiovascular Imaging*, 4(3):269–278, March 2011.

[12] Corinna M Bauer, Hernan Jara, and Ron Killiany. Whole brain quantitative T2 MRI across multiple scanners with dual echo FSE: Applications to AD, MCI, and normal aging. *NeuroImage*, 52(2):508–514, August 2010.

[13] Kelly C. McPhee and Alan H. Wilman. T2 quantification from only proton density and T2-weighted MRI by modelling actual refocusing angles. *NeuroImage*, 118:642–650, September 2015.

[14] Amanda F. Mejia, Elizabeth M. Sweeney, Blake Dewey, Govind Nair, Pascal Sati, Colin Shea, Daniel S. Reich, and Russell T. Shinohara. Statistical estimation of

T1 relaxation times using conventional magnetic resonance imaging. *NeuroImage*, 133:176–188, June 2016.

[15] Jesse I. Hamilton, Yun Jiang, Yong Chen, Dan Ma, Wei-Ching Lo, Mark Griswold, and Nicole Seiberlich. MR fingerprinting for rapid quantification of myocardial T1, T2, and proton spin density. *Magnetic Resonance in Medicine*, 77(4):1446–1458, April 2017.

[16] Dan Ma, Vikas Gulani, Nicole Seiberlich, Kecheng Liu, Jeffrey L. Sunshine, Jeffrey L. Duerk, and Mark A. Griswold. Magnetic resonance fingerprinting. *Nature*, 495(7440):187–192, March 2013.

[17] Sean C.L. Deoni, Brian K. Rutt, and Terry M. Peters. Rapid combined T1 and T2 mapping using gradient recalled acquisition in the steady state. *Magnetic Resonance in Medicine*, 49(3):515–526, March 2003. 00316.

[18] Sean C. L. Deoni, Terry M. Peters, and Brian K. Rutt. High-resolution T1 and T2 mapping of the brain in a clinically acceptable time with DESPOT1 and DESPOT2. *Magnetic Resonance in Medicine*, 53(1):237–241, January 2005. 00148.

[19] J.b.m. Warntjes, O. Dahlqvist, and P. Lundberg. Novel method for rapid, simultaneous T1, T*2, and proton density quantification. *Magnetic Resonance in Medicine*, 57(3):528–537, March 2007.

[20] J.B.M. Warntjes, O. Dahlqvist Leinhard, J. West, and P. Lundberg. Rapid magnetic resonance quantification on the brain: Optimization for clinical usage. *Magnetic Resonance in Medicine*, 60(2):320–329, August 2008.

[21] Stuart Clare and Peter Jezzard. Rapid T1 mapping using multislice echo planar imaging. *Magnetic Resonance in Medicine*, 45(4):630–634, April 2001.

[22] European Society of Radiology. Magnetic Resonance Fingerprinting - a promising new approach to obtain standardized imaging biomarkers from MRI. *Insights into Imaging*, 6(2):163–165, April 2015.

[23] Greg J. Stanisz, Ewa E. Odrobina, Joseph Pun, Michael Escaravage, Simon J. Graham, Michael J. Bronskill, and R. Mark Henkelman. T1, T2 relaxation and magnetization transfer in tissue at 3t. *Magnetic Resonance in Medicine*, 54(3):507–512, 2005. 00545.

[24] Kelly C. McPhee and Alan H. Wilman. Transverse relaxation and flip angle mapping: Evaluation of simultaneous and independent methods using multiple spin echoes. *Magnetic Resonance in Medicine*, 77(5):2057–2065, May 2017.

[25] J. Pauly, P. Le Roux, Dwight Nishimura, and A. Macovski. Parameter relations for the Shinnar-Le Roux selective excitation pulse design algorithm [NMR imaging]. *IEEE Transactions on Medical Imaging*, 10(1):53–65, 1991.

[26] Irene M. Vavasour, Kenneth P. Whittall, David K.B. Li, and Alex L. MacKay. Different magnetization transfer effects exhibited by the short and long T2 components in human brain. *Magnetic Resonance in Medicine*, 44(6):860–866, 2000.

[27] M. Kitajima, T. Hirai, Y. Shigematsu, H. Uetani, K. Iwashita, K. Morita, M. Komi, and Y. Yamashita. Comparison of 3d FLAIR, 2d FLAIR, and 2d T2-Weighted MR Imaging of Brain Stem Anatomy. *American Journal of Neuroradiology*, 33(5):922–927, May 2012.

[28] John P. Mugler. Optimized three-dimensional fast-spin-echo MRI. *Journal of Magnetic Resonance Imaging*, 39(4):745–767, April 2014. 00073.

[29] Yongmin Chang, Sung Jin Bae, Young Ju Lee, Moon Jung Hwang, Sang Heun Lee, Jongmin Lee, Sang Kwon Lee, and Seongku Woo. Incidental magnetization transfer effects in multislice brain MRI at 3.0t. *Journal of Magnetic Resonance Imaging*, 25(4):862–865, April 2007.

Chapter 6

Conclusions

6.1 Summary of Findings

Multi-echo spin echo (MESE) methods are the gold standard for T2 quantification in vivo. In practical imaging situations, precise 180° refocusing angles are impractical or impossible to achieve. Imperfect slice profiles, radio frequency (RF) interference, and potentially purposeful reduction in refocusing angles can all contribute to this problem. Imperfect refocusing results in indirect and stimulated echo contamination, resulting in non-exponential decay, precluding exponential fitting. Methods for fitting for T2 while accounting for imperfect refocusing exist and are available. Generally, the simulation model falls into one of two categories: Bloch equation simulations, or the extended phase graph (EPG). In Chapter 2, Bloch and EPG methods for Indirect and Stimulated Echo Compensation (ISEC) fitting of slice selective MESE data are compared. In addition to differences between methods, the inclusion of flip angle as a fitting parameter and the use of separately measured values was examined. EPG employs estimates of slice profile. A Fourier transform approach has been previously proposed [1], and a Shinnar-Le Roux (SLR) simulation approach was demonstrated here. Simulated slice selective decay curves vary substantially between models and are not symmetric about 180° refocusing values (symmetry exists for non-selective pulses, and was assumed in previous work [1]). Differences in the simulated decay curves arise primarily from differences in the modelling of RF profile response. EPG_{FT} (EPG using FT slice profile approximation)

provides highly inaccurate flip angles, and use of SLR slice profiles with EPG (EPG$_{SLR}$) provides only minor improvement. Consequently, providing measured flip angles to EPG methods yields erroneous T2 values, and this two parameter fitting approach (amplitude and T2) is not recommended. Three parameter (T2, B1 and amplitude) EPG fitting yields systematically different, but very similar T2 results, compared to Bloch based methods. In contrast, provision of accurate flip angles to the Bloch modelling approach yields accurate T2 values, and avoids effects of multiple solutions with refocusing angles above and below 180°, especially in cases of low SNR. When available, the more complex Bloch fitting approach is preferred over EPG. However, the much simpler EPG approach can still provide excellent T2 results in most cases.

Despite the availability of T2 fitting methods which account for indirect and stimulated echoes, exponential fitting methods remain persistent. Researchers frequently discard echoes with the assumption that improved fit quality means improved accuracy. In Chapter 3, exponential fitting skipping the first echo or all odd echoes was examined for a wide range of T2 and flip angle values, and for a range of echo train lengths. Skipped echo exponential fitting schemes can make substantial improvements in accuracy of T2 values, over fitting of all echoes, particularly where a short echo train is used. However, these methods are insufficient for avoiding stimulated echo contamination in MESE T2 fitting. Error in T2 fitting using skipped echo approaches yielded a highly variable error that is flip angle, T2 and echo train length dependent. Errors in T2 were highest when refocusing angles deviated from 180°. Modelling approaches, as described in Chapter 2, are recommended over the use of exponential fitting.

Multi-echo spin echo sequences are time consuming, which limits availability in research, and precludes use in the clinic. Weighted images are frequently acquired in the clinic and in research studies. Particularly the T2-weighted Fast Spin Echo (FSE) is typically included in most clinical brain exams. In Chapter 4 it was demonstrated that ISEC fitting with Bloch modelling approach allows for accurate T2 fitting of a PD and T2-weighted FSE image when flip angles are available. By incorporating actual refocusing angles into the fitting process, ISEC fitting achieves a two point fit while providing much greater accuracy and less sensitivity to refocusing pulse shape than exponential fit-

ting (T2 was overestimated by 33 - 112%, depending on chosen echo times, as expected from simulations). Values from human brain experiments at 4.7T agreed within 4% of 32 echo MESE methods. Phantom experiments provided values which agreed within the measurement certainty to spin echo experiments. While MESE methods are preferred, when available, the described methods permits extraction of accurate T2 values without additional imaging time.

The addition of a T1-weighted image to the PD-T2 weighted protocol allows for simultaneous extraction of T1 and T2. The use of a T1w FSE, or a T2w-FLAIR (FLuid Attenuated Inversion Recovery), for this purpose were examined in Chapter 5. Single slice acquisitions of PD-T2 and T1w images provided T1 values were within 7% of gold standard in grey matter and within 13% in white matter. Corresponding T2 values were within 5% in grey matter and 7% in white matter. Multi-slice acquisitions were less accurate. Contiguous acquisitions resulted in up to 30% difference in T1 values relative to inversion recovery. T2 values were less sensitive to acquisition and were not found to be significantly different across methods. In multi-slice acquisitions, differences in slice order between acquisitions result in different amounts of cross-talk and incidental magnetization transfer (MT) between acquisitions, reducing the accuracy of T1 estimation, relative to inversion recovery.

6.2   Limitations

Simulations in this work were based on pulse sequences used on three local MRI systems. Exact errors in T2 quantification will depend on the exact sequence used, parameters prescribed, and perhaps the tissue being examined (for example, white matter is known to exhibit multi-component T2, and the accuracy of characterizing it with a single exponential fit will be limited and sensitive to echo timing). This work only considers one inter-echo spacing at each field strength (generally, $\sim$10 ms). However, results may be scaled for any other inter-echo spacing by the ratio of echo spacing to T2. Only single component T2 is examined in this work. White matter voxels and partial volume effects would results in multiple T2 components. Constant T1 was assumed for MESE

fitting with indirect and stimulated echo compensation, and in the two point T2 fitting in Chapter 4. In cases with a large T1/T2 value (>10), this assumption will result in only very small errors in ISEC fitting [1]. Due to a range of T1 values in tissues, simulations examining differences in T2 values between models may not be exactly as simulation results presented. Echo amplitude simulations are most sensitive to T1 accuracy where there are large contributions from indirect and stimulated echoes, though any resulting T2 fit errors are expected to be small in comparison to differences in T2 values due to the fitting model.

The majority of this work considers nominal 180° refocussing angles. In general, the sensitivity of ISEC methods to errors in measured B1 or assumed T1 increase as the refocussing angle deviates further from 180°. Reduced refocussing angles are frequently employed in multi-echo sequences in order to maintain the desired number of imaging slices while staying within safety limits for RF heating. Compromises between slice coverage, echo train length, pulse shape and imaging time must often be made in order to remain within safety limits. The Gaussian pulse shapes employed in 4.7T experiments described in this work are used in order to reduce RF power. SAR (specific absorption rate) is proportional to B1^2. This results in pulse shapes with negative lobes, such as in truncated Sinc pulses, depositing more RF power to achieve the same flip angle as a simpler pulse shape without negative lobes (such as a Gaussian). If RF heating concerns could be ignored, pulse shapes could be optimized for slice profile, and stimulated echo contamination could be significantly reduced (though not entirely eliminated, since RF inhomogeneity would remain an issue).

Methods for two point fitting of T2, or three point fitting of T1 and T2 are less accurate than using dedicated relaxometry experiments. The exactly echo times (for PD and T2w images) and repetition times (for T1w) will limit the range of T1 and T2 values which the methods are sensitive to. These sequences are also more sensitive to noise, and to the accuracy of acquired B1 maps. When possible, prospective acquisition of dedicated experiments for measurement of T1 and T2 are preferred. Further, these methods do not and cannot account for multi-component T1 or T2 relaxation. While the T2 measurement appears relatively insensitive to T1, the assumption of single component

T2 can impact the T1 measurement, particularly when using the T2w FLAIR, since a single component T2 estimate is insufficient to unravel the mixed T1 and T2-weighted contrast.

Multi-slice FSE protocols for T1 and T2 fitting result in signal loss due to incidental magnetization transfer and cross-talk. Given differences in slice acquisition order between the T1w, T2-FLAIR, and PD-T2 protocols, these effects are unequal. Incidental MT will not equally affect different regions of the brain, due to variation in B1 and local tissue MT sensitivity [2]. Multi-slice data acquired with odd and even slices acquired in separate acquisitions minimize these MT differences compared to interleaved multi-slice acquisition of all contiguous slices, and should avoid most cross-talk between slices. Contiguous acquisitions may result in cross talk which cause the slice profile to differ from the simulation. Adjacent slices were not accounted for in steady state simulations. The acquisition of even and odd slices is non-standard, and there is risk of motion occurring between acquisitions. This acquisition also results in increased imaging time. In future, improved slice interleaving options could be implemented to further reduce incidental MT and cross talk. Alternatively, the issues with slice cross-talk and MT could be eliminated by moving to 3D imaging, which is becoming more common (for example, [3]).

The second half of this thesis is dedicated to extracting relaxometry information from standard weighted images. This has the advantage of acquiring quantitative measurements without dedicated relaxometry sequences and minimal additional imaging time. However, PD weighted images are not standard in all imaging protocols. Though a dual echo FSE image may be acquired with a minimal increased imaging time over a T2 weighted image and B1 maps may be acquired in less than 10 seconds, some clinicians may not be inclined to add the additional image which they will then have to view, nor feel that a T2 map is necessary. These methods will most likely be implemented in prospective clinical research, quantitative measurements are desired, but there is insufficient time available. Prospective acquisition of weighted images and a B1 map such that it is possible to produce accurate and reproducible relaxation maps from clinical data sets open the door to collaborations such that clinicians and researchers may find new roles for quantitative MR in the clinic. Relaxation maps have the advantage of

removing image non-uniformities due to coil sensitivity, B1 in homogeneity, and nuisance parameters, such as gain. As 3T imaging increases in popularity, clinicians may find that techniques which avoid image inhomogeneities, which are increased at higher field, more desirable.

The accuracy of in vivo relaxometry measurements is ultimately limited by the fact that data is being acquired on a living, breathing subject, not on uniform samples in test tubes. While long scan times with many averages can result in high SNR, this is impractical for in vivo experiments. Ultimately, scan times must be practical, and subjects move, creating motion artefacts or resulting in differences in orientation and slice positions between images. Motion can be a particular issue for long scans, or long protocols, and subjects who are sick or injured may not be capable of staying still for long periods of time. Noise, artefacts, mis-registration between images used for fitting, and differences between positioning and ROI selection can all limit accuracy and/or reproducibility of T1 and T2 measurements. Further, biological tissues are non-uniform. Many biological tissues exhibit multi-component T1 and T2 decay due to tissue properties or partial volume effects. Multi-component relaxation is not considered in this thesis, but could result in additional biases in T1 and T2 results. Errors or biases in fitting results would depend on scan parameters including choice of TE, TR, or inversion times, particularly where only a few data points are used to determine relaxation times. All of these potential sources of error would be in addition to limitations of the sequence modelling or flip angle mapping, as discussed throughout this thesis. Ultimately the aim of this work is to limit errors inherent in the fitting model such that, even with the additional challenges of in vivo imaging, relaxation parameters are sufficiently accurate to provide useful comparison between groups, or changes over time in individuals or groups. A practical scan-rescan reproducibility goal would be within 5%.

6.3 Future Directions

There is a demand for rapid acquisition of quantitative MR parameters, as demonstrated by the rapid rise in popularity of fingerprinting. The use of *big data* is also becoming a

topic of interest [4]. In particular, weighted images are frequently acquired in the clinic and in research, and the question of how that data may be used quantitatively is of interest in the research community [4–6]. Future work related to this project primarily include optimization of the T1 protocol, the prospective addition of developed methods into ongoing studies, and retrospective application of the developed methods to existing data sets.

The three point FSE T1 and T2 fitting protocol requires optimization to improve the accuracy with multi-slice acquisitions, and to reduce imaging time, such that it may be implemented into future imaging protocols. This may require customization of the sequence. Further, there is potential for use of 3D acquisitions to avoid incidental MT and cross talk. Standard 3D acquisitions are very slow and blurring reduces image quality. Recent developments such as the Siemens SPACE sequence [3] have resulted in rapid 3D images. These may be useful for parameter mapping, though the exact pulse sequences are not openly published.

Retrospective application of the presented method for acquiring T2 from dual echo FSE is an important next step. In particular, data from Amyotrophic Lateral Sclerosis patients and Multiple Sclerosis patients is available locally, and the Alzheimer's Disease Neuroimaging Initiative [7] database includes a large number of patients where PD-T2 data were acquired. Previously, researchers attempted to use exponential fitting for T2 quantification from this data and found systematic differences between scanners and across sites [6].

There is currently demand for rapid acquisition of quantitative MR parameters. Work to achieve this goal is currently a popular area of research. One such method for achieving this is Fingerprinting. Fingerprinting relies on rapid radial acquisition of many low SNR data points with semi-random variations in imaging parameters. Both Fingerprinting and the ISEC fitting approach presented in this thesis rely on pre-computed databases of simulated image intensities. However, the methods for fitting relaxation parameters from FSE images presented in this thesis are not Fingerprinting methods, and differ from Fingerprinting in that conventional images are acquired, measurements rely on only a few higher SNR data points, scan parameters are chosen purposefully, rather

than semi-randomly, and pattern matching was not employed. This avoids spatially specific artefacts, and allows clinicians to directly obtain the desired weighted images. Implementation of the developed PD-T2 protocol and acquisition of a rapid B1 map could allow for T2 quantification in ongoing clinical studies, with minimal time penalty.

Machine learning approaches are becoming more prevalent in medical imaging research, and could potentially be employed for either improved fitting of data, or interpretation of quantitative data. Perhaps training data sets looking at single vs multi-slice acquisitions could assist with removal of bias due to incidental MT, or to extract relaxation parameters given alternative groups of weighted images. For example, if training data contained B1, T1 and T2 maps, and a variety of weighted images, perhaps quantitative maps could be extracted, even where sequences were not simulated in detail, or the requirement of a B1 map could be removed.

Overall, the methods presented here may be implemented for the purpose of improving accuracy, reproducibility, and availability of relaxation mapping in both clinical and research settings. The described limitations of T1 and T2 methods may also allow future research to be better interpreted. The methods developed in this thesis for quantification of relaxation times from FSE images have potential for both retrospective analysis of existing data, and prospective acquisition of data. This has potential for use in both large scale databases, and smaller local research-clinical partnerships. The ISEC approach for fitting MESE data could also allow for combination of data across multiple sites, where differences in scanners and pulse sequences may have previously prevented comparison of data due to variable amounts of indirect and stimulated echo contamination, and thus systematic biases between data sets.

References

[1] R. Marc Lebel and Alan H. Wilman. Transverse relaxometry with stimulated echo compensation. *Magnetic Resonance in Medicine*, 64(4):1005–1014, 2010.

[2] Irene M. Vavasour, Kenneth P. Whittall, David K.B. Li, and Alex L. MacKay. Different magnetization transfer effects exhibited by the short and long T2 components in human brain. *Magnetic Resonance in Medicine*, 44(6):860–866, 2000.

[3] John P. Mugler. Optimized three-dimensional fast-spin-echo MRI. *Journal of Magnetic Resonance Imaging*, 39(4):745–767, April 2014. 00073.

[4] White Matter Study Group. White Matter Study Group Meeting. In *Proceedings of ISMRM*, volume 25, April 2017.

[5] Amanda F. Mejia, Elizabeth M. Sweeney, Blake Dewey, Govind Nair, Pascal Sati, Colin Shea, Daniel S. Reich, and Russell T. Shinohara. Statistical estimation of T1 relaxation times using conventional magnetic resonance imaging. *NeuroImage*, 133:176–188, June 2016.

[6] Corinna M Bauer, Hernan Jara, and Ron Killiany. Whole brain quantitative T2 MRI across multiple scanners with dual echo FSE: Applications to AD, MCI, and normal aging. *NeuroImage*, 52(2):508–514, August 2010.

[7] Alzheimer's Disease Neuroimaging Initiative. Alzheimer's disease neuroimaging initiative. `http://adni.loni.usc.edu/`, 2014. Accessed 2014-04-03.

Bibliography

José M. Alústiza, José Artetxe, Agustín Castiella, Cristina Agirre, José I. Emparanza, Pedro Otazua, Manuel García-Bengoechea, Jess Barrio, Fernando Mjica, and José A. Recondo. MR Quantification of Hepatic Iron Concentration1. *Radiology*, 230(2):479–484, February 2004. doi: 10.1148/radiol.2302020820.

A. Amirabadi, L. Vidarsson, E. Miller, M. S. Sussman, K. Patil, H. Gahunia, S. A. F. Peel, A. Zhong, R. Weiss, G. Detzler, H. L. M. Cheng, R. Moineddin, and A. S. Doria. USPIO-related T1 and T2 mapping MRI of cartilage in a rabbit model of blood-induced arthritis: a pilot study. *Haemophilia*, 21(1):e59–e69, January 2015. doi: 10.1111/hae.12601.

Ishu Arpan, Sean C. Forbes, Donovan J. Lott, Claudia R. Senesac, Michael J. Daniels, William T. Triplett, Jasjit K. Deol, H. Lee Sweeney, Glenn A. Walter, and Krista Vandenborne. T2 mapping provides multiple approaches for the characterization of muscle involvement in neuromuscular diseases: a cross-sectional study of lower leg muscles in 515-year-old boys with Duchenne muscular dystrophy. *NMR in Biomedicine*, 26(3):320–328, March 2013. doi: 10.1002/nbm.2851.

Bettina Baeßler, Frank Schaarschmidt, Christian Stehning, Bernhard Schnackenburg, Agathe Giolda, David Maintz, and Alexander C. Bunck. Reproducibility of three different cardiac T2-mapping sequences at 1.5t. *Journal of Magnetic Resonance Imaging*, 44(5):1168–1178, November 2016. doi: 10.1002/jmri.25258.

G. Bartzokis, D. Sultzer, J. Cummings, L. E. Holt, D. B. Hance, V. W. Henderson, and J. Mintz. In vivo evaluation of brain iron in Alzheimer disease using magnetic resonance imaging. *Archives of General Psychiatry*, 57(1):47–53, January 2000. doi: 10.1001/archpsyc.57.1.47.

George Bartzokis, Mace Beckson, Darwood B. Hance, Peter Marx, Jennifer A. Foster, and Stephen R. Marder. MR evaluation of age-related increase of brain iron in young adult and older normal males. *Magnetic Resonance Imaging*, 15(1):29–35, January 1997. doi: 10.1016/S0730-725X(96)00234-2.

Corinna M Bauer, Hernan Jara, and Ron Killiany. Whole brain quantitative T2 MRI across multiple scanners with dual echo FSE: Applications to AD, MCI, and normal aging. *NeuroImage*, 52(2):508–514, August 2010. doi: 10.1016/j.neuroimage.2010.04. 255.

Sonja Bauer, Marlies Wagner, Alexander Seiler, Elke Hattingen, Ralf Deichmann, Ulrike Nöth, and Oliver C. Singer. Quantitative T2-Mapping in Acute Ischemic. *Stroke*, 45 (11):3280–3286, November 2014. doi: 10.1161/STROKEAHA.114.006530.

Mehdi Behroozi, Caroline Chwiesko, Felix Str ockens, Magdalena Sauvage, Xavier Helluy, Jutta Peterburs, and Onur G unt urk un. In vivo measurement of T1 and T2 relaxation times in awake pigeon and rat brains at 7t. *Magnetic Resonance in Medicine*, page In Press, May 2017. doi: 10.1002/mrm.26722.

Noam Ben-Eliezer. EMC Based T2-Mapping Package | CAI2r. http://cai2r.net/resources/software/emc-based-t2-mapping-package, 2015. Accessed 2017-09-28.

Noam Ben-Eliezer, Daniel K. Sodickson, and Kai Tobias Block. Rapid and accurate T $_2$ mapping from multi-spin-echo data using Bloch-simulation-based reconstruction: Mapping Using Bloch-Simulation-Based Reconstruction. *Magnetic Resonance in Medicine*, 73(2):809–817, 2015. doi: 10.1002/mrm.25156.

Luca Biasiolli, Alistair C Lindsay, Joshua T Chai, Robin P Choudhury, and Matthew D Robson. In-vivo quantitative T2 mapping of carotid arteries in atherosclerotic patients: segmentation and T2 measurement of plaque components. *Journal of Cardiovascular Magnetic Resonance*, 15(1):69, August 2013. doi: 10.1186/1532-429X-15-69.

N. Bloembergen, E. M. Purcell, and R. V. Pound. Relaxation Effects in Nuclear Magnetic Resonance Absorption. *Physical Review*, 73(7):679, April 1948. doi: 10.1103/PhysRev. 73.679. 05294.

Mustapha Bouhrara and Jean-Marie Bonny. B1 mapping with selective pulses. *Magnetic Resonance in Medicine*, 68(5):1472–1480, November 2012. doi: 10.1002/mrm.24146.

Dylan Breitkreutz, Kelly C McPhee, and Alan H. Wilman. Value of Independent Flip Angle Mapping for Transverse Relaxometry with Stimulated Echo Compensation. In *Proceedings of ISMRM 21*, page 2466, Salt Lake City, Utah, USA, 2013.

H. Y. Carr and E. M. Purcell. Effects of Diffusion on Free Precession in Nuclear Magnetic Resonance Experiments. *Physical Review*, 94(3):630–638, May 1954. doi: 10.1103/ PhysRev.94.630. 04664.

Yongmin Chang, Sung Jin Bae, Young Ju Lee, Moon Jung Hwang, Sang Heun Lee, Jongmin Lee, Sang Kwon Lee, and Seongku Woo. Incidental magnetization transfer effects in multislice brain MRI at 3.0t. *Journal of Magnetic Resonance Imaging*, 25 (4):862–865, April 2007. doi: 10.1002/jmri.20867.

Stuart Clare and Peter Jezzard. Rapid T1 mapping using multislice echo planar imaging. *Magnetic Resonance in Medicine*, 45(4):630–634, April 2001. doi: 10.1002/mrm.1085.

A. P. Crawley and R. M. Henkelman. Errors in T2 estimation using multislice multiple-echo imaging. *Magnetic Resonance in Medicine*, 4(1):34–47, January 1987. doi: 10. 1002/mrm.1910040105.

Marion de Roquefeuil, Pierre-André Vuissoz, Jean-Marie Escanyé, and Jacques Fel-blinger. Effect of physiological Heart Rate variability on quantitative T2 mea-surement with ECG-gated Fast Spin Echo (FSE) sequence and its retrospective

correction. *Magnetic Resonance Imaging*, 31(9):1559–1566, November 2013. doi: 10.1016/j.mri.2013.06.006.

Sean C. L. Deoni, Terry M. Peters, and Brian K. Rutt. High-resolution T1 and T2 mapping of the brain in a clinically acceptable time with DESPOT1 and DESPOT2. *Magnetic Resonance in Medicine*, 53(1):237–241, January 2005. doi: 10.1002/mrm.20314. 00148.

Sean C. L. Deoni, Evelyne Mercure, Anna Blasi, David Gasston, Alex Thomson, Mark Johnson, Steven C. R. Williams, and Declan G. M. Murphy. Mapping Infant Brain Myelination with Magnetic Resonance Imaging. *Journal of Neuroscience*, 31(2):784–791, January 2011. doi: 10.1523/JNEUROSCI.2106-10.2011.

Sean C.L. Deoni. Transverse relaxation time (T2) mapping in the brain with off-resonance correction using phase-cycled steady-state free precession imaging. *Journal of Magnetic Resonance Imaging*, 30(2):411–417, August 2009. doi: 10.1002/jmri.21849.

Sean C.L. Deoni. Quantitative Relaxometry of the Brain. *Topics in magnetic resonance imaging : TMRI*, 21(2):101–113, April 2010. doi: 10.1097/RMR.0b013e31821e56d8.

Sean C.L. Deoni, Brian K. Rutt, and Terry M. Peters. Rapid combined T1 and T2 mapping using gradient recalled acquisition in the steady state. *Magnetic Resonance in Medicine*, 49(3):515–526, March 2003. doi: 10.1002/mrm.10407. 00316.

R. J. Dolan, A. M. Poynton, P. K. Bridges, and M. R. Trimble. Altered magnetic resonance white-matter T1 values in patients with affective disorder. *The British Journal of Psychiatry*, 157(1):107–110, July 1990. doi: 10.1192/bjp.157.1.107.

Timothy C. Dunn, Ying Lu, Hua Jin, Michael D. Ries, and Sharmila Majumdar. T2 Relaxation Time of Cartilage at MR Imaging: Comparison with Severity of Knee Osteoarthritis. *Radiology*, 232(2):592–598, August 2004. doi: 10.1148/radiol.2322030976.

N. K. Focke, G. Helms, P. M. Pantel, S. Scheewe, M. Knauth, C. G. Bachmann, J. Ebentheuer, P. Dechent, W. Paulus, and C. Trenkwalder. Differentiation of Typical and

Atypical Parkinson Syndromes by Quantitative MR Imaging. *American Journal of Neuroradiology*, 32(11):2087–2092, December 2011. doi: 10.3174/ajnr.A2865.

Alexander G. Gardener, Susan T. Francis, Malcolm Prior, Andrew Peters, and Penny A. Gowland. Dependence of blood R2 relaxivity on CPMG echo-spacing at 2.35 and 7 T. *Magnetic Resonance in Medicine*, 64(4):967–974, October 2010. doi: 10.1002/mrm. 22575.

Neil Gelman, Jay M. Gorell, Peter B. Barker, Ralph M. Savage, Eric M. Spickler, Joseph P. Windham, and Robert A. Knight. MR Imaging of Human Brain at 3.0 T: Preliminary Report on Transverse Relaxation Rates and Relation to Estimated Iron Content. *Radiology*, 210(3):759–767, March 1999.

Nilesh R. Ghugre, Thomas D. Coates, Marvin D. Nelson, and John C. Wood. Mechanisms of Tissue-Iron Relaxivity: Nuclear Magnetic Resonance Studies of Human Liver Biopsy Specimens. *Magnetic resonance in medicine : official journal of the Society of Magnetic Resonance in Medicine / Society of Magnetic Resonance in Medicine*, 54(5):1185–1193, November 2005. doi: 10.1002/mrm.20697.

Nilesh R. Ghugre, Cathleen M. Enriquez, Ignacio Gonzalez, Marvin D. Nelson, Thomas D. Coates, and John C. Wood. MRI detects myocardial iron in the human heart. *Magnetic Resonance in Medicine*, 56(3):681–686, September 2006. doi: 10.1002/mrm.20981.

Peter Gibbs, Daniel J. Tozer, Gary P. Liney, and Lindsay W. Turnbull. Comparison of quantitative T2 mapping and diffusion-weighted imaging in the normal and pathologic prostate. *Magnetic Resonance in Medicine*, 46(6):1054–1058, 2001. doi: 10.1002/mrm. 1298.

Shivraman Giri, Yiu-Cho Chung, Ali Merchant, Georgeta Mihai, Sanjay Rajagopalan, Subha V. Raman, and Orlando P. Simonetti. T2 quantification for improved detection of myocardial edema. *Journal of Cardiovascular Magnetic Resonance*, 11(1), December 2009. doi: 10.1186/1532-429X-11-56.

John C. Gore and Richard Kennan. Chapter 3: Physical and Physiological Basis of Magnetic Relaxation. In *Magnetic Resonance Imaging*. Mosby, 1999.

David J. Griffiths. *Introduction to Quantum Mechanics*. Pearson, Upper Saddle River, NJ, 2 edition edition, March 2004.

E. Mark Haacke, Robert W. Brown, Michael R. Thompson, and Ramesh Venkatesan. *Magnetic Resonance Imaging: Physical Principles and Sequence Design*. Wiley-Liss, 1st edition, June 1999.

E. L. Hahn. Spin Echoes. *Physical Review*, 80(4):580–594, November 1950. doi: 10.1103/ PhysRev.80.580.

B. Hallgren and P. Sourander. THE EFFECT OF AGE ON THE NON-HAEMIN IRON IN THE HUMAN BRAIN. *Journal of Neurochemistry*, 3(1):41–51, 1958. doi: 10.1111/ j.1471-4159.1958.tb12607.x.

Jesse I. Hamilton, Yun Jiang, Yong Chen, Dan Ma, Wei-Ching Lo, Mark Griswold, and Nicole Seiberlich. MR fingerprinting for rapid quantification of myocardial T1, T2, and proton spin density. *Magnetic Resonance in Medicine*, 77(4):1446–1458, April 2017. doi: 10.1002/mrm.26216.

Brian Hargreaves. Bloch Equation Simulator. http://www-mrsrl.stanford.edu/ brian/blochsim/, 2003. URL `http://www-mrsrl.stanford.edu/~brian/blochsim/`. Date Accessed: 2016-04-08.

Khader M. Hasan, Christopher Halphen, Arash Kamali, Flavia M. Nelson, Jerry S. Wolinsky, and Ponnada A. Narayana. Caudate Nuclei Volume, Diffusion Tensor Metrics, and T2 Relaxation in Healthy Adults and Relapsing-Remitting Multiple Sclerosis Patients: Implications to Understanding Gray Matter Degeneration. *Journal of magnetic resonance imaging : JMRI*, 29(1):70–77, January 2009. doi: 10.1002/jmri.21648.

Khader M. Hasan, Indika S. Walimuni, Larry A. Kramer, and Richard E. Frye. Human brain atlas-based volumetry and relaxometry: Application to healthy development

and natural aging. *Magnetic Resonance in Medicine*, 64(5):1382–1389, 2010. doi: 10.1002/mrm.22515.

Lili He and Nehal A. Parikh. Automated detection of white matter signal abnormality using T2 relaxometry: application to brain segmentation on term MRI in very preterm infants. *NeuroImage*, 64:328–340, January 2013. doi: 10.1016/j.neuroimage.2012.08.081.

J Hennig. Multiecho Imaging Sequence with Low Refocusing Flip Angles. *J. Magn. Reson.*, 78:397, 1988. doi: 10.1016/0022-2364(88)90128-X.

J. Hennig, A. Nauerth, and H. Friedburg. RARE imaging: A fast imaging method for clinical MR. *Magnetic Resonance in Medicine*, 3(6):823–833, December 1986. doi: 10.1002/mrm.1910030602.

Jürgen Hennig. Echoes - how to generate, recognize, use or avoid them in MR-imaging sequences. Part I: Fundamental and not so fundamental properties of spin echoes. *Concepts in Magnetic Resonance*, 3(3):125–143, 1991. doi: 10.1002/cmr.1820030302.

Diego Hernando, Yakir S Levin, Claude B Sirlin, and Scott B Reeder. Quantification of Liver Iron with MRI: State of the Art and Remaining Challenges. *Journal of magnetic resonance imaging : JMRI*, 40(5):1003–1021, November 2014. doi: 10.1002/jmri.24584.

Kelsey Herrmann, Bernadette O. Erokwu, Mette L. Johansen, James P. Basilion, Vikas Gulani, Mark A. Griswold, Chris A. Flask, and Susann M. Brady-Kalnay. Dynamic Quantitative T1 Mapping in Orthotopic Brain Tumor Xenografts. *Translational Oncology*, 9(2):147–154, April 2016. doi: 10.1016/j.tranon.2016.02.004.

Vít Herynek, Dita Wagnerová, Irena Hejlová, Monika Dezortov, and Milan Hájek. Changes in the brain during long-term follow-up after liver transplantation. *Journal of Magnetic Resonance Imaging*, 35(6):1332–1337, June 2012. doi: 10.1002/jmri.23599.

Chuan Huang, Ali Bilgin, Tomoe Barr, and Maria I. Altbach. T2 relaxometry with indirect echo compensation from highly undersampled data. *Magnetic Resonance in Medicine*, 70(4):1026–1037, 2013. doi: 10.1002/mrm.24540.

Chuan Huang, Maria I. Altbach, and Georges El Fakhri. Pattern recognition for rapid T2 mapping with stimulated echo compensation. *Magnetic Resonance Imaging*, 32(7): 969–974, September 2014. doi: 10.1016/j.mri.2014.04.014.

Alzheimer's Disease Neuroimaging Initiative. Alzheimer's disease neuroimaging initiative. `http://adni.loni.usc.edu/`, 2014. URL `http://adni.loni.usc.edu/`. Accessed 2014-04-03.

Clifford R Jack, Jr, Matt A Bernstein, Nick C Fox, Paul Thompson, Gene Alexander, Danielle Harvey, Bret Borowski, Paula J Britson, Jennifer L Whitwell, Chadwick Ward, Anders M Dale, Joel P Felmlee, Jeffrey L Gunter, Derek L G Hill, Ron Killiany, Norbert Schuff, Sabrina Fox-Bosetti, Chen Lin, Colin Studholme, Charles S DeCarli, Gunnar Krueger, Heidi A Ward, Gregory J Metzger, Katherine T Scott, Richard Mallozzi, Daniel Blezek, Joshua Levy, Josef P Debbins, Adam S Fleisher, Marilyn Albert, Robert Green, George Bartzokis, Gary Glover, John Mugler, and Michael W Weiner. The Alzheimer's Disease Neuroimaging Initiative (ADNI): MRI methods. *Journal of magnetic resonance imaging: JMRI*, 27(4):685–691, April 2008. doi: 10.1002/jmri.21049.

G. D. Jackson, A. Connelly, J. S. Duncan, R. A. Gr unewald, and D. G. Gadian. Detection of hippocampal pathology in intractable partial epilepsy: increased sensitivity with quantitative magnetic resonance T2 relaxometry. *Neurology*, 43(9):1793–1799, September 1993.

P Jezzard, S Duewell, and R S Balaban. MR relaxation times in human brain: measurement at 4 T. *Radiology*, 199(3):773–779, June 1996. doi: 10.1148/radiology.199.3. 8638004.

J. M. Jin, J. Chen, W. C. Chew, H. Gan, R. L. Magin, and P. J. Dimbylow. Computation of electromagnetic fields for high-frequency magnetic resonance imaging applications. *Physics in Medicine and Biology*, 41(12), December 1996. doi: 10.1088/0031-9155/41/ 12/011.

Hermien E. Kan, Tom W. J. Scheenen, Marielle Wohlgemuth, Dennis W. J. Klomp, Ivonne van Loosbroek-Wagenmans, George W. Padberg, and Arend Heerschap. Quantitative MR imaging of individual muscle involvement in facioscapulohumeral muscular dystrophy. *Neuromuscular Disorders*, 19(5):357–362, May 2009. doi: 10.1016/j.nmd. 2009.02.009.

Daniel Kim, Jens H. Jensen, Ed X. Wu, Sujit S. Sheth, and Gary M. Brittenham. Breathhold multiecho fast spin-echo pulse sequence for accurate R2 measurement in the heart and liver. *Magnetic Resonance in Medicine*, 62(2):300–306, August 2009. doi: 10.1002/mrm.22047.

M. Kitajima, T. Hirai, Y. Shigematsu, H. Uetani, K. Iwashita, K. Morita, M. Komi, and Y. Yamashita. Comparison of 3d FLAIR, 2d FLAIR, and 2d T2-Weighted MR Imaging of Brain Stem Anatomy. *American Journal of Neuroradiology*, 33(5):922–927, May 2012. doi: 10.3174/ajnr.A2874.

Michael J. Knight, Bryony McCann, Demitra Tsivos, Elizabeth Couthard, and Risto A. Kauppinen. Quantitative T1 and T2 MRI signal characteristics in the human brain: different patterns of MR contrasts in normal ageing. *Magnetic Resonance Materials in Physics, Biology and Medicine*, 29(6):833–842, December 2016. doi: 10.1007/s10334-016-0573-0.

Rajesh Kumar, Sean Delshad, Paul M. Macey, Mary A. Woo, and Ronald M. Harper. Development of T2-relaxation Values in Regional Brain Sites during Adolescence. *Magnetic resonance imaging*, 29(2):185–193, February 2011. doi: 10.1016/j.mri.2010.08. 006. 00013.

Timo Kurki and Markku Komu. Spin-lattice relaxation and magnetization transfer in intracranial tumors in vivo: Effects of Gd-DTPA on relaxation parameters. *Magnetic Resonance Imaging*, 13(3):379–385, January 1995. doi: 10.1016/0730-725X(94) 00126-N.

Christian Langkammer, Nikolaus Krebs, Walter Goessler, Eva Scheurer, Franz Ebner, Kathrin Yen, Franz Fazekas, and Stefan Ropele. Quantitative MR Imaging of Brain

Iron: A Postmortem Validation Study. *Radiology*, 257(2):455–462, November 2010. doi: 10.1148/radiol.10100495. 00088.

H. B. W. Larsson, J. Frederiksen, J. Petersen, A. Nordenbo, I. Zeeberg, O. Henriksen, and J. Olesen. Assessment of demyelination, edema, and gliosis by in vivo determination of T1 and T2 in the brain of patients with acute attack of multiple sclerosis. *Magnetic Resonance in Medicine*, 11(3):337–348, September 1989. doi: 10.1002/mrm.1910110308.

R Marc Lebel. StimFit: A toolbox for robust T2 mapping with stimulated echo compensation. In *Proceedings of the Meeting of the International Society for Magnetic Resonance in Medicine*, page 2558, Melbourne, Australia, 2012. URL `http://www.ismrm.org/12/tp_12.htm`.

R. Marc Lebel and Alan H. Wilman. Transverse relaxometry with stimulated echo compensation. *Magnetic Resonance in Medicine*, 64(4):1005–1014, 2010. doi: 10.1002/mrm.22487.

R. Marc Lebel, Amir Eissa, Peter Seres, Gregg Blevins, and Alan H. Wilman. Quantitative high-field imaging of sub-cortical gray matter in multiple sclerosis. *Multiple Sclerosis Journal*, 18(4):433–441, April 2012. doi: 10.1177/1352458511428464.

Ilana R. Leppert, C. Robert Almli, Robert C. McKinstry, Robert V. Mulkern, Carlo Pierpaoli, Michael J. Rivkin, and G.Bruce Pike. T2 Relaxometry of Normal Pediatric Brain Development. *Journal of magnetic resonance imaging : JMRI*, 29(2):258–267, February 2009. doi: 10.1002/jmri.21646.

Stephanie Lescher, Alina Jurcoane, Andreas Veit, Oliver B ahr, Ralf Deichmann, and Elke Hattingen. Quantitative T1 and T2 mapping in recurrent glioblastomas under bevacizumab: earlier detection of tumor progression compared to conventional MRI. *Neuroradiology*, 57(1):11–20, January 2015. doi: 10.1007/s00234-014-1445-9.

Ke Li, Richard D. Dortch, E. Brian Welch, Nathan D. Bryant, Amanda K.W. Buck, Theodore F. Towse, Daniel F. Gochberg, Mark D. Does, Bruce M. Damon, and Jane H. Park. Multi-parametric MRI characterization of healthy human thigh muscles at 3.0T

- relaxation, magnetization transfer, fatwater, and diffusion tensor imaging. *NMR in biomedicine*, 27(9):1070–1084, September 2014. doi: 10.1002/nbm.3159.

Serguei Liachenko and Jaivijay Ramu. Quantification and reproducibility assessment of the regional brain T2 relaxation in nave rats at 7t. *Journal of Magnetic Resonance Imaging*, 45(3):700–709, March 2017. doi: 10.1002/jmri.25378.

Gary P. Liney, Adrian J. Knowles, David J. Manton, Lindsay W. Turnbull, Stephen J. Blackband, and Anthony Horsman. Comparison of conventional single echo and multi-echo sequences with a fast spin-echo sequence for quantitative T2 mapping: Application to the prostate. *Journal of Magnetic Resonance Imaging*, 6(4):603–607, 1996. doi: 10.1002/jmri.1880060408.

Haiying Liu, Edward Michel, Sean O. Casey, and Charles L. Truwit. Actual imaging slice profile of 2d MRI. In L.E. Antonuk and M.J. Yaffe, editors, *Medical Imaging 2002: Physics of Medical Imaging*, volume 4682 of *Proceedings of the SPIE*, pages 767–773, May 2002.

Tarja L onnfors-Weitzel, Thilo Weitzel, Johannes Slotboom, Claus Kiefer, Claudio Pollo, Michael Sch upbach, Markus Oertel, Alain Kaelin, and Roland Wiest. T2-relaxometry predicts outcome of DBS in idiopathic Parkinson's disease. *NeuroImage : Clinical*, 12: 832–837, September 2016. doi: 10.1016/j.nicl.2016.09.019. 00000.

Dan Ma, Vikas Gulani, Nicole Seiberlich, Kecheng Liu, Jeffrey L. Sunshine, Jeffrey L. Duerk, and Mark A. Griswold. Magnetic resonance fingerprinting. *Nature*, 495(7440): 187–192, March 2013. doi: 10.1038/nature11971.

Marnix C. Maas, Eline K. Vos, Miriam W. Lagemaat, Andreas K. Bitz, Stephan Orzada, Thiele Kobus, Oliver Kraff, Stefan Maderwald, Mark E. Ladd, and Tom W. J. Scheenen. Feasibility of T2-weighted turbo spin echo imaging of the human prostate at 7 tesla. *Magnetic Resonance in Medicine*, 71(5):1711–1719, May 2014. doi: 10.1002/mrm.24818.

A. MacKay, C. Laule, I. Vavasour, B. M adler, A. Traboulsee, D. Paty, W. Moore, and D. Li. The Short T2 Component in Normal-Appearing White Matter in Multiple Sclerosis. In *Normal-appearing White and Grey Matter Damage in Multiple Sclerosis*, Topics in Neuroscience, pages 47–61. Springer, Milano, 2004. DOI: 10.1007/978-88-470-2127-3_5.

A.L. MacKay, I.M. Vavasour, A. Rauscher, S.H. Kolind, B. M adler, G.R.W. Moore, A.L. Traboulsee, D.K.B. Li, and C. Laule. MR Relaxation in Multiple Sclerosis. *Neuroimaging Clinics of North America*, 19(1):1–26, February 2009. doi: 10.1016/j.nic.2008.09.007.

Alex MacKay, Cornelia Laule, Irene Vavasour, Thorarin Bjarnason, Shannon Kolind, and Burkhard M adler. Insights into brain microstructure from the T2 distribution. *Magnetic Resonance Imaging*, 24(4):515–525, May 2006. doi: 10.1016/j.mri.2005.12.037.

S. Majumdar, S. C. Orphanoudakis, A. Gmitro, M. O'Donnell, and J. C. Gore. Errors in the measurements of T2 using multiple-echo MRI techniques. I. Effects of radiofrequency pulse imperfections. *Magnetic Resonance in Medicine*, 3(3):397–417, 1986a. doi: 10.1002/mrm.1910030305.

S. Majumdar, S. C. Orphanoudakis, A. Gmitro, M. O'Donnell, and J. C. Gore. Errors in the measurements of T2 using multiple-echo MRI techniques. II. Effects of static field inhomogeneity. *Magnetic Resonance in Medicine: Official Journal of the Society of Magnetic Resonance in Medicine / Society of Magnetic Resonance in Medicine*, 3 (4):562–574, August 1986b.

Francesco Manfredonia, Olga Ciccarelli, Zhaleh Khaleeli, Daniel J. Tozer, Jaume Sastre-Garriga, David H. Miller, and Alan J. Thompson. Normal-appearing brain t1 relaxation time predicts disability in early primary progressive multiple sclerosis. *Archives of Neurology*, 64(3):411–415, March 2007. doi: 10.1001/archneur.64.3.411.

Stephen J Matzat, Jasper van Tiel, Garry E Gold, and Edwin H G Oei. Quantitative MRI

techniques of cartilage composition. *Quantitative imaging in medicine and surgery*, 3
(3):162–174, June 2013. doi: 10.3978/j.issn.2223-4292.2013.06.04.

Stephen J. Matzat, Emily J. McWalter, Feliks Kogan, Weitian Chen, and Garry E. Gold.
T2 Relaxation time quantitation differs between pulse sequences in articular cartilage.
Journal of Magnetic Resonance Imaging, pages n/a–n/a, 2014. doi: 10.1002/jmri.
24757.

Kelly C. McPhee and Alan H. Wilman. T2 quantification from only proton density and
T2-weighted MRI by modelling actual refocusing angles. *NeuroImage*, 118:642–650,
September 2015. doi: 10.1016/j.neuroimage.2015.05.079.

Kelly C. McPhee and Alan H. Wilman. Transverse relaxation and flip angle mapping:
Evaluation of simultaneous and independent methods using multiple spin echoes. *Magnetic Resonance in Medicine*, 77(5):2057–2065, May 2017. doi: 10.1002/mrm.26285.

Donald W. McRobbie, Elizabeth A. Moore, Martin J. Graves, and Martin R. Prince.
MRI from Picture to Proton. Cambridge University Press, September 2006. 00412.

S. Meiboom and D. Gill. Modified Spin-Echo Method for Measuring Nuclear Relaxation
Times. *Review of Scientific Instruments*, 29:688–691, August 1958. doi: 10.1063/1.
1716296.

Amanda F. Mejia, Elizabeth M. Sweeney, Blake Dewey, Govind Nair, Pascal Sati, Colin
Shea, Daniel S. Reich, and Russell T. Shinohara. Statistical estimation of T1 relaxation
times using conventional magnetic resonance imaging. *NeuroImage*, 133:176–188, June
2016. doi: 10.1016/j.neuroimage.2015.12.037.

Fumiyuki Mitsumori, Hidehiro Watanabe, and Nobuhiro Takaya. Estimation of brain iron
concentration in vivo using a linear relationship between regional iron and apparent
transverse relaxation rate of the tissue water at 4.7t. *Magnetic Resonance in Medicine*,
62(5):1326–1330, 2009. doi: 10.1002/mrm.22097.

Fumiyuki Mitsumori, Hidehiro Watanabe, Nobuhiro Takaya, Michael Garwood, Edward J. Auerbach, Shalom Michaeli, and Silvia Mangia. Toward understanding trans-

verse relaxation in human brain through its field dependence. *Magnetic Resonance in Medicine*, 68(3):947–953, 2012. doi: 10.1002/mrm.23301.

Timothy J. Mosher, Yi Liu, and Collin M. Torok. Functional Cartilage MRI T2 Mapping: Evaluating the Effect of Age and Training on Knee Cartilage Response to Running. *Osteoarthritis and cartilage / OARS, Osteoarthritis Research Society*, 18(3):358–364, March 2010. doi: 10.1016/j.joca.2009.11.011. 00060.

John P. Mugler. Optimized three-dimensional fast-spin-echo MRI. *Journal of Magnetic Resonance Imaging*, 39(4):745–767, April 2014. doi: 10.1002/jmri.24542. 00073.

Takashi Nishii, Toshiyuki Shiomi, Hisashi Tanaka, Youichi Yamazaki, Kenya Murase, and Nobuhiko Sugano. Loaded Cartilage T2 Mapping in Patients with Hip Dysplasia. *Radiology*, 256(3):955–965, September 2010. doi: 10.1148/radiol.10091928.

Dwight G. Nishimura. *Principles of Magnetic Resonance Imaging.* Stanford Univ, 1.1 edition, February 2010.

European Society of Radiology. Magnetic Resonance Fingerprinting - a promising new approach to obtain standardized imaging biomarkers from MRI. *Insights into Imaging*, 6(2):163–165, April 2015. doi: 10.1007/s13244-015-0403-3.

G. J. Parker, G. J. Barker, and P. S. Tofts. Accurate multislice gradient echo T(1) measurement in the presence of non-ideal RF pulse shape and RF field nonuniformity. *Magnetic Resonance in Medicine: Official Journal of the Society of Magnetic Resonance in Medicine / Society of Magnetic Resonance in Medicine*, 45(5):838–845, May 2001.

J. Pauly, P. Le Roux, Dwight Nishimura, and A. Macovski. Parameter relations for the Shinnar-Le Roux selective excitation pulse design algorithm [NMR imaging]. *IEEE Transactions on Medical Imaging*, 10(1):53–65, 1991. doi: 10.1109/42.75611.

Gaby S. Pell, Regula S. Briellmann, Anthony B. Waites, David F. Abbott, David P. Lewis, and Graeme D. Jackson. Optimized clinical T2 relaxometry with a standard

CPMG sequence. *Journal of Magnetic Resonance Imaging*, 23(2):248–252, 2006. doi: 10.1002/jmri.20490. 00058.

Thomas Prasloski, Burkhard M adler, Qing-San Xiang, Alex MacKay, and Craig Jones. Applications of stimulated echo correction to multicomponent T2 analysis. *Magnetic Resonance in Medicine*, 67(6):1803–1814, 2012. doi: 10.1002/mrm.23157.

Joseph R. Roebuck, Steven J. Haker, Dimitris Mitsouras, Frank J. Rybicki, Clare M. Tempany, and Robert V. Mulkern. Carr-Purcell-Meiboom-Gill imaging of prostate cancer: quantitative T2 values for cancer discrimination. *Magnetic Resonance Imaging*, 27(4):497–502, May 2009. doi: 10.1016/j.mri.2008.08.001.

W. D. Rooney, J. R. Poolaro, S. C. Forbes, D. J. Wang, K Vanderborne, and G. A. Walter. Application of the Extended Phase Graph Technique to Improve T2 Quantitation Across Sites. In *Proceedings of International Society for Magnetic Resonance in Medicine Annual Meeting 19*, volume 19, page 138, 2011.

P. Roschmann. Radiofrequency penetration and absorption in the human body: Limitations to high-field whole-body nuclear magnetic resonance imaging. *Medical Physics*, 14(6):922–931, 1987. doi: 10.1118/1.595995.

John F. Schenck and Earl A. Zimmerman. High-field magnetic resonance imaging of brain iron: birth of a biomarker? *NMR in Biomedicine*, 17(7):433–445, 2004. doi: 10.1002/nbm.922.

J. Sedlacik, K. Boelmans, U. L obel, B. Holst, S. Siemonsen, and J. Fiehler. Reversible, irreversible and effective transverse relaxation rates in normal aging brain at 3 T. *NeuroImage*, 84:1032–1041, January 2014. doi: 10.1016/j.neuroimage.2013.08.051.

S. T. Soellner, A. Goldmann, D. Muelheims, G. H. Welsch, and M. L. Pachowsky. Intraoperative validation of quantitative T2 mapping in patients with articular cartilage lesions of the knee. *Osteoarthritis and Cartilage*, 25(11):1841–1849, November 2017. doi: 10.1016/j.joca.2017.07.021.

R. J. Stafford. High Field Mri - Technology, Applications, Safety, and Limitations. *Medical Physics*, 31(6), June 2004.

Greg J. Stanisz, Ewa E. Odrobina, Joseph Pun, Michael Escaravage, Simon J. Graham, Michael J. Bronskill, and R. Mark Henkelman. T1, T2 relaxation and magnetization transfer in tissue at 3t. *Magnetic Resonance in Medicine*, 54(3):507–512, 2005. doi: 10.1002/mrm.20605. 00545.

Rudolf Stollberger and Paul Wach. Imaging of the active B1 field in vivo. *Magnetic Resonance in Medicine*, 35(2):246–251, 1996. doi: 10.1002/mrm.1910350217.

Tilman J. Sumpf, Martin Uecker, Susann Boretius, and Jens Frahm. Model-based nonlinear inverse reconstruction for T2 mapping using highly undersampled spin-echo MRI. *Journal of Magnetic Resonance Imaging*, 34(2):420–428, August 2011. doi: 10.1002/jmri.22634. 00057.

Enver Tahir, Martin Sinn, Sebastian Bohnen, Maxim Avanesov, Dennis S aring, Christian Stehning, Bernhard Schnackenburg, Christine Eulenburg, Joshua Wien, Ulf K. Radunski, Stefan Blankenberg, Gerhard Adam, Charles B. Higgins, Maythem Saeed, Kai Muellerleile, and Gunnar K. Lund. Acute versus Chronic Myocardial Infarction: Diagnostic Accuracy of Quantitative Native T1 and T2 Mapping versus Assessment of Edema on Standard T2-weighted Cardiovascular MR Images for Differentiation. *Radiology*, 285(1):83–91, October 2017. doi: 10.1148/radiol.2017162338.

Shoichiro Takao, Tan B. Nguyen, Hon J. Yu, Shigeo Hagiwara, Yasuhito Kaneko, Taiki Nozaki, Seiji Iwamoto, Maki Otomo, Ran Schwarzkopf, and Hiroshi Yoshioka. T1rho and T2 relaxation times of the normal adult knee meniscus at 3t: analysis of zonal differences. *BMC Musculoskeletal Disorders*, 18, May 2017. doi: 10.1186/s12891-017-1560-y.

N Takaya, H Watanabe, and F Mitsumori. Elongated T1 values in human brain and the optimization of MDEFT measurements at 4.7t. In *Proceedings of the 12th Annual Meeting of ISMRM*, volume 12, page 2339, Kyoto, Japan, 2004.

Jody L. Tanabe, Martina Vermathen, Robert Miller, Deborah Gelinas, Michael W. Weiner, and William D. Rooney. Reduced MTR in the corticospinal tract and normal T2 IN amyotrophic lateral sclerosis. *Magnetic resonance imaging*, 16(10):1163–1169, December 1998.

Haiying Tang, Jens H. Jensen, Christina L. Sammet, Sujit Sheth, Srirama V. Swaminathan, Kristi Hultman, Daniel Kim, Ed X. Wu, Truman R. Brown, and Gary M. Brittenham. MR characterization of hepatic storage iron in transfusional iron overload. *Journal of Magnetic Resonance Imaging*, 39(2):307–316, February 2014. doi: 10.1002/jmri.24171.

David L. Thomas, Enrico De Vita, Ralf Deichmann, Robert Turner, and Roger J. Ordidge. 3d MDEFT imaging of the human brain at 4.7 T with reduced sensitivity to radiofrequency inhomogeneity. *Magnetic resonance in medicine : official journal of the Society of Magnetic Resonance in Medicine / Society of Magnetic Resonance in Medicine*, 53(6):1452–1458, June 2005. doi: 10.1002/mrm.20482.

Paul Tofts. *Quantitative MRI of the Brain: Measuring Changes Caused by Disease*. Wiley, 1 edition, October 2003.

Md. Nasir Uddin, R. Marc Lebel, and Alan H. Wilman. Transverse relaxometry with reduced echo train lengths via stimulated echo compensation. *Magnetic Resonance in Medicine*, 70(5):1340–1346, 2013. doi: 10.1002/mrm.24568.

Md Nasir Uddin, R. Marc Lebel, Peter Seres, Gregg Blevins, and Alan H. Wilman. Spin echo transverse relaxation and atrophy in multiple sclerosis deep gray matter: A two-year longitudinal study. *Multiple Sclerosis (Houndmills, Basingstoke, England)*, 22(9): 1133–1143, August 2016. doi: 10.1177/1352458515614091.

Md. Nasir Uddin, Kelly C. McPhee, Gregg Blevins, and Alan H. Wilman. Recovery of accurate T2 from historical 1.5 tesla proton density and T2-weighted images: Application to 7-year T2 changes in multiple sclerosis brain. *Magnetic Resonance Imaging*, 37:21–26, April 2017. doi: 10.1016/j.mri.2016.11.007.

J.T. Vaughan, M. Garwood, C.m. Collins, W. Liu, L. DelaBarre, G. Adriany, P. Andersen, H. Merkle, R. Goebel, M.b. Smith, and K. Ugurbil. 7t vs. 4t: RF power, homogeneity, and signal-to-noise comparison in head images. *Magnetic Resonance in Medicine*, 46 (1):24–30, July 2001. doi: 10.1002/mrm.1156.

Irene M. Vavasour, Kenneth P. Whittall, David K.B. Li, and Alex L. MacKay. Different magnetization transfer effects exhibited by the short and long T2 components in human brain. *Magnetic Resonance in Medicine*, 44(6):860–866, 2000. doi: 10.1002/1522-2594(200012)44:6⟨860::AID-MRM6⟩3.0.CO;2-C.

David Verhaert, Paaladinesh Thavendiranathan, Shivraman Giri, Georgeta Mihai, Sanjay Rajagopalan, Orlando P. Simonetti, and Subha V. Raman. Direct T2 Quantification of Myocardial Edema in Acute Ischemic Injury. *JACC: Cardiovascular Imaging*, 4(3): 269–278, March 2011. doi: 10.1016/j.jcmg.2010.09.023.

Marinus T. Vlaardingerbroek and Jacques A. den Boer. *Magnetic Resonance Imaging*. Springer, 2 edition, January 1999. Google-Books-ID: n3e0QgAACAAJ.

Josef Vymazal, Rodney A. Brooks, Charles Baumgarner, Vu Tran, David Katz, Jeff W. M. Bulte, E. Rivka Bauminger, and Giovanni Di Chiro. The relation between brain iron and NMR relaxation times: An in vitro study. *Magnetic Resonance in Medicine*, 35(1):56–61, 1996. doi: 10.1002/mrm.1910350108.

D. Wagnerová, V. Herynek, M. Dezortová, P. Marusič, P. Krek, J. Zámečník, F. Jírøu, A. Škoch, and M. Hájek. The relationships between quantitative MR parameters in hippocampus in healthy subjects and patients with temporal lobe epilepsy. *Physiological Research*, 64(3):407–417, 2015.

Andrew J. Walsh, R. Marc Lebel, Amir Eissa, Gregg Blevins, Ingrid Catz, Jian-Qiang Lu, Lothar Resch, Edward S. Johnson, Derek J. Emery, Kenneth G. Warren, and Alan H. Wilman. Multiple Sclerosis: Validation of MR Imaging for Quantification and Detection of Iron. *Radiology*, 267(2):531–542, May 2013. doi: 10.1148/radiol.12120863.

J.b.m. Warntjes, O. Dahlqvist, and P. Lundberg. Novel method for rapid, simultaneous T1, T*2, and proton density quantification. *Magnetic Resonance in Medicine*, 57(3): 528–537, March 2007. doi: 10.1002/mrm.21165.

J.B.M. Warntjes, O. Dahlqvist Leinhard, J. West, and P. Lundberg. Rapid magnetic resonance quantification on the brain: Optimization for clinical usage. *Magnetic Resonance in Medicine*, 60(2):320–329, August 2008. doi: 10.1002/mrm.21635.

Matthias Weigel. Extended phase graphs: Dephasing, RF pulses, and echoes - pure and simple. *Journal of Magnetic Resonance Imaging*, 41(2):266–295, February 2015. doi: 10.1002/jmri.24619.

Nikolaus Weiskopf, John Suckling, Guy Williams, Marta M. Correia, Becky Inkster, Roger Tait, Cinly Ooi, Edward T. Bullmore, and Antoine Lutti. Quantitative multi-parameter mapping of R1, PD*, MT, and R2* at 3t: a multi-center validation. *Frontiers in Neuroscience*, 7, June 2013. doi: 10.3389/fnins.2013.00095.

White Matter Study Group. White Matter Study Group Meeting. In *Proceedings of ISMRM*, volume 25, April 2017. URL `https://www.ismrm.org/17/SG13_White_Matter_Program.pdf`.

Kenneth P Whittall, Alex L. Mackay, Douglas A. Graeb, Robert A. Nugent, David K. B. Li, and Donald W. Paty. In vivo measurement of T2 distributions and water contents in normal human brain. *Magnetic Resonance in Medicine*, 37(1):34–43, 1997. doi: 10.1002/mrm.1910370107.

Rebecca J. Willcocks, William D. Rooney, William T. Triplett, Sean C. Forbes, Donovan J. Lott, Claudia R. Senesac, Michael J. Daniels, Dah-Jyuu Wang, Ann T. Harrington, Gihan I. Tennekoon, Barry S. Russman, Erika L. Finanger, Barry J. Byrne, Richard S. Finkel, Glenn A. Walter, H. Lee Sweeney, and Krista Vandenborne. Multicenter prospective longitudinal study of magnetic resonance biomarkers in a large duchenne muscular dystrophy cohort. *Annals of Neurology*, 79(4):535–547, April 2016. doi: 10.1002/ana.24599.

L Yao, A Gentili, and A Thomas. Incidental magnetization transfer contrast in fast spin-echo imaging of cartilage. *Journal of magnetic resonance imaging: JMRI*, 6(1): 180–184, February 1996.

Appendix A

Supplementary Figures

This Appendix contains images which were prepared as supplementary figures, or are displaying results which were discussed but not shown in the respective chapters.
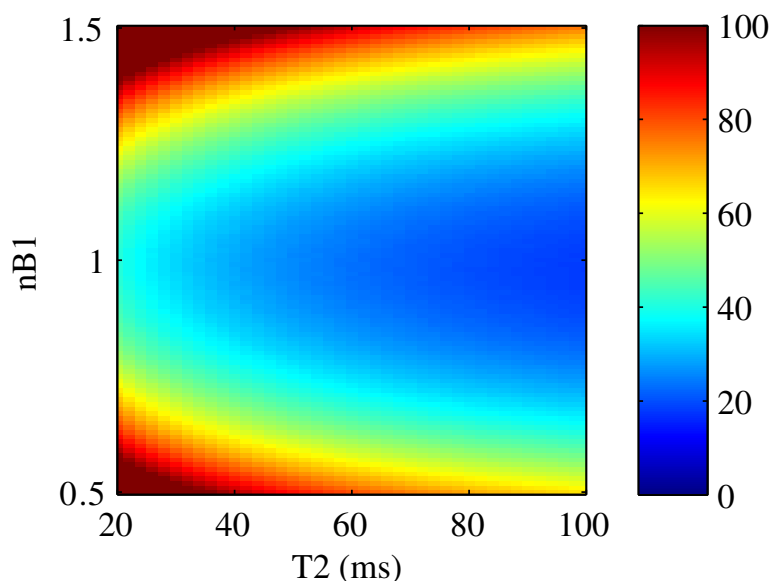
A.1   Supplementary Figures for Chapter 2

Figure A.1: Mean error in T2 fit result (%) from simulated MESE T2 decay curves with T1 = 1 s, 500 repetitions at SNR = 50 when using a simple mono-exponential model. Errors observed are 20% to >100%.
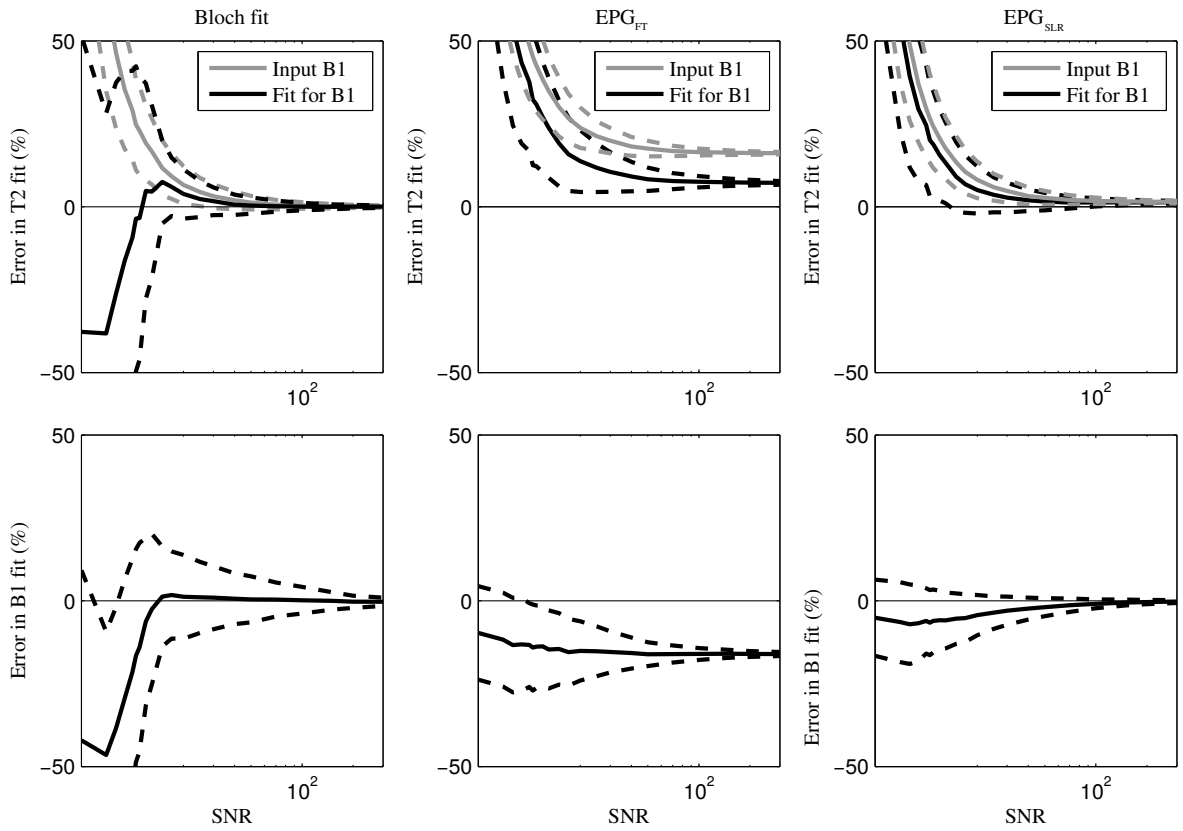
Figure A.2: Mean error in T2 fit values (solid lines) ± coefficient of variation of (dashed line) for simulated T2 = 50 ms and nB1 = 1.0 for a range of SNR are shown (a-c) for each algorithm, and corresponding B1 fits are shown below (d-f).
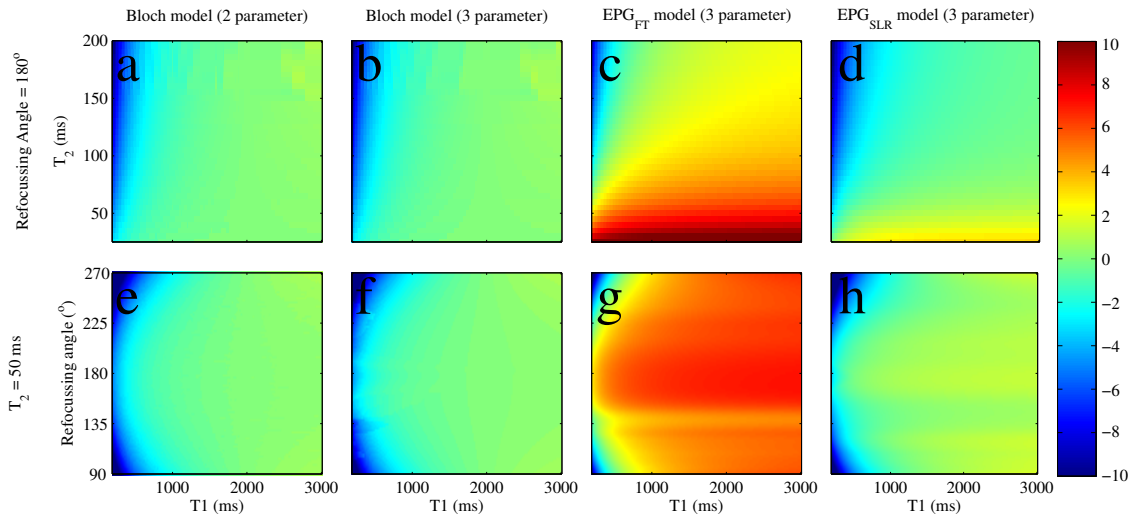
Figure A.3: T2 mapping using the Bloch model for ISEC was found to be robust to errors in the assumed T1, where T1 is estimated within 1 second. The EPG$_{SLR}$ fitting model was similarly robust, however, the EPG$_{FT}$ model, overestimated T2. Fit accuracy in all models is relatively insensitive to T1, when fitting uses a T1 estimate (here, 2 s) within 1 s of the actual T1 (1-3 s).
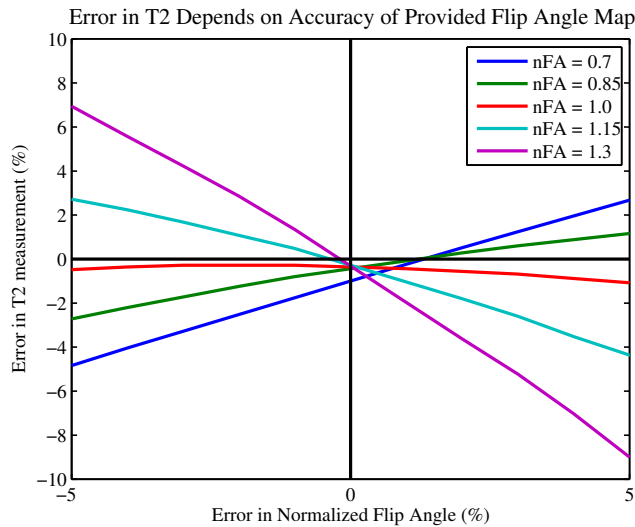

Figure A.4: T2 accuracy is examined when erroneous nB1 values are provided to Bloch-ISEC fitting. T2 measurements are found to be robust to small errors in the nB1 map. Simulations were performed for a T2 of 50 ms, T1 of 1 s, and a range of nB1 values.

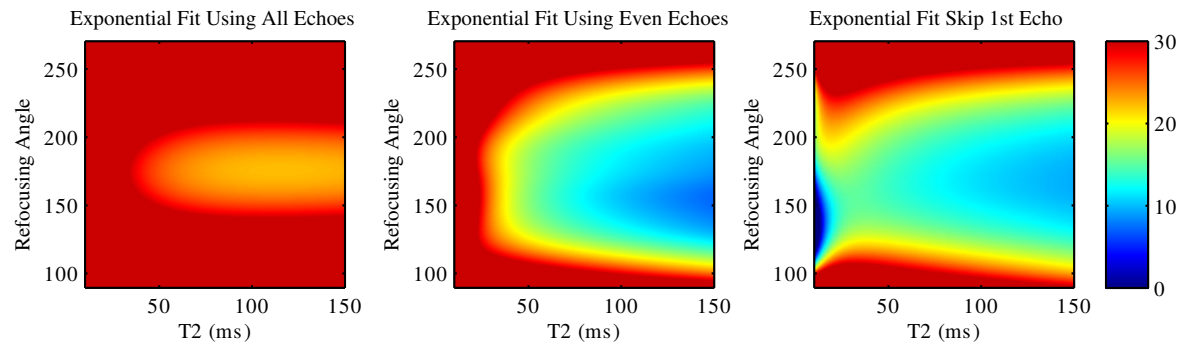## A.2 Supplementary Figures for Chapter 3

Figure A.5: Error in exponential T2 fitting of 12 echoes, simulating 1.5T experiments. Results show similar trends to simulations of 4.7T experiments. Differences are primarily due to use of different pulse shapes. 1.5T experiments were performed on a clinical scanner, using proprietary Siemens standard optimized pulse shapes.